

# **Investigation of the influence of mechanical pressure on the aging and the expansion of silicon-containing lithium-ion batteries**

Von der Fakultät für Ingenieurwissenschaften  
der Universität Bayreuth  
zur Erlangung der Würde einer  
Doktor-Ingenieurin (Dr.-Ing.)  
genehmigte Dissertation

von  
Verena Müller, M. Sc.  
aus  
Neustadt a. d. Aisch

Erstgutachter: Prof. Dr.-Ing. Michael Danzer

Zweitgutachterin: Prof. Dr.-Ing. Christina Roth

Tag der mündlichen Prüfung: 05.08.2020

Lehrstuhl Elektrische Energiesysteme  
Universität Bayreuth

2020



## Kurzzusammenfassung

Um die steigende Nachfrage nach Batterie-Elektrischen-Fahrzeugen (BEVs) bedienen zu können, müssen heutige Lithium-Ionen-Batterie-Zellen (LiBs) hohe Anforderungen hinsichtlich ihrer volumetrischen Energiedichte, der Lebensdauer sowie der Leistungsfähigkeit erfüllen. Aufgrund ihrer hohen spezifischen Kapazität spielen Silicium-(Si)-haltige Anodenmaterialien zur Erreichung dieser Ziele eine enorme Rolle. Allerdings weist Si eine Volumenausdehnung von bis zu 300% während der Lithiierung auf, was die Forschung und Entwicklung vor einige Schwierigkeiten stellt. Abgesehen von den technischen Herausforderungen bei der Applikation in Batterie-Modulen oder -Packs, führt die starke Ausdehnung zu starken Alterungseffekten in den Elektroden. Partikelbrüche, Kontaktverluste und die Ablösung von Aktivmaterial von der Kollektorfolie können die Folge sein. Neben einigen Ansätzen, diesen Problemen auf Material-Ebene durch die Optimierung des verwendeten Binders, des Aktivmaterials oder des Elektrolyten entgegenzuwirken, sind weitere Maßnahmen auf Zell-Ebene erforderlich. Eine vielversprechende Aussicht bietet dabei die Applikation mechanischen Drucks auf die Si-haltigen Zellen, um die Entstehung von Kontaktverlusten und Delaminationen in der Zelle zu verhindern.

Daher beschäftigt sich diese Arbeit mit der Untersuchung des Einflusses mechanischer Verspannung auf die Alterung verschiedener Si-haltiger Anodenmaterialien kombiniert mit Nickel-reichen Kathoden. Zunächst wird der Effekt mechanischen Drucks auf die elektrochemischen Prozesse in Elektroden anhand von Elektrochemischer Impedanzspektroskopie (EIS) in symmetrischen Zellen erarbeitet. Dabei wird eine Abnahme der Lithium-Ionen Leitfähigkeit in den Poren der verspannten Elektroden deutlich. Kombiniert mit durchgeführten Kompressionsmessungen helfen die Ergebnisse dabei die verringerte Zellkapazität von verspannten LiBs bei erhöhter Stromdichte zu erklären. Vor allem für Elektroden mit hoher Flächenmasse resultiert die reduzierte Lithium-Ionen Leitfähigkeit in den Poren bei einer erhöhten Stromdichte in einer starken Erhöhung der Impedanz. Andererseits kann die Kapazität der Zellen bei kleinen Stromdichten aufgrund des verbesserten elektrischen Kontakts vergrößert werden. Diese Ergebnisse zeigen die Wichtigkeit der genauen Definition der Betriebsbedingungen mit dem zu applizierenden Druck.

Im nächsten Schritt wird das erlangte Wissen auf die Optimierung von Si-haltigen LiBs angewendet. Dazu werden zwei verschiedene Si-basierte Komposit-Materialien untersucht. Das erste Material weist einen geringen Si-anteil von  $\sim 8$  wt% auf, dessen Kapazität vollständig genutzt wird und es somit im Laufe der Zyklierung zu einer starken Volumenausdehnung kommt. Zusätzlich wird ein Komposit mit einem hohen Si-Anteil von  $\sim 50$  wt% und definierter Partikelporosität evaluiert, welche die Volumenausdehnung des Si abdämpfen soll. Beide Anodenmaterialien werden zunächst in Pouch-Zellen mit Ni-reichen Kathoden in flexibler und fixierter Druckkonfiguration bei Drücken von 0.08 MPa, 0.42 MPa und 0.84 MPa getestet. Erstere ermöglicht die Ausdehnung der Zellen, wobei der Druck konstant gehalten wird. Die fixierte Verspannung verhindert die Ausdehnung der Zelle, was zur Erhöhung des Drucks führt. Die Expansion sowie die orts aufgelöste Druckverteilung auf der

Zelloberfläche können operando während des Betriebs der Zellen gemessen werden. Die Ergebnisse zeigen die hohe Wichtigkeit der Applikation eines mechanischen Drucks auf die Si-haltigen LiBs. Durch die verhinderten Kontaktverluste und die Verringerung von Partikelbrüchen wird die Lebensdauer drastisch verlängert. Weiterhin können, durch ausführliche Analysen, zwei unterschiedliche Alterungsmechanismen in Abhängigkeit der jeweiligen Druckkonfiguration der Si-haltigen LiBs mit starker Ausdehnung erarbeitet werden. Werden die LiBs unter flexibler Verspannung zyklisiert, führt die sich wiederholende Volumenausdehnung zu einer stark erhöhten Anodenpassivierung. Dies hat Verluste von zyklisierbarem Lithium und damit eine lineare Alterung zur Folge. Dahingegen führt die fixierte Verspannung der LiBs zur Ausbildung starker Druckinhomogenitäten mit Hot-Spots in Bereichen erhöhter Strombelastung. Dies führt zu einem Verschluss von Poren des Separators, was die verfügbare Kapazität durch erhöhte Überspannung stark reduziert.

Die Si-haltige Anode mit eingebetteter Porosität zeigt eine stark verringerte Expansion. Durch weitere Optimierungen der Elektrodendichte und des applizierten Drucks kann die Lebensdauer dieser Zellen verbessert werden. Die erhöhte Porosität des Materials führt allerdings auch zu einer reduzierten volumetrischen Energiedichte.

Schlussendlich können die anhand von Pouch-Zellen erzielten Ergebnisse noch auf großformatige, prismatische Zellen transferiert werden. Mit Hilfe von operando Expansionsmessungen und Computertomographie können mechanische Deformationen der Elektrodenwicklungen in den prismatischen Zellen über ihre Lebensdauer untersucht werden. Analog zu den Pouch-Zellen kann die Zyklenstabilität der prismatischen Zellen durch mechanische Verspannung stark verbessert werden.

Durch die Untersuchung der druckabhängigen Alterung sowie Ausdehnung neuartiger Aktivmaterialien in verschiedener Skalierung von Elektrode über Pouch-Zelle bis hin zu prismatischen Zellen, schafft diese Arbeit eine wichtige Grundlage für die optimierte Auslegung und den Betrieb dieser Materialien in zukünftigen Applikationen. Das erarbeitete Wissen kann dafür genutzt werden, die Entwicklung neuer Modul- und Pack-Konzepte zu erleichtern und treibt die großflächige Nutzung von Si als Aktivmaterial in LiB Applikationen voran.

## Abstract

The demand for Battery Electric Vehicles (BEVs) is constantly increasing resulting in the need for optimization of today's Lithium-ion battery cells (LiBs) in terms of volumetric energy density, lifetime, and high power ability. Due to their high specific capacity, next generation anode active materials as silicon (Si) play an important role to achieve these future goals. However, the high volume expansion of the Si of up to 300% during the lithiation leads to numerous drawbacks on system and cell level. Apart from numerous technical challenges for the application of those LiBs in module or pack constraints, the repetitive volume changes lead to particle cracking, contact loss, and delamination from the current collector foil. Besides several approaches on material level, i.e. new binders, modification of the active material, and the utilization of tailored electrolytes, developments on cell level are necessary to enable the extensive application of Si in automotive applications. One promising idea is the application of a mechanical pressure on the Si-containing cells to prevent contact loss, particle fractures, and layer detachment.

In this work the influence of such a mechanical compression on different Si-containing anode materials is investigated in full cells with a Ni-rich layered oxide cathode material. Initially, the effects of the applied pressure on the microstructure of the electrodes are investigated via Electrochemical Impedance Spectroscopy (EIS) measurements of symmetrical cells. The results show a reduction of the Li-ion mobility within the pores of compressed electrodes. The data gained from a combination of EIS with compressibility measurements of the examined electrodes allows the interpretation of the current rate stability of the LiBs depending on the applied pressure. For electrodes with a high mass loading, the reduced pore volume in the compressed electrodes results in a hindered ion mobility. This is pronounced at high current densities reducing the available capacity by an increased polarization. Contrariwise, at low current densities the improved electric contact in the cells is beneficial for their lifetime and their performance compared to uncompressed cells.

In the next step, the gained knowledge about the pressure-dependent sensitivity of the electrochemical processes in the electrodes is applied on Si-containing LiBs. Two different material concepts are presented. Firstly, the influence of the mechanical pressure on a C/Si-composite with  $\sim 8$  wt% Si is investigated. The capacity of this composite is fully utilized resulting in a high vertical expansion. Secondly, a Si-rich composite with  $\sim 50$  wt% Si is examined, which was designed with embedded porosity in an encapsulated C-matrix preventing the vertical expansion. To enable the comparison with state-of-the-art applications, the cells are tested at different flexible and fixed pressure configurations at certain pressure levels of 0.08 MPa, 0.42 MPa, and 0.84 MPa. The flexible configuration enables the expansion of the cells under a constant pressure, while the fixed configuration inhibits the expansion leading to the increase of the pressure in the fixture. Operando expansion measurements with a high accuracy are conducted within the flexible configuration. Furthermore, a new pressure mapping system introduced herein enables the spatially resolved evaluation of the pressure distribution on the surface of the pouch cells. The results demonstrate that the application of a mechanical pressure is of an utmost importance to prevent accelerated degra-

dation in the Si-containing anodes and to prolong the cycle life. Furthermore, different pressure induced aging mechanisms can be identified in the case of the C/Si-composite with a high vertical expansion. When cycled in a heavily flexible pressure configuration, the C/Si-anode tends to an accelerated film formation due to the repetitive swelling. Therefore, the cycleable Li is reduced causing a linear degradation of the cells. Contrariwise, the attempt of preventing the swelling in the heavily fixed configuration leads to the development of pressure hot spots in regions with a high current density. Thereby, pore closure of the separator is induced reducing the available capacity drastically by an increased polarization.

In case of an anode active material providing an embedded porosity, the volume expansion can be reduced by a combination of an adjusted density on electrode level together with a heavy compression on cell level. In addition, the lifetime of these cells is prolonged significantly. However, due to the void space provided in the composite material, this improvement comes at the expense of the volumetric energy density.

Finally, the results of the pouch cells are transferred to a prismatic cell format consisting of Si/C-anodes ( $\sim 50$  wt% Si) and Ni-rich cathodes. Employing operando expansion and X-ray computer tomography measurements, the mechanical deformation of the jelly roll during the compressed and uncompressed cycling is evaluated. The lifetime of the prismatic cells can be prolonged by mechanical compression.

Aging processes and expansion behavior of next-generation active materials are investigated as functions of mechanical compression as well as of the cell geometry, therefore this work provides a new baseline for a well-defined implementation of these materials in future applications. The understanding of the effects of mechanical pressure on the electrodes, the pouch cells, and the prismatic cells facilitates the design and the development of modules and packs and can promote the extensive utilization of Si as active material in LiB applications.

## Contents

Kurzzusammenfassung .....	II
Abstract .....	IV
Contents .....	VI
1 Introduction and motivation.....	1
2 Fundamentals and methods.....	4
2.1 Lithium-ion batteries .....	4
2.2 Aging mechanisms .....	7
2.3 Electrochemical impedance spectroscopy .....	8
2.3.1 Modeling of the full cell EIS measurements in non-blocking condition .....	9
2.3.2 Modeling of the symmetrical cell EIS measurements in blocking condition .....	12
3 Experimental: Electrodes, test cells and electrochemical characterization .....	15
3.1 Electrode preparation .....	15
3.2 Test cells.....	17
3.2.1 Symmetrical electrode and separator cells.....	17
3.2.2 Reference electrode cells .....	18
3.2.3 Stacked pouch cells.....	19
3.2.4 PHEV1 cells.....	20
3.2.5 Testing of aged electrodes in coin cells .....	20
3.3 Electrochemical characterization and testing.....	21
3.4 Mechanical characterization.....	26
4 Effects of the mechanical pressure on the electrodes and the full cells.....	27
4.1 Nonlinear compressibility of electrodes and stacks .....	27
4.2 Ionic pore resistance of compressed electrodes and separators .....	30
4.3 Full cell impedance of compressed cells correlated to their performance .....	32
4.4 Summary of the influence of mechanical pressure .....	37
5 Influence on the aging of C/Si NMC811-cells with a high expansion .....	38
5.1 Cyclic aging and volume expansion in dependency of the applied pressure .....	38
5.2 Aging mechanisms of cells under a heavily fixed and flexible compression .....	40
5.3 Impact of the absence of a mechanical pressure .....	50
5.4 Summary of the influence of mechanical pressure on C/Si NMC811-cells.....	58
6 Influence on the aging of Si/C NMC811-cells with particle included porosity.....	60

6.1	Pressure-dependent cyclic aging and expansion.....	60
6.1.1	Cyclic aging and pressure distribution .....	61
6.1.2	Post-mortem investigations .....	64
6.1.3	Summary of the influence of mechanical pressure.....	69
6.2	Cathode potential shift .....	71
6.3	Upscaling to PHEV1 cell format .....	74
7	Comparison of the effects of mechanical pressure on Si-containing Li-ion cells.....	84
7.1	Volumetric energy density and lifetime.....	84
7.2	Comparison of the pressure distribution and the expansion .....	88
7.3	C-rate capability.....	89
7.4	Summary of all contributions .....	90
8	Conclusion and outlook.....	93
	References .....	IX
	Nomenclature.....	XXI
	Abbreviations .....	XXII
	Supplementary Material .....	XXIII
	Danksagungen .....	XXVI
	List of publications .....	XXVII
	Curriculum vitae .....	XXIX





# 1 Introduction and motivation

One of the greatest challenges for the future generations are to shift the power supply towards renewable energies as well as to enable an emission-free transport. This includes not only the change from conventional power plants i.e. oil, coal, and gas to renewable energy generation but also decentralized energy storage or energy storage for the purpose of transportation. One promising storage technology applicable for a wide range i.e. portable consumer devices, stationary energy storages, and battery electric vehicles (BEVs) is the Li-ion battery cell (LiB) technology. Especially the demand for LiBs in BEVs is rising rapidly. According to the Zentrum für Sonnenenergie- und Wasserstoff-Forschung (ZSW), the number of new approvals for BEVs in Germany has more than doubled from 2017 to 2018 to a number of 67 504.<sup>1</sup> However, numerous stringent requirements have to be fulfilled to enable the extensive utilization of LiBs in BEV applications. According to Fraunhofer ISI, the gravimetric and the volumetric energy and power density, the cycle life, the fast charging ability, and the safety of LiBs are of high importance.<sup>2-4</sup> Ideally, all of these quality characteristics are provided at low costs. However, the current costs for one kilowatt hour lie between 150 – 300 €/kWh on cell level depending on their geometry and the goal is a cost reduction to below 100 €/kWh until 2030.<sup>2,5</sup> A high gravimetric and volumetric energy density is necessary to meet the demands of rising driving ranges targeting 500 km at a low mass and volume of the battery system.<sup>6</sup> Today, volumetric energy densities vary between 230 – 350 Wh L<sup>-1</sup> for prismatic cells and 250 – 450 Wh L<sup>-1</sup> in case of pouch cells.<sup>2</sup> Gravimetric energy densities of 120 – 140 Wh kg<sup>-1</sup> and 150 – 180 Wh kg<sup>-1</sup> are reported for the prismatic and pouch cell geometries, respectively.<sup>2,7,8</sup> Both are aimed to be increased to values > 1000 Wh L<sup>-1</sup> and > 350 Wh kg<sup>-1</sup> in 2030. To enable a fast acceleration in the BEV, a high power density has to be achieved at the same time. This means, the LiB needs to provide a high discharge current rate, also called C-rate capability. But also regarding the fast charging, the LiB needs to meet certain demands i.e. to be fully charged within 10 – 15 mins.<sup>6</sup> Apart of several developments on pack, module, and cell level, the composition of the electrodes in the Li-ion cells has a severe influence to achieve the aforementioned requirements. Therefore, several approaches on the active material level are on the roadmaps for today's research and development on LiBs. Figure 1.1 provides an overview of different negative and positive electrode active materials frequently reported in literature.<sup>2,6</sup> Today in most of the commercially available LiBs, graphite and Li[Ni<sub>0.1</sub>Mn<sub>0.1</sub>Co<sub>0.1</sub>]<sub>2</sub>O<sub>2</sub> (NMC111) represent the majority of the negative and the positive active materials, respectively. However, the specific capacity of graphite is limited to 372 mAh g<sup>-1</sup> and of NMC111 to < 155 mAh g<sup>-1</sup> (at a limited potential of 4.3 V vs. Li/Li<sup>+</sup>).<sup>11-13</sup> To meet the requirements of a high energy density, materials providing higher specific capacities have to be applied. On the side of the positive electrode, active materials containing higher contents of Ni i.e. NMC532, NMC622, and NMC811\* are promising to increase the specific capacity.<sup>4,13</sup> As a mid-term prospect, materials containing silicon oxide (SiO<sub>x</sub>) have been the focus of attempts to increase the theoretic capacities of the nega-

\*Li[Ni<sub>1-x-y</sub>Mn<sub>x</sub>Co<sub>y</sub>]<sub>2</sub>O<sub>2</sub> with x = 0.3, y = 0.2 for NMC532, x = 0.2, y = 0.2 for NMC622, and x = 0.1, y = 0.1 for NMC811.

tive electrode.  $\text{SiO}_x$  containing electrodes are generally promising due to the extremely increased specific capacity of Si compared to graphite. At elevated temperatures of 415 °C, specific capacities of up to 4200 mAh g<sup>-1</sup> were reported during the lithiation of Si to the most Li-rich phase of  $\text{Li}_{22}\text{Si}_5$ .<sup>14–16</sup> The theoretic capacity of the lithiation of Si to  $\text{Li}_{15}\text{Si}_4$  is limited to 3579 mAh g<sup>-1</sup> at room temperature.<sup>17–19</sup> Unfortunately, the lithiation of Si is accompanied by a large drawback, i.e. the high volume expansion of the Si of up to 300% of its initial size.<sup>20</sup> According to several reports,  $\text{SiO}_x$  offers the chance of a high cycle life with an improved specific capacity e.g. by encapsulating the  $\text{SiO}_x$  in a vertical graphene to buffer the volume expansion<sup>21</sup> or by nitrogen doping and embedding in a carbon matrix.<sup>22</sup> Still,  $\text{SiO}_x$  suffers from disadvantages like a poor electric conductivity and a high irreversible losses in the first cycle > 20%.<sup>23,24</sup> Negative electrode materials containing a certain amount of pure Si are a promising approach to increase the energy density at a concurrently high power density due to lower coating thicknesses. Currently, the amount of Si in commercial LiBs is not higher than 5 wt% as was shown by Richter et al.<sup>25</sup> The reason for this is the high volume expansion of the Si putting new challenges on the LiB development.

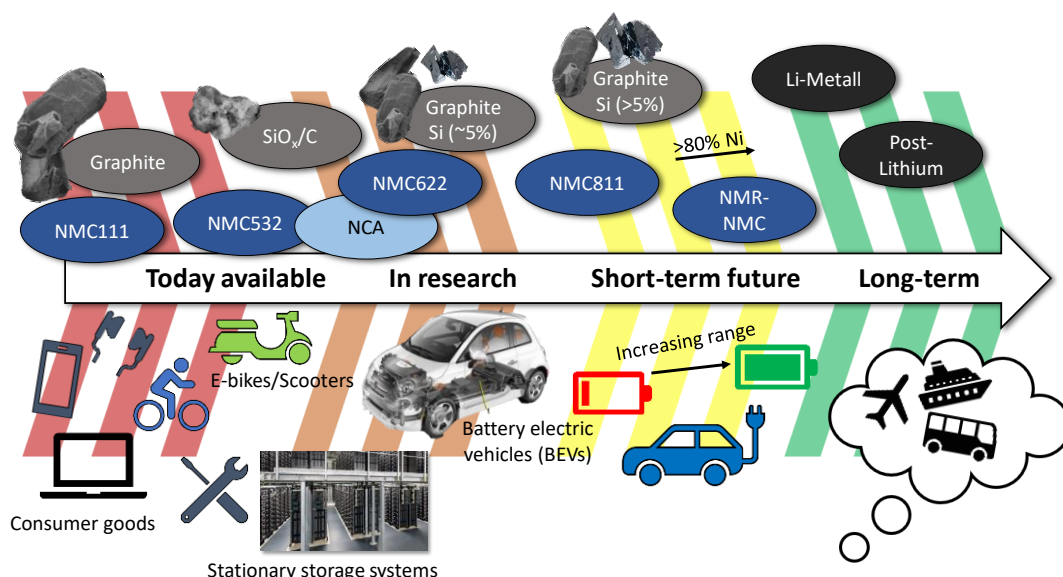


Figure 1.1: LiB roadmap regarding different today's and future negative and positive electrode active materials as well as certain LiB applications.

The high volume expansion of the Si not only brings up particular challenges during the operating the cells in a module or pack constraint. In addition, several accelerated aging mechanisms are triggered on the electrode level. The repetitive expansion/shrinking of the Si in the active material during the lithiation/delithiation causes particle cracking, detachment of active material regions, and delamination from the current collector. This in turn results in the electric disconnection and therefore, the increase of the cell impedance and a strongly accelerated capacity fading.<sup>14,17,19,23,26–31</sup> In literature, reports of the high cycle life and the high capacity of tested Si-containing active materials are published. Interestingly, most of the reports are either based on lab scale electrode coatings with areal capacities lower than 2.0 mAh cm<sup>-2</sup> or the cycling results are obtained in small coin cells.<sup>21,22,32–37</sup> To meet the future requirements, areal capacities higher than 3.0 mAh cm<sup>-2</sup> and the application of the material in large format cells is of utmost importance.<sup>38</sup> As a matter of fact, the

reproducibility of the up scaling of results gained in small test cells to application relevant cell sizes i.e. on pouch cells, cylindrical cells, or PHEV1 cells, is challenging. Hence, it is essential to evaluate these future materials on large-scale electrodes and cells. The behavior of these future materials needs to be well understood to enable an optimization on electrode and cell level. Apart from the fact that the performance of Si-containing electrodes can be improved by the selection of the binders<sup>35,39–43</sup> and the conductive agent<sup>44</sup> of the electrode, the utilized electrolyte,<sup>36,45–50</sup> or the cycling conditions,<sup>30</sup> approaches on full cell level are required. The application of a mechanical pressure on these cells to counteract the volume expansion and to enlarge the cycle life is one promising perspective. Because there are only rare studies on larger Si-containing cells, there is a lack of knowledge regarding the influence of mechanical pressure on the performance and the aging behavior of those cells. Only few groups already reported of an improved performance of compressed Si-containing cells without giving a deep insight into the underlying aging mechanisms.<sup>51–53</sup>

Hence, the main purpose of this work is to combine different approaches i.e. the mechanical compression, the microstructural properties of the Si-containing material, and the cell geometry with the aim to identify crucial coherences and their interactions with the performance of the cells. The influence of mechanical pressure will be analyzed on electrode, pouch cell up to prismatic cell level enabling the comprehensive understanding of the materials' aging and expansion behavior in industrial-scale cell formats. The selected negative electrode active materials are a composite of carbon (C) and Si mixed with graphite (~8 wt% Si). This material will be referred to as C/Si-composite. Furthermore, a Si-rich composite embedded in a C-matrix (~50 wt% Si) is utilized and will be referred to as Si/C-composite. Both negative electrodes are tested in full cells with a Ni-rich positive electrode (NMC811). As a state-of-the-art material, graphite and NMC622 are evaluated as negative and positive electrode in graphite|NMC622-cells and are tested under the same conditions as the C/Si|NMC811- and Si/C|NMC811-cells, respectively. Most of the tests are performed on basis of stack-type pouch cells. After a brief introduction of the theory regarding LiBs, their aging mechanism, and electrochemical impedance spectroscopy (EIS) in section 2, the experimental electrode and cell preparation as well as the electrochemical testing is described in section 3. In the results part, section 4 discusses the effects of mechanical pressure on the electrode and the cell level with the aim of understanding the interaction of the compression of electrodes with their performance in stacked pouch cells. Subsequently, the influence of mechanical pressure on the two different systems with the C/Si-composite exhibiting a large volume expansion and on Si/C-composite with ~50 wt% Si providing an intrinsic porosity to buffer the volume expansion is evaluated in section 5 and 6, respectively. In addition, the influence of the cell geometry on the aging and the expansion behavior of the Si/C-composite paired with the NMC811-electrode is determined by the up scaling from pouch cells to large-scale prismatic cells in section 6.3. Finally, the results gained on basis of the two different Si material concepts are compared in terms of state-of-the-art specifications i.e. the volumetric energy density, the behavior of the pressure and the expansion, the current rate capability, and the safety in section 7. Section 8 provides the conclusion and the outlook of this work.

## 2 Fundamentals and methods

### 2.1 Lithium-ion batteries

The first commercial LiB was introduced by Sony in 1991.<sup>54</sup> Nowadays, LiBs are playing a major role and are utilized in almost all portable electric devices such as smartphones, laptops, or power tools. And their market is constantly increasing.<sup>4,55–57</sup> A LiB consists of several main components such as the negative electrode, the positive electrode, the separator, and the electrolyte. During the discharge of the Li-ion cell, oxidation reactions take place at the negative electrode. At the same time, reduction reactions occur at the positive electrode. It is commonly accepted to refer to the negative electrode as anode and the positive electrode as cathode during both, charging and discharging of the cell. Hence, the negative and the positive electrode will be referred to as anode and cathode, respectively. Graphite is extensively utilized as anode active material due to a number of advantages as its theoretical specific capacity of  $372 \text{ mAh g}^{-1}$ , a low electrochemical potential for the de-/intercalation of  $0.05 - 0.3 \text{ V vs. Li/Li}^+$ , and a flat potential curve.<sup>4,11,54,55</sup> As cathode active material, the current developments are focusing on layered oxides as Lithium-Nickel-Manganese-Cobalt-Oxides,  $\text{Li}[\text{Ni}_{1-x-y}\text{Mn}_y\text{Co}_x]\text{O}_2$  (NMC) and Mn-spinel materials. The separator in the LiB serves as electric insulator between the anode and the cathode as a protection from short circuits and is permeable for  $\text{Li}^+$ . Commonly, materials as polyethylene (PE), polypropylene (PP), and combinations of both are utilized. These materials are chemically stable towards electrolytes and exhibit a high porosity of around  $40 - 50\%$  to enable the passage of  $\text{Li}^+$ . In addition, several approaches regarding ceramic coatings on the separator have been made to decrease safety risks, e.g. preventing thermal runaways.<sup>58</sup> Besides the porosity of the separator, the  $\text{Li}^+$  conductivity of the electrolyte in LiBs has a severe impact on the cell performance. To assure a high conductivity in a wide temperature and voltage range, the electrolyte is a combination of solvents such as dimethyl carbonate (DMC), ethyl methyl carbonate (EMC), ethylene carbonate (EC), diethyl carbonate (DEC), and a conductive Li salt, Lithium fluorophosphates ( $\text{LiPF}_6$ ). In addition, several additives are used to improve e.g. the film formation or the voltage stability of the electrolyte.<sup>55</sup> In case of Si-containing anode materials, electrolytes with specific amounts of fluoroethylene carbonate (FEC) are utilized. The FEC improves the SEI formation on the anode surface and increases the  $\text{Li}^+$  conductivity of the resulting film.<sup>36,45,49,59</sup>

Figure 2.1 schematically describes the main processes that take place during the charging of a LiB. As aforementioned, the cathode is subjected to electrochemical oxidation reactions releasing  $\text{Li}^+$  into the electrolyte and electrons  $e^-$  into an external electric circuit (shown in Figure 2.1 as process b). Electrically conductive agents like carbon black provide the electronic transport throughout the electrode. The  $\text{Li}^+$  dissolves into and migrates within the electrolyte through the porous separator towards the anode. After reaching the surface of the graphite particle, intercalation starts, whereas the charge of one  $\text{Li}^+$  ion is equalized by one  $e^-$  as the  $\text{Li}^+$  is intercalated between the graphene sheets by charge transfer reaction after stripping the solvent molecules (shown in Figure 2.1 as process a). The Li is diffusing

from the surface of the active material to the inside of the particle. To ensure electric conduction, both active materials are coated on current collector foils, consisting either of Al for the cathode or Cu for the anode. To guarantee the adhesion and mechanical stability of the electrode microstructures, binders are utilized.

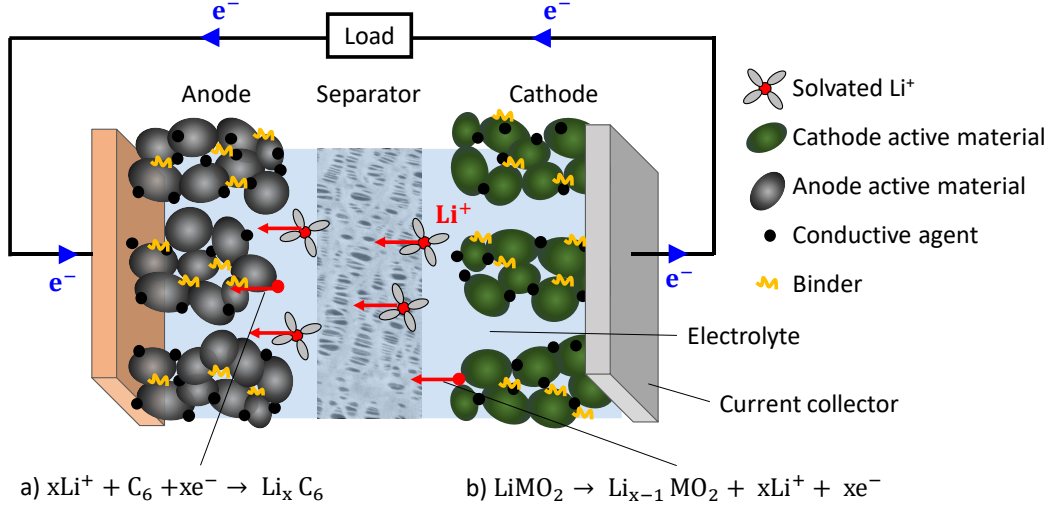


Figure 2.1: Schematic illustration of the functionality of a Li-ion battery cell during the charging process.

The intercalation of the Li in graphite is taking place stepwise in distinct stages which are influenced by the energy necessary to expand the van der Waals gap between the graphene layers and the repulsive interactions of the  $\text{Li}^+$ .<sup>11</sup> These stages can be determined as plateaus from the potential curve. During the intercalation of the  $\text{Li}^+$ , the hexagonal (AB) structure of the graphite is transformed to an AA-structure. The distinct stages are  $\text{LiC}_{36-50}$ ,  $\text{LiC}_{25-30}$ ,  $\text{LiC}_{18}$ ,  $\text{LiC}_{12}$  and  $\text{LiC}_6$ .<sup>11,60-62</sup> Thereby, the distance between the graphene layers is increasing around 10.3% to reach  $\text{LiC}_6$ .<sup>17,63,64</sup>

The implementation of elementary Si into graphite increases the energy density of the anode active material. Contrary to the Li intercalation into graphite, the lithiation of Si can be described by an alloying process.<sup>11</sup> The crystalline Si is lithiated by a two-phase mechanism leading to the amorphization of the pristine Si to form  $\text{Li}_x\text{Si}$ . At high temperatures (415 °C), the lithiation passes four intermediate equilibrium phases  $\text{Li}_{12}\text{Si}_7$ ,  $\text{Li}_7\text{Si}_3$ ,  $\text{Li}_{13}\text{Si}_4$ , and  $\text{Li}_{22}\text{Si}_5$  resulting in a theoretic specific capacity of 4200 mAh g<sup>-1</sup> in the fully lithiated form.<sup>14</sup> However, at room temperature, the lithiation of the Si exhibits a flat voltage plateau at around 0.1 V. Several groups found that the highest lithiation phase at room temperature is  $\text{Li}_{15}\text{Si}_4$  which is formed at a potential of 50 mV vs. Li/Li<sup>+</sup> where the amorphous Si converts to a crystalline phase with a theoretic specific capacity of 3579 mAh g<sup>-1</sup>.<sup>17-19</sup> During the lithiation of the amorphous Si, the material is subjected to extreme volume changes of up to 300%.<sup>20</sup> These high internal stresses lead to particle cracking, a poor electrical contact, and capacity fading. Hence, the Si should be cycled above the 50 mV vs. Li/Li<sup>+</sup> in the fully amorphous range.<sup>19</sup>

Regarding the positive electrode, Ni-rich NMCs provide advantages as an increased specific capacity above 200 mAh g<sup>-1</sup> for NMC811.<sup>8</sup> However, their stability suffers with an

increased amount of Ni. The most common aging mechanisms of those NMCs will be explained in section 2.2 and experimental results will be discussed in section 6.2.

During the first charging of the full cell, the so-called Solid Electrolyte Interphase (SEI) is formed with the products of electrolyte decomposition at the negative electrode, causing an irreversible capacity loss (ICL) in the first cycle. In 1979, Peled first evaluated and introduced the SEI.<sup>65</sup> The SEI provides the protection of the anode particles against further electrolyte decomposition in the subsequent cycles, inhibits exfoliation, and is highly permeable for  $\text{Li}^+$ .<sup>66,67</sup> Its stability depends on various influences such as the components of the electrolyte, the anode active material, and the formation protocol.<sup>66–68</sup> Especially, when regarding Si-containing anode, the influence of the film formation agents in the electrolyte are essential. According to several studies, the utilization of FEC as an additive for Si-anodes improves the passivation ability and increases the Coulombic efficiency.<sup>36,45–47</sup>

Thereby, the **Coulombic efficiency** is defined as the ratio of the discharge to charge capacity and is given in percentage. During the cycling, the **charge and discharge capacities** of the LiBs are defined as the integral of the charge/discharge current over time, which is necessary to reach the upper/lower voltage limit. To enable the comparison of the cyclic aging and to evaluate the **capacity fading** of the test cells at different conditions, the **relative capacity** is defined as the capacity in each cycle divided by the capacity of the first cycle whereas the cells are charged/discharge at the same current based on their positive active material. This charging/discharging current is often referred to as **C-rate**, which is defined as the applied current divided by the capacity of the LiB. This means a C-rate of 1C for a LiB with a capacity of 25 Ah charged at 25 A. Because the mechanical pressure applied on the surface of the cells influences the available capacity strongly, the capacity and the corresponding C-rate is selected based on the average discharge capacity of the cells after the formation and the same currents are applied for all cells consisting of the same active material. The capacities determined for the different cell configurations will be shown in section 3.2.3 in Table 3.3. Another important definition is the **state of charge (SOC)** of a LiB. The SOC is the ratio of the charge capacity at a particular cell voltage within the voltage window divided by the overall available charge capacity when reaching the upper voltage limit.

During the cycling of the cells, the preferred charging protocol is a sequence of constant current (CC) and constant voltage (CV), which is referred to as **CC/CV charging**.<sup>69–72</sup> Firstly, the LiB is charged at a constant current until a certain upper voltage limit is reached. Secondly, the voltage is kept constant, which leads to a decrease of the charging current with an increasing SOC. As soon as the current drops below a particular previously fixed minimum value, the charging process is finished and the next step of the test program is initiated.

In addition to the “full cell” consisting of a graphite/Si-anode and an NMC-cathode introduced in Figure 2.1, Li metal electrodes can be utilized as counter electrode to characterize the anode or the cathode in so-called “half-cells”. To evaluate the ionic pore resistance of either the anode, or the cathode, “symmetrical cells” are used consisting of two anodes or two cathodes, respectively.



## 2.2 Aging mechanisms

According to Vetter et al., the degradation of carbonaceous anodes can be mainly contributed to changes of the electrode/electrolyte interphase during the cycling of the cell.<sup>73</sup> Even though, the SEI formation takes place during the initial formation cycles, its growth proceeds during the cycling and the storage of the cells.<sup>74</sup> Consequences are an increased cell impedance, directly affecting the available cell capacity and the loss of cycleable Li (ICL).<sup>73,75</sup> Preferred at low temperatures and high C-rates, Li can be deposited as Li metal on the anode surface accelerating the cell aging and increasing the safety risks.<sup>76</sup> When regarding Si/C-composite anodes, the degradation mechanisms are even more wide-ranging. Due to the extreme volume expansion of the Si,<sup>20</sup> the protective SEI is subjected to high tension forces during the lithiation leading to cracks. Si is exposed towards the electrolyte and is covered by a new SEI in every cycle consuming electrolyte and active Li. The gradual thickening of the SEI can cause the electric isolation of some particles of the anode.<sup>77–79</sup> In addition, the repetitive expansion during the lithiation and the shrinking during the delithiation of the anode can lead to particle-particle contact loss, cracking of Si particles, and detachment of some active regions.<sup>23,73,80</sup> This accelerates mechanical degradation and the loss of active anode material.<sup>75</sup>

As aforementioned in the introduction, Ni-rich NMC is on its way to become the state-of-the-art cathode material in LiBs. Increasing the Ni content in the NMC increases the specific capacity and satisfies the need for higher energy densities. At the same time, a higher Ni content brings in several challenges contributing to an enhanced aging. The predominant state of the Ni-ions in the charged state is  $\text{Ni}^{4+}$ . This species is highly reactive towards both, the solvent molecules and the conductive salt of the electrolyte, leading to undesired side reactions. This is not only causing safety concerns, but can also result in gas formation and the consumption of cycleable Li reducing the available capacity. Another well-known failure mechanism often observed when investigating the aging processes of Ni-rich layered oxides is the so called cation mixing process. Cations from the transition metal sites mix with  $\text{Li}^+$ . Preferably  $\text{Ni}^{2+}$  mixes with the  $\text{Li}^+$  when highly delithiating the NMC due to their similar radii of 69 pm and 76 pm, respectively.<sup>13,81,82</sup> However, the migration of Mn and Co was observed as well in literature.<sup>83</sup> Irreversible cation mixing also called layered-to-spinel transition reduces the amount of cycleable Li and hinders the diffusion in the Li layers both resulting in capacity fading.<sup>84</sup> Contrariwise, reversible cation mixing can lead to crack formation due to the induced stress.<sup>85,86</sup> One approach to prevent cation mixing, is the introduction of dopants like  $\text{Mg}^{2+}$ ,  $\text{Al}^{3+}$  or  $\text{Zr}^{4+}$ .<sup>13,81,87,88</sup> The appropriate dopant is inserted in the Li layer to stabilize the structure repelling transition metals. Other groups pursued the strategy of synthesizing NMC with a Ni-rich core but a Mn-rich shell to reduce the amount of  $\text{Ni}^{4+}$  exposed at the surface of the particles.<sup>89</sup>

The NMC-particles (secondary particles) are composed of primary crystallites (primary particles) with a diameter of 0.5 – 1.0  $\mu\text{m}$ . Especially, the Ni-rich NMCs tend to the formation of micro cracks along the grain boundaries of these primary particles. This microstructural failure is mainly caused by the lattice changes induced by the removal of the Li



during the delithiation.<sup>13,90–92</sup> Consequently, the electrodes suffer from contact loss. In addition, pristine active material is exposed to the electrolyte enabling uncontrolled side reactions in each cycle.<sup>84</sup> According to literature, especially NMC811 tends to crack formation when delithiated to potentials above 4.3 V vs. Li/Li<sup>+</sup>.<sup>84,93</sup>

## 2.3 Electrochemical impedance spectroscopy

The electrochemical impedance spectroscopy (EIS) is a very powerful method for the investigation of the internal processes in Li-ion cells.<sup>94–98</sup> The complex cell impedance is determined by the application of a sinusoidal current or voltage signal at a frequency  $f$  (galvanostatic and potentiostatic stimulation) and the respective voltage or current response is measured. Under the conditions of linearity and time invariance,<sup>94</sup> the electrical impedance can be determined from the ratio of the Fourier transformed voltage and current signal as follows

$$Z(j\omega) = \frac{\mathcal{F}(u(t))}{\mathcal{F}(i(t))} \quad (2.1)$$

whereas the impedance  $Z(j\omega)$  depends on the angular frequency  $\omega$  which is defined as

$$\omega = 2\pi f. \quad (2.2)$$

To determine the complete impedance spectrum of the cell, the measurement has to be repeated for various frequencies  $f$ . This enables the evaluation of different occurring processes in the cell at various time constants. The method is very sensitive to interferences e.g. from the inductance of the cables to the contacts of the cells.<sup>99,100</sup> Hence, the same measurement conditions are applied for all the cells tested in this work. In addition, the test setup introduced in Figure 3.5 enables Kelvin contacting in order to reduce the ohmic impedance of the contacting and of the measuring cables. The measurements are performed in a temperature-controlled room to minimize fluctuation. The status of the cell and therefore the time invariance of the system can further be compromised, by self-discharge, aging, or changes of the SOC during the measurement. Thus, the measurement time is kept as short as possible by the utilization of the multi-frequency mode. Furthermore, the measurements of the full cells are conducted galvanostatically to keep a constant SOC. The EIS measurements of the symmetrical cells are performed potentiostatically under blocking conditions, which means that intercalation processes are inhibited. The amplitude of the stimulation is minimized, so that the conditions of linearity are kept.

The resulting EIS spectrum can be analyzed by the modeling of equivalent circuit (EC) elements to quantify the ongoing electrochemical processes. Sections 2.3.1 and 2.3.2 give further explanations on the utilized models for the full cell and symmetrical cell measurements, respectively.

### 2.3.1 Modeling of the full cell EIS measurements in non-blocking condition

Figure 2.2 summarizes all relevant ongoing transport processes involved in the electrochemical reaction and the associated EC elements for a Li-ion full cell. At the porous electrode/electrolyte interphase transport processes are distributed at different times, thus this unit is too complex to be described by a simple parallel circuit of a resistance and a capacitance to represent the charge transfer process of the electrode. It is necessary to take all processes at the porous electrode/electrolyte interphase into account.<sup>101,102</sup> When a full cell is regarded, different electrochemical processes are taking place at the same time, which are schematically illustrated in the pores of the electrode in Figure 2.2b and c. The main contributions to the EIS spectra are: the resistance  $R_L$  parallel to the inductance  $L$  representing the inductivity of the cables and cell terminals, the electric resistance in the current collectors and the cell terminals  $R_{Ce}$ , the interfacial contact of the active material particles and the current collector  $R_{Co}$ , and the ionic transport in the electrolyte filled pores  $Z_P$ .<sup>101,103–105</sup>  $Z_P$  has to be separated into an ohmic contribution from the separator  $R_{P,S}$  and a more complex term describing the resistance within the electrodes' pores. This includes the charge-transfer processes for the Li-ion insertion into the active material particles represented by a parallel  $R_{CT}$  and double-layer capacitor  $C_{dl}$  and the diffusion within these particles, described by a Warburg impedance  $Z_W$ .<sup>101,103,104</sup>

$Z_P$  is closer regarded in Figure 2.2a, representing the ionic resistance of the electrolyte in a porous electrode, which can be described by the theory of the transmission line model (TLM) for cylindrical pores. The  $e^-$  transport inside the solid phase is represented by  $R_{El}$  and in the electrolyte phase by  $R_P$ . Additionally, the charge is transferred between the solid and the electrolyte phase via charge-transfer reactions which are shown as RC elements  $Z_{CT}$ .<sup>106</sup> The pressure sensitive contribution of  $R_P$  to the full cell spectra will be an important factor in this work because of its strong influence on the performance of the compressed cells. However, the contribution of  $R_P$  cannot be determined from EIS measurements of the full cells.<sup>101,103,107,108</sup> Therefore, symmetrical cell measurements in blocking conditions are necessary and will be presented in section 2.3.2.

Furthermore, the formation of a SEI layer at the electrode/electrolyte interphase, especially of the anode, can influence the EIS spectra and can be modeled by an additional resistance in parallel to a capacitance. For reasons of clarity, Figure 2.2 does not include this contribution. The ionic transport in the separator  $R_{P,S}$  cannot be separated from the electric resistance of the current collectors  $R_{Ce}$  in full cells and is often count to the total ohmic high-frequency resistance  $R_{HF}$  of the cell. Its contribution can be determined by the shift of the EIS spectra along the real axis. The interface between the current collector and the active material layer of both electrodes  $R_{Co}$  is contributing to the EIS spectra of the cells at high frequencies.  $R_{Co}$  depends on the adhesion of the electrode, the quality of the coating, and the calendaring process. Furthermore, Nara et al. reported that the value is strongly affected by the densification of the electrodes.<sup>104</sup> Due to the fact that the electrodes in this work are industrial grade coated with an optimized adhesion and most of the cells are tested under

mechanical compression, the influence of the interfacial contact can be neglected in the further considerations.

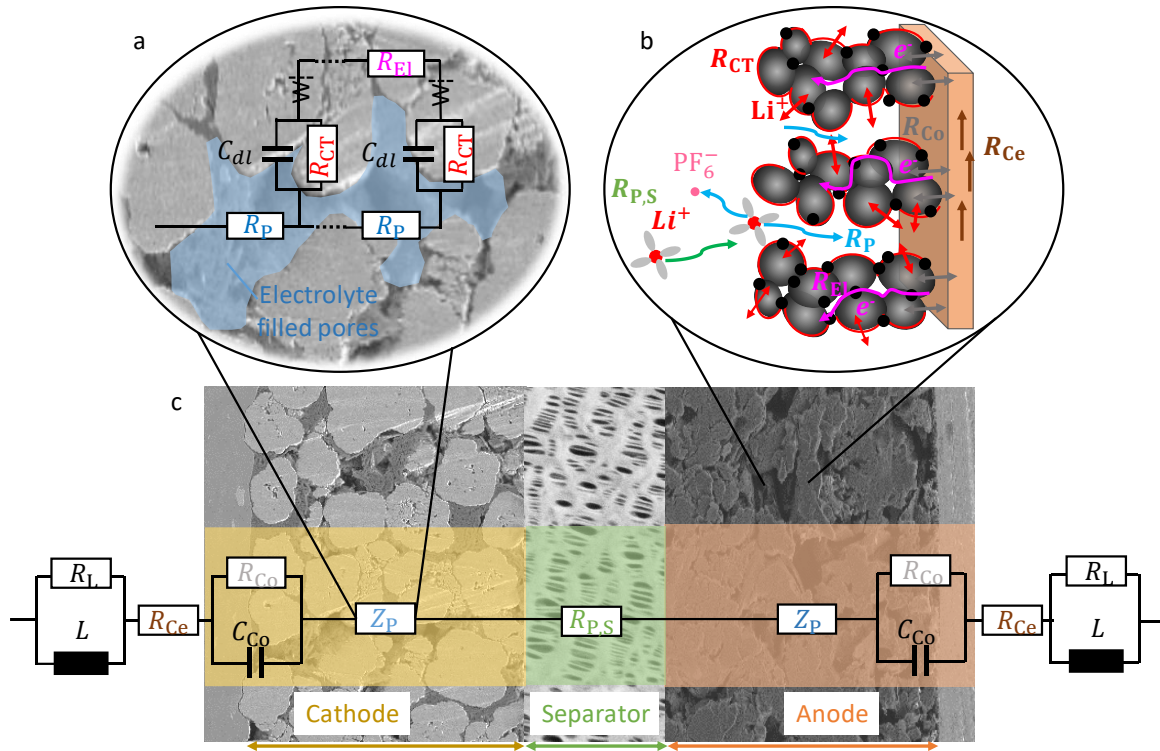


Figure 2.2: Schematic illustration of the equivalent circuit (a) and the electrochemical processes (b) in the pores of the electrodes, and the associated equivalent circuit elements in a Li-ion full cell (c).

According to Landesfeind et al., the modeling of EIS measurements utilizing the EC shown in Figure 2.2a requires the ability of separating the contributions from the anode and the cathode as well as the measurement in blocking and non-blocking conditions.<sup>103</sup> Blocking conditions can be realized by suppressing the faradaic charge-transfer processes in the pores of the electrodes i.e. by the utilization of a  $Li^+$ -free electrolyte or by the measurement in symmetrical cell setups at certain conditions. Both methods will be explained in section 2.3.2. Furthermore, the utilization of a three-electrode cell setup with a Li reference electrode in between the anode and the cathode is required to distinguish anode and cathode contributions to the spectrum.<sup>103</sup> Further information on the reference cell setup is provided in section 3.2.2. However, by inserting a Li reference in the electrode stack, the application of a homogeneously distributed pressure on the surface of the electrodes is impeded. Since the EIS measurements will be applied to analyze the aging of differently compressed cells, which are required to be compressed with a homogeneous pressure distribution, the implementation of a Li reference is impossible. Therefore, in this work, a simplified EC model will be utilized to analyze full cell EIS measurements and the spectra will be compared regarding the high frequency resistance  $R_{HF}$  and the sum of all charge-transfer contributions.

Figure 2.3 shows the utilized simplified EC model for the evaluation of the full cell impedance spectra. It consists of an inductance  $L$  in parallel with a resistance  $R_L$  to account for

the high frequency inductive tail in the spectrum.<sup>109–111</sup> The high frequency resistance  $R_{\text{HF}}$  summarizes the contributions of the electric contacts  $R_{\text{Ce}}$  and the ionic pore resistance of the separator  $R_{\text{P,S}}$  in the full cell. Since the cell contacts and the cables are staying the same during the measurement,  $R_{\text{Ce}}$  is expected to stay constant while changes in  $R_{\text{HF}}$  can most likely be contributed to  $R_{\text{P,S}}$ . The mid frequency region of the spectra depicting the charge-transfer processes of the anode, of the cathode as well as the polarization of the electrode/electrolyte interphase (SEI) is modelled with three parallel  $R||\text{CPE}$  elements in series.

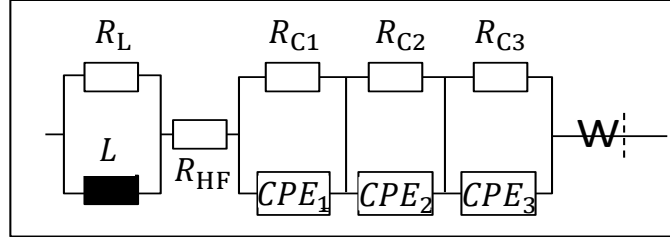


Figure 2.3: Equivalent circuit to model the full cell impedance.

From literature, it is well known that the quality of the fitted spectrum is improved when constant phase elements (CPE) are used instead of double-layer capacitors.<sup>112,113</sup> The CPE describes a non-uniform double-layer capacitor. The impedance  $Z_{R||\text{CPE}}$  of the resulting  $R||\text{CPE}$  element is

$$Z_{R||\text{CPE}} = \frac{R}{1 + (j\omega RC)^n} \quad (2.3)$$

whereas  $n$  is a value between 0 and 1. In case  $n = 1$ ,  $Z_{R||\text{CPE}}$  becomes a parallel  $R||C$  element, which results in a perfect semicircle in the Nyquist plot of the spectrum. For values of  $n < 1$ , the semicircle is attenuated in direction of the imaginary axis, while the value for  $R$  stays constant.

The diffusion at low frequencies is represented by a finite-length Warburg element  $Z_W$ , which may be written as

$$Z_W = R_{D0} \cdot \tanh(B\sqrt{j\omega}) \quad (2.4)$$

with  $B = l_{\text{diff}}/\sqrt{D}$  and  $D$  is the diffusion coefficient of the diffusing particle and  $l_{\text{diff}}$  is the diffusion length.<sup>94,114</sup>  $Z_W$  exhibits a 45°-slope for high frequencies when plotted in the complex plane and converges to the diffusion resistance  $R_{D0}$  for low frequencies.<sup>94</sup>

As was shown by other groups before, a Li reference would be necessary to distinguish the contributions of the anode and the cathode processes.<sup>95,112,115</sup> Since the full cells are tested under a mechanical pressure in this study, an inserted Li reference would be damaged and the homogeneous application of pressure on the electrode stack would be disturbed. Therefore, the contribution of the  $R||\text{CPE}$  elements cannot be separated. The occurring charge-

transfer processes in the cells will be discussed as the sum of charge-transfer resistances  $R_{CT\_sum}$ . The data was processed in Matlab employing a nonlinear least-square optimization (see (S0.1) in the supplementary material) based on the EC presented in Figure 2.3. The fitting function can be found in the supplementary material in (S.02).

In a full cell, the distinction of the influence of the applied mechanical pressure on the ionic pore resistance  $R_p$  of the separator, the anode, and the cathode is impossible. Therefore, symmetrical cell measurements in blocking condition are conducted.

### 2.3.2 Modeling of the symmetrical cell EIS measurements in blocking condition

The impedance measurement of symmetrical electrode cells is a non-invasive method to determine the impedance of either the anode or the cathode without the utilization of a Li metal reference.<sup>101–103,106,107,116</sup> This method enables the determination of the ionic pore resistance  $R_p$  as indicator for the ionic mobility in the pores of porous electrodes and of the separator. The impedance of a symmetrical cell is measured in blocking condition, i.e. no charge transfer processes take place. In this case, the EIS model introduced earlier in Figure 2.2 can be simplified. The blocking condition can be achieved either by the utilization of two pristine anodes or cathodes, respectively, or by the usage of a Li free electrolyte. In case of testing of pristine electrodes, no effective faradaic reaction is taking place. For a pristine anode, the Li concentration  $c_s$  of the active material is zero and for a pristine cathode  $c_s$  is equal to the maximum available Li concentration  $c_{s,max}$ . The surface current density  $i_0$  is given as

$$i_0 = F(k_a)^{1-\alpha}(k_c)^\alpha(c_{s,max} - c_s)^{1-\alpha}(c_s)^\alpha \left( \frac{C_l}{C_{l,ref}} \right)^\alpha \quad (2.5)$$

derived from the Butler-Volmer equation,<sup>117</sup>  $i_0$  gets zero for both cases when  $c_s = 0$  or  $c_s = c_{s,max}$ . When utilizing a blocking electrolyte,  $i_0$  is also negligible because  $C_l/C_{l,ref} = 0$ .<sup>118</sup>

In blocking condition, the charge transfer processes are negligible and the ionic pore resistance can be calculated under the utilization of the non-faradaic transmission line model (TLM).<sup>101–103,106,107,118</sup> Figure 2.4a represents a typical Nyquist impedance plot of a symmetrical electrode cell measurement. It is clearly visible that the spectrum is not influenced by an interfacial contact resistance which would appear as semicircle in the high frequency region of the Nyquist impedance plot and was reported in literature by Landesfeind et al.<sup>103</sup> and Gaberscek et al.<sup>119</sup> In contrast to their work, all the tested symmetrical cells herein are characterized under a mechanical compression whereas the contribution of the interfacial contact between the electrode layer and the current collector is minimized and can be neglected.<sup>104</sup> Figure 2.4b shows the schematic illustration of the simplified TLM which is achieved under the assumption that the electronic resistance in the solid phase  $R_{El}$  is negligibly small compared to the ionic pore resistance  $R_p$  ( $R_{El} \ll R_p$ ). This condition is given

by the presence of well distributed conductive carbon additives.<sup>101,106,120,121</sup> The ionic pore resistance of the anode and the cathode ( $R_{P,A}$  and  $R_{P,C}$ ) can be calculated from the TLM impedance  $Z_{TLM}$  as

$$Z_{TLM} = \sqrt{\frac{R_P}{Q(j\omega)^\gamma}} \coth \left( \sqrt{R_P Q(j\omega)^\gamma} \right) \quad (2.6)$$

by fitting the measurement data.

Figure 2.4a shows that the ionic pore resistance  $R_P$  can also be evaluated by the linear extrapolation of the low and high frequency region onto the x-axis. The intercept of the high frequency region provides the value of the high frequency resistance  $R_{HF}$ . By employing the Maclaurin expansion of the TLM function in (2.5) and for  $\omega \rightarrow 0$ ,<sup>122</sup>  $R_P$  can be written as

$$\lim_{\omega \rightarrow 0} \text{Re}\{Z_{TLM}\} = \frac{R_P}{3} + R_{HF} \quad (2.7)$$

and is often utilized in literature.<sup>101,106,107</sup>

Whereas,  $R_{HF}$  sums up the contributions from the electric resistance of the electrodes, the contact resistances, and the ionic resistance of the electrolyte filled pores of the separator.

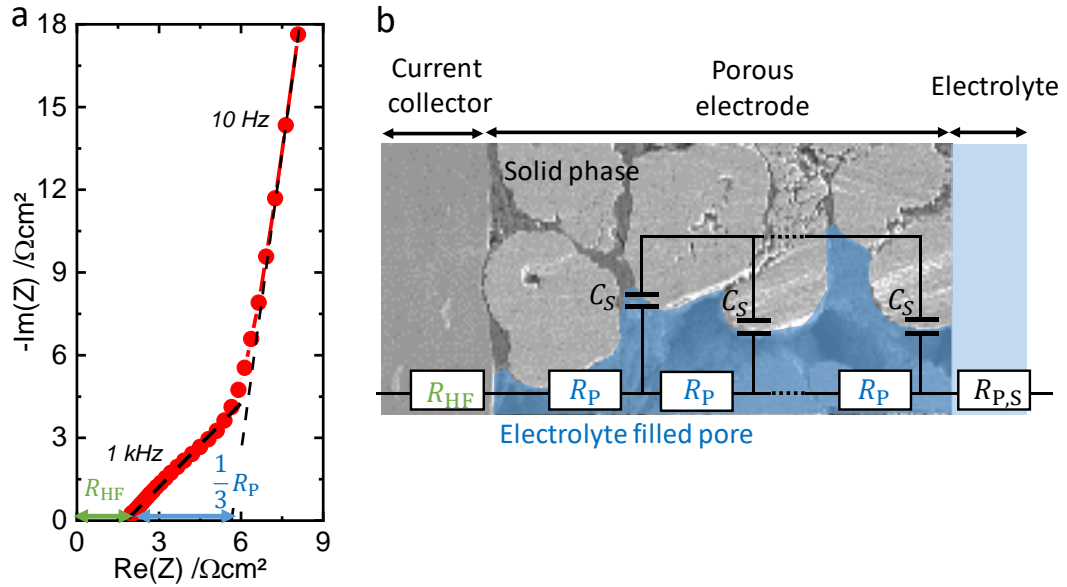


Figure 2.4: (a) Schematic Nyquist impedance plot of a symmetrical cell measurement in blocking condition- and (b) schematic illustration of the simplified transmission line model with  $R_P \gg R_{EL}$  (TLM).

The ionic resistance  $R_P$  in the electrolyte filled pores of the electrodes and the separator<sup>102,106,107</sup>

$$R_p = \frac{\tau}{\varepsilon} \cdot \frac{d}{A \cdot \kappa} \quad (2.8)$$

depends on the tortuosity  $\tau$ , the porosity  $\varepsilon$  as well as on the geometrical parameters of the electrode like the thickness  $d$  and the area  $A$ , and on the electrolyte's conductivity  $\kappa$ .

The tortuosity  $\tau$  is defined as<sup>106,123</sup>

$$\tau = \frac{l}{L} \quad (2.9)$$

depending on the total transport path  $l$  through the pore structure and the straight thickness of the electrode  $L$ , shown in Figure 2.5.

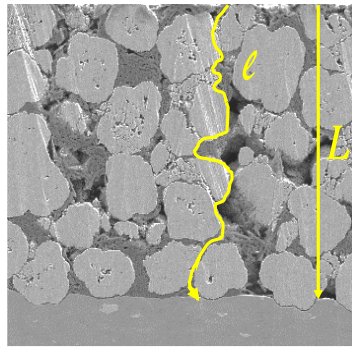


Figure 2.5: Schematic illustration of the tortuosity  $\tau$  of an electrode.

The impedance of the separator  $Z_{\text{sep}}$  can be written as

$$Z_{\text{sep}} = R_{p,s} + \frac{1}{Q_s(j\omega)^\gamma} \quad (2.10)$$

by a serial connection of the ionic resistance in the separator  $R_{p,s}$  and a *CPE*.<sup>106</sup>

The ionic pore resistances  $R_p$  is normalized on the surface  $A$  of the measured electrode.



### 3 Experimental: Electrodes, test cells and electrochemical characterization

#### 3.1 Electrode preparation

For this thesis, two cathode active materials, NMC622 and NMC811, were utilized. These will be referred to as NMC622- and NMC811-cathode in the following. Graphite and two different Si-containing composite materials were tested as anode. The utilized Si-composite materials differ in terms of their particle structure and their Si content. The first Si based anode material has an overall Si content of  $\sim 8$  wt% and consists of Si/C-particles and graphite particles (see schematic illustration in Figure 3.1 a). It will be declared as C/Si-anode. Additionally, a second Si/C-composite material with an approx. Si content of  $\sim 50$  wt% embedded in a C-matrix with integrated porosity was utilized. Figure 3.1 b gives a schematic illustration of this Si/C-composite anode. The particles are coated to prevent electrolyte insertion in the particle structure. In the following, this material will be named Si/C-anode. Further information about the synthesis of the Si/C-composite can be found in our previous paper.<sup>124</sup>

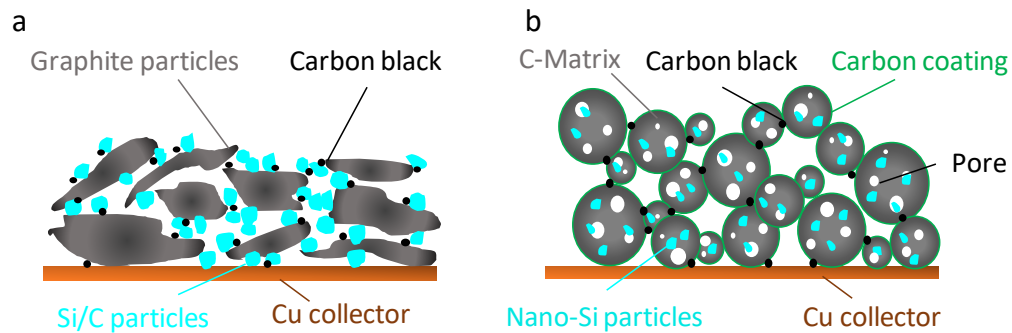


Figure 3.1: Schematic illustration of the C/Si-anode (a) and the Si/C-anode (b).

The anode and the cathode slurries were prepared in planetary mixers (PMH, Netzsch GmbH) of different batch sizes of 10 L or 60 L according to the respective application. For the cathode slurries, a binder solution of 7 wt% polyvinylidene fluoride (PVDF) in 1-methyl-2-pyrrolidone (NMP) was prepared. The conductive graphite (2 wt%) and the carbon black (2 wt%) were stirred before the active material was added stepwise. To prepare the anode slurries, the active material, the carboxymethyl cellulose (CMC) and the conductive agent (carbon black) were first dry mixed before deionized water was added stepwise. After a kneading time of 2 h to prevent agglomerates, styrene-butadiene rubber (SBR) was mixed in at a lower speed. For the graphite- and the C/Si-anode, the mixing ratio was 94 wt% active material with 2 wt% CMC, 2 wt% SBR, and 2 wt% carbon black. To adjust the rheological parameters of the Si/C-slurry, the CMC content was increased to 4 wt% reducing the active material content to 92 wt%. The slurry for the PHEV1 cells had to be adjusted and consisted of 92.5 wt% Si/C-active material, 3 wt% CMC, 2.5 wt% SBR, and 2 wt% carbon black. After the mixing process, the anode and the cathode slurries were coated by a continuous slot die coating process on the Cu-foil (6  $\mu\text{m}$  in case of the graphite-anode,



11  $\mu\text{m}$  for the C/Si- and Si/C-anodes) and Al-foil (20  $\mu\text{m}$ ), respectively. The coating speeds differed between 1.5 - 4  $\text{m min}^{-1}$ . During the coating process, the mass loading was controlled by an ultrasonic distance measurement system. Furthermore, the coater includes five individually adjustable drying zones with an overall length of 16 m. Temperatures between 50 – 80  $^{\circ}\text{C}$  are set to guarantee an optimized drying result. Afterwards, the electrodes were calendered to a defined porosity. Due to the risk of breaking the complex structure of the Si/C-particles (see Figure 3.1b), the Si/C-anode was evaluated calendered and uncalendered. Table 3.1 and Table 3.2 summarize all relevant characteristics of the utilized anode and cathode coatings, respectively.

Table 3.1: Characteristics of the utilized anode coatings.

Parameter	Graphite-anode	C/Si-anode	Si/C-anode (calendered)	Si/C-anode (uncalendered)
Si-content in wt%	-	$\sim 8$		$\sim 50$
Mass loading in $\text{mg cm}^{-2}$	8.6	5.9		6.3
Active material content in %	94	94		92
Density in $\text{g cm}^{-3}$	1.45	1.3	0.9	0.74
Porosity in %	41.5	41.1	50.4	53.9
D50 <sup>*1</sup> in $\mu\text{m}$	22.5	10.1		20.1
One-sided coating thickness in $\mu\text{m}$	59.5	46.0	72.5	85.5
Reversible capacity in $\text{mAh (g}_{\text{AM}})^{-1}$	335	576	560 (limited)	
Areal capacity in $\text{mAh cm}^{-2}$	2.71	3.19		3.26

Table 3.2: Characteristics of the utilized cathode coatings.

Parameter	NMC622-cathode	NMC811-cathode
Mass loading in $\text{mg cm}^{-2}$	15.0	15.4
Active material content in %	94	94
Density in $\text{g cm}^{-3}$	3.4	3.3
Porosity in %	27.5	24.4
D50 in $\mu\text{m}$	11.5	12.0
One-sided coating thickness in $\mu\text{m}$	46.0	48.5
Reversible capacity in $\text{mAh (g}_{\text{AM}})^{-1}$	155 @ 1C <sup>*2</sup>	175 @ 1C <sup>*2</sup>
Areal capacity in $\text{mAh cm}^{-2}$	2.47	2.75

The theoretic capacity of the Si/C-anode is much higher than 560  $\text{mAh (g}_{\text{AM}})^{-1}$ . However, the concept of this material is to provide free porosity inside of the particles for the expected volume expansion of the Si. Hence, the capacity of this material is limited to this dictated value ensuring the buffering of the volume expansion of the Si without breaking the C-matrix. The partial lithiation provides further advantages in regards of the lifetime of the material.<sup>125</sup> The relevant capacity values of the electrodes shown in Table 3.1 and

<sup>\*1</sup> Diameter of 50% of the particles are smaller than the D50 value.

<sup>\*2</sup> The reversible capacities of the cathodes are provided for a C-rate of 1C.

Table 3.2 were determined by half cell measurements and the porosities by mercury porosimeter measurements. The values for the particle size distribution were measured by laser diffraction (Mastersizer, Malvern Instruments).

After the coating and before the cell assembly, the electrodes were punched, or laser cut to the respective formats and additionally dried under vacuum at 120 °C for 16 h.

## 3.2 Test cells

For electrochemical testing, different cell formats were utilized which are summarized in Figure 3.2 schematically. All cells were assembled in the dry room with a dew point below -60 °C.

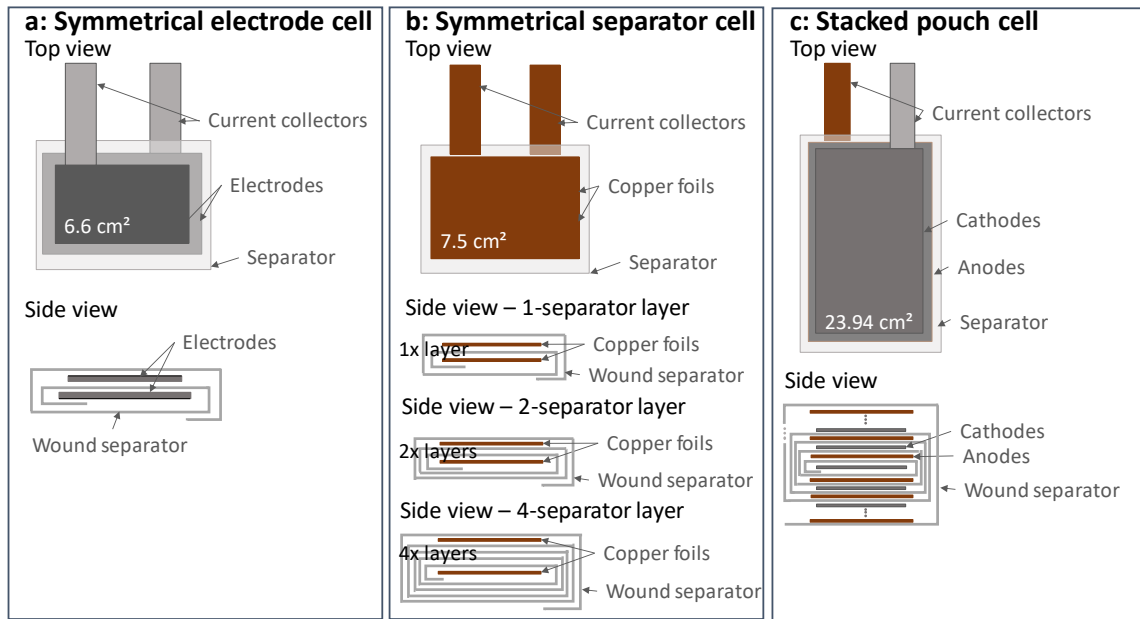


Figure 3.2: Schematic illustration of the symmetrical electrode-cell (a), the symmetrical separator cell(b), and the stacked pouch cell (c). Reused in parts with permission of the Journal of Power Sources.<sup>126</sup>©2019 Elsevier B.V.

### 3.2.1 Symmetrical electrode and separator cells

The symmetrical electrode cells (see Figure 3.2a) for the EIS measurements presented in section 4.2 were assembled from two laser cut anodes or cathodes, respectively. Thereby, the active area of the first electrode was 6.6 cm². To prevent misalignment, the second electrode was designed larger. The separator (Celgard2325) was wound around the electrode sheets, the cell tabs were ultra-sonically welded, and the final stack was sealed in the pouch bag.

The separator cells (see Figure 3.2b) were built utilizing two copper foils with an active area of 7.5 cm². Cells with different number of separator layers were assembled. The copper foils were wrapped into the separator so that 1-, 2-, and 4-separator layers lie in between the copper foils. Finally, the cell tabs were ultra-sonically welded on the copper current collectors and the separator stack was sealed in the pouch bag.

After overnight drying under vacuum at 80 °C, the symmetrical cells were filled with 0.4 mL electrolyte in the glovebox. To generate comparable conditions with the pouch cells, 1 M LiPF<sub>6</sub> in EC:DEC 3:7 with 2 wt% vinylene carbonate (VC) was utilized for the symmetrical graphite- and NMC622-electrode cells and 1 M LiPF<sub>6</sub> in EC:DEC 3:7 with 10 wt% (FEC) for the symmetrical C/Si-, Si-/C-, and NMC811-cells. The electrolytes 1 M LiPF<sub>6</sub> in EC:DEC 3:7 with 2 wt% VC and 1 M LiPF<sub>6</sub> in EC:DEC 3:7 with 10 wt% FEC will be referred to as electrolyte A and B, respectively. Electrolyte A shows a conductivity  $\kappa$  of 0.691 Sm<sup>-1</sup>, electrolyte B of 0.713 Sm<sup>-1</sup> at 25 °C.

Furthermore, symmetrical separator and electrode cells were assembled from post-mortem harvested separators and electrodes. The separators and electrodes were harvested in an Ar-filled glovebox, three times dip washed in DMC for 60 sec in different containers and dried under vacuum for 18 h before they were re-assembled in symmetrical cells for further testing. An electrode area of 6.6 cm<sup>2</sup> was laser cut from the harvested electrode sheets of the cycled pouch cells. To enable the contacting of the electrode, the coating had to be removed via laser ablation. Since no blocking condition could be guaranteed for the aged electrodes, a Li-free electrolyte consisting of 0.5 M tetrabutylammonium hexafluorophosphate (TBA-PF<sub>6</sub>, Alfa Aesar) in EC:EMC 3:7 was utilized for these cells. This electrolyte will be referred to as electrolyte C in this work. It has a conductivity  $\kappa$  of 0.613 Sm<sup>-1</sup>. Since the electrodes had to be exposed to dry room atmosphere and to the energy of laser radiation, only electrodes free of Li deposition could be re-assembled. Due to the high reactivity of the partially lithiated Si/C-anodes, it was not possible to harvest these electrodes without safety concerns.

The EIS measurements of the symmetrical cells were conducted at a VMP3 battery tester with a VMP3 booster (Biologic). The frequency range was set to 1 Hz to 300 kHz with potentiostatic stimulation with an amplitude of 10 mV. The data evaluation was conducted with MATLAB with a self-written script applying the TLM function (2.6) introduced in section 2.3.2.

### 3.2.2 Reference electrode cells

To analyze the potential of the anode and the cathode separately in section 6.2, reference electrode cells in a three-electrode configuration were assembled. The cells consisted of one anode and one cathode sheet, which were both single-sided coated and mechanically punched to an area of 26.00 cm<sup>2</sup> and of 23.94 cm<sup>2</sup>, respectively. The anode and the cathode were wound in the separator with the coating facing each other. Thereby, two separator layers were put in between the anode and the cathode. The reference electrode was made of a thin Cu tab and was isolated by a Kapton film. Metallic Li was pressed at the tip of the Cu tab. The reference electrode was inserted between the two separator layers at the side of the anode tab. The sealing of the pouch bag made sure that the reference electrode is kept at its place during the measurement. After drying the cells overnight at 80 °C under vacuum, the cells were filled with 0.9 mL electrolyte B. The cell setup was utilized to characterize the cathode potential shift of the NMC811-cathode. For this reason, cells were

assembled consisting of a Si/C-anode and a NMC811-cathode as well as of a graphite-anode and a NMC811-cathode (electrode data see Table 3.1 and

Table 3.2). The formation as well as the cycling of the cells was conducted utilizing a VMP3 battery tester (Biologic). For the formation, three cycles at C/10 and for the cycling 100 cycles with a CC/CV charge at C/3 to C/20 and a 1C discharge were performed in a voltage window of 2.7 – 4.2 V. The discharge capacity of the cells in the third formation cycle was  $61.33 \text{ mAh} \pm 0.44 \text{ mAh}$ . A number of three cells consisting of the graphite- and three cells of the Si/C-anodes were tested together with the NMC811 as cathode.

### 3.2.3 Stacked pouch cells

Stacked pouch cells were assembled from mechanically punched anode and cathode sheets with an area of  $26.00 \text{ cm}^2$  and of  $23.94 \text{ cm}^2$ , respectively. The electrode stacks were assembled using a semi-automatic winding-stacking machine inside of the dry room after overnight drying at  $120^\circ\text{C}$  under vacuum. Graphite-anodes and NMC622-cathodes were selected as reference system without Si and stacked to a 27-layered stack consisting of 13 cathodes and 14 anodes. After pre-testing these cells, the number of layers in the stack was reduced to a 13-layer configuration consisting of 6 cathodes and 7 anodes of the C/Si- or Si/C-anode with the NMC811-cathodes. Table 3.3 shows all relevant parameters of all stacked cells including the nominal capacities and the cell geometries.

After the cell assembly, the cells were transferred to an Ar-filled glovebox, dried overnight at  $80^\circ\text{C}$ , and filled with the respective electrolyte. An amount of 5 mL electrolyte A was defined for the graphite|NMC622-cells to be enough to wet the complete electrode stack without leaving an excess of electrolyte in the cell. The C/Si|NMC811-cells were filled with 2.75 mL of electrolyte B. Due to the high porosity and the hygroscopic behavior of the Si/C-active material, the amount of electrolyte B was increased to 3.5 mL for the Si/C|NMC811-cells. After the electrolyte filling, all stacked pouch cells were compressed in their respective test configuration, which is described in section 3.3. After an electrolyte soaking time of 18 h, the cells were cycled three times at C/10 in the operation voltage window of 2.7 – 4.2 V for the formation.

Table 3.3: Characteristics of the utilized pouch cells.

Parameter	Graphite  NMC622-cell	C/Si NMC811-cell	Si/C NMC811-cell
Stack configuration	13x cathodes, 14x anodes	6x cathodes, 7x anodes	
Stack thickness in $\mu\text{m}$	4054	1700	2019 (calendered), 2161 (uncalendered)
Cell capacity in Ah	1.4	0.75	0.75
Geometrical cathode area in $\text{cm}^2$		23.94	
Geometrical anode area in $\text{cm}^2$		26.0	

### 3.2.4 PHEV1 cells

To analyze the behavior of the Si-containing anodes in larger cell formats, PHEV1 cells were manufactured at the ZSW in-house research production line. The cells were assembled from the Si/C-anodes and the NMC811-cathodes with a width of 144.50 mm and 138.80 mm and a length of 4.20 m and 3.94 m, respectively. This means a total active surface area of 10937.4 cm<sup>2</sup>. After over-night drying under vacuum at 120 °C, the jelly rolls were wound in a fully automated winding machine. Figure 3.3 shows the resulting jelly roll. Afterwards, the jelly rolls are pressed at an elevated temperature, the active material free edges of the anode and the cathode were tacked, and the cell cap with terminals was ultra-sonically welded. The resulting component consisting of the jelly roll connected to the cap was fitted in the cell housing and sealed by a laser welding process (see Figure 3.3 for a final PHEV1 cell). After a final heating step of the cells at 80 °C in the glovebox, the cells were filled with 120 g of electrolyte B. Subsequently, the cells are pre-charged to 3.7 V at C/10 with an opened filling hole in the glovebox to enable the escape of the formation gas.

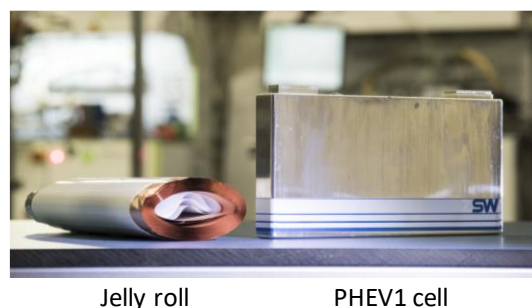


Figure 3.3: Jelly roll and final PHEV1 cell.

Finally, the cells were closed and three times cycled CC/CV at C/10 until C/20 in a voltage window of 2.5 V – 4.2 V for the formation. The average discharge capacity at C/10 of the cells was determined to be  $27.9 \pm 0.2$  Ah with an ICL of  $18.0 \pm 0.24\%$  during the first cycle.

To evaluate the swelling of the jelly roll in the PHEV1 cell, 3D computer tomography measurements (CT) were conducted of the cells after the production, after the formation, and after the cycling. A microfocus X-ray tube (Modell GE Phoenix v | tome | x 300) was employed and the measurement data was processed with Datos.

### 3.2.5 Testing of aged electrodes in coin cells

Electrodes were harvested post-mortem and were re-assembled in coin cells. Therefore, the pouch cells were CC/CV discharged until C/20 to the lower cut off voltage of 2.7 V and the cells were opened in an Ar-filled glovebox within the next hour. After the cell opening, the electrodes were three times dip-washed in DMC in different containers and dried over-night under vacuum at 120 °C. This procedure was proposed by our in-house post-mortem experts to maintain the cell components in a very similar way as during the cell operation.<sup>127</sup> Afterwards, the electrodes were mechanically punched to a diameter of 12 mm and assembled in coin cells (CR2032) vs. Li-metal with fresh electrolyte. To analyze the thickness

and mass increase of the cycled electrodes, the punched electrodes were weight and the thickness was determined. The procedure was repeated at least three times.

After a soaking time of 4 h, the cells were cycled two times in the voltage window of 1.5 – 0.02 V for the anodes and 3.0 – 4.3 V for the cathodes at a battery test system (Basytec CTS). The current was set to C/10 based on the remaining capacity of the before cycled pouch cells. Figure 3.4 shows these two cycles of an aged cathode in the re-assembled coin cell configuration. The first delithiation of the harvested cathode to the upper voltage limit of 4.3 V extracts the remaining cycleable Li out of the cathode host. This value enables the calculation of the loss of cycleable Li (ICL) of the aged cell by subtracting the determined remaining amount of Li capacity from the initial capacity of the cathode (see Figure 3.4). In the subsequent cycle, the empty Li sites of the aged cathode are occupied with  $\text{Li}^+$  provided from the Li-metal counter electrode. The thereby available capacity exhibits the remaining available capacity of the NMC. The difference of this remaining capacity of the NMC and the initial capacity is defined as the NMC loss (see Figure 3.4). This procedure of determining the ICL and the NMC loss will be utilized to characterize the aged test cells post-mortem in sections 5.2 and 6.1.2.

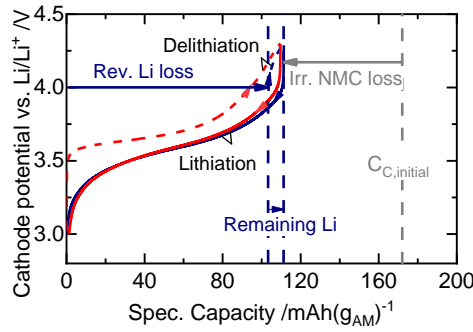


Figure 3.4: Determination of remaining reversible Li content and irreversible NMC loss.

Furthermore, C-rate tests have been performed to test the remaining rate capability of the anodes for a quantitative comparison between different cycling conditions. The anodes were lithiated CC/CV with C/3 until C/20 and delithiated at various current densities from 0.2  $\text{mA cm}^{-2}$  to 1.85  $\text{mA cm}^{-2}$ .

For the Si/C-anodes, a capacity-limited charge-process is recommended by the manufacturer, i.e. 560  $\text{mAh (g}_{\text{AM}})^{-1}$ . Therefore, the electrodes could not be tested with a voltage limitation.

### 3.3 Electrochemical characterization and testing

To evaluate the influence of mechanical compression on the performance and the aging of the test cells, a special test device has been developed. Figure 3.5a shows a CAD drawing of the in-house developed and constructed bench vise enabling the application of a defined pressure on the cell in the inner cell fixture. A defined force can be adjusted on the cell in the inner fixture via the integrated force sensor (load cell, Haehne RKS01A) with a high accuracy of 0.5%. This inner cell fixture can be individually equipped with springs or with stiff pipes to enable either a “flexible compression” or a “fixed compression” configuration (compare Figure 3.5b and c). After the adjustment of the requested force on the cell, the



screws of the inner cell fixture are fixed, and the fixture can be taken out of the bench vice for subsequent testing of the included cell. Furthermore, this inner fixture enables Kelvin contacting. In case of the flexible compression configuration in Figure 3.5b, the cell is able to expand while the pressure on the cell is hold constant by the inserted springs. To enable the lowest possible force variations during the cell expansion, different kinds of springs (SuperSprings, Danly), each with a suitable spring constant for the required pressure level, were used. The springs, selected for the 0.08 MPa, the 0.42 MPa, and the 0.84 MPa flexible compression, exhibit a theoretical force variation of 2.04 N, 11.5 N, and 23.5 N for a maximum cell expansion of 30% of the initial stack thickness. This is around 2% of the initially applied forces. These force variations were confirmed in initial tests, where the force sensor was utilized to measure the pressure changes during the cell cycling. A displacement sensor is utilized to measure the expansion of the test cells during the cell operation with an accuracy of 0.1  $\mu\text{m}$  (Keyence GT2-P12). As can be seen in Figure 3.5c, stiff pipes can exchange the springs to enable testing under “fixed compression”. This means that the included cell is not able to expand and the pressure in the fixture is increasing.

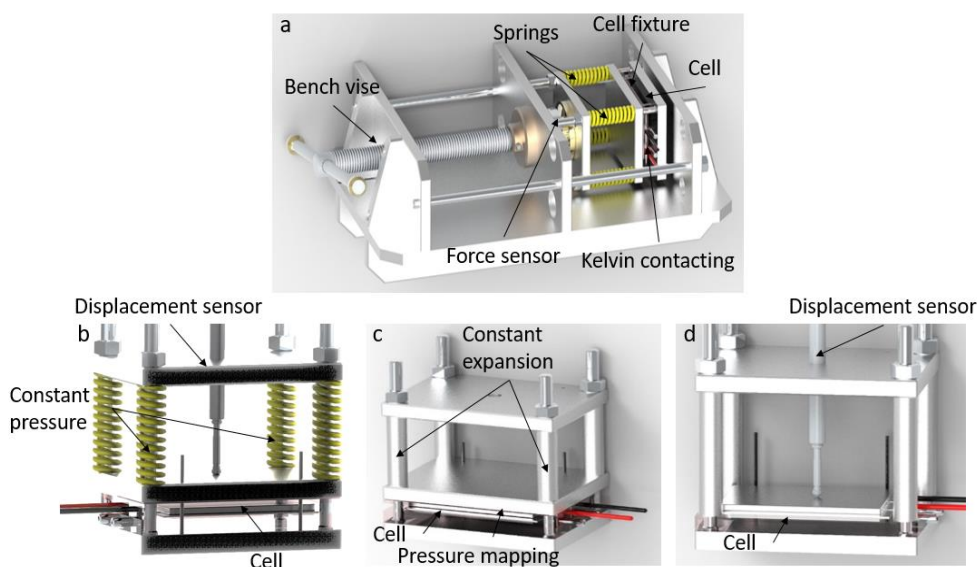


Figure 3.5: CAD image of the test setup for the pressure application (a) as well as the different pressure configurations: constant pressure (flexible compression) in b, constant expansion (fixed compression) in d, and uncompressed in c. Reused in parts with permission of the Journal of Power Sources and of the Journal of The Electrochemical Society.<sup>126,128</sup>©2019 Elsevier B.V. and ECS.

The utilized stiff pipes are made of Al 2024 with a diameter of 12 mm and a length of 50 mm with an inner hole of 6 mm, and an E-Module of 73.1 GPa. Finite elements method (FEM) simulations were performed to assess the deformation of the fixture under the maximum applied pressure of 0.84 MPa. Figure 3.6 shows the deformation at that applied pressure. The maximum deformation of the fixture under a load of 0.84 MPa is smaller than 3.5  $\mu\text{m}$  in the center parts and has a maximum of  $\sim 6 \mu\text{m}$  at the edges of the fixture.

The cells were compressed directly after the filling process and stayed at the specific pressure level during the formation, the cycling, and different other tests. The fixture was only released directly before the post-mortem investigation of the cells. This procedure ensured the reproducible handling of the cells. Since there is an unneglectable amount of gas formed

during the formation and the subsequent cyclic aging, the pouch cells were all equipped with a gasbag outside of the fixture. Hence, the formed gas is pressed out of the stack into the gasbag and the expansion measurements is not distorted.

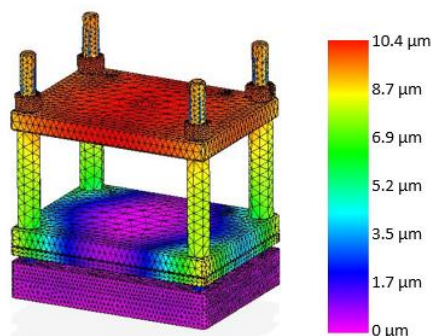


Figure 3.6: Deformation of the fixed compression fixture under 0.84 MPa outer pressure.

Operando pressure distribution measurements were conducted to evaluate the homogeneity of the pressure on the surface of the compressed pouch cells. Figure 3.7 demonstrates the principle of the pressure mapping system schematically.

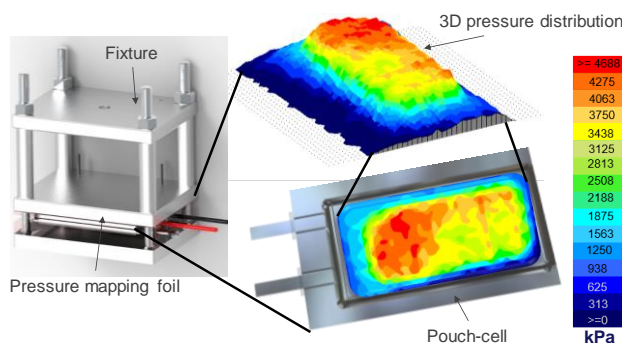


Figure 3.7: Schematic illustration of the setup for the pressure mapping on the surface of the compressed pouch cells. Reused in parts with permission of the Journal of The Electrochemical Society.<sup>128</sup> ©2019 ECS.

A pressure mapping foil (FlexiForce Sensor 5051 150 psi, Tekscan) can be placed on the cell's surface in the fixture and the pressure distribution can be monitored with a spatial resolution of 62 sensels/cm<sup>2</sup>. The bench vise with the load cell introduced in Figure 3.5a was utilized to calibrate the system. The calibration was repeated at five pressure levels. The pressure mapping foil was utilized to guarantee a homogeneous pressure distribution during the compression process of the cells. Furthermore, the pressure distribution of particular cells was monitored operando during the cycling. To track the total change of the pressure outside of the fixture, the load cell was utilized, whereas the pressure mapping foil enabled a spatially resolved measurement on the cell's surface.

To compare the cycling results of the compressed cells with the behavior of the uncompressed cells, some test cells were cycled without any compression. The cells were cycled in the exact same fixture but without any outer constraint (see Figure 3.5d) to enable comparable cycling conditions, especially in terms of the cell contacting. The reproducible expansion measurement of the uncompressed cells is facilitated by including thin Al plates



(1.5 mm) on the top and the bottom of the electrode stack in the cell (see Figure 3.8). Without these plates, the displacement sensor tip would penetrate the electrodes and would lead to artificial aging in this area, distorting the measurement.

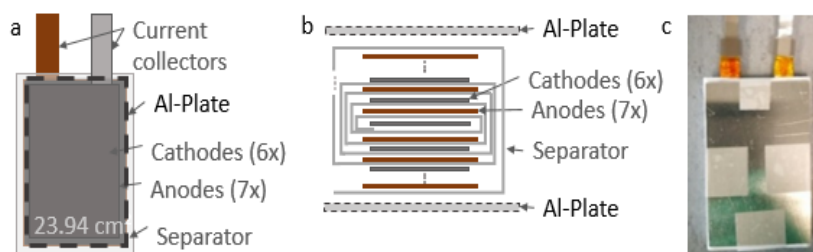


Figure 3.8: Cell design for the expansion measurement of uncompressed stacked pouch cells. Schematic illustration (a) and (b). Picture of the real cell setup (c).

Unfortunately, the literature on the application of mechanical pressure on LiBs is rare. Berckmans et al. investigated pouch cells at very soft compression up to 0.06 MPa even though they reported of an improved performance with an increased pressure.<sup>51,129,130</sup> Sauerteig et al. tested hard-case cells at a pressure of 0.07 MPa.<sup>116</sup> Louli et al. tested Si-containing pouch cells at a pressure of 0.34 MPa.<sup>131</sup> To cover a large area in this work, the cells were tested at 0.84 MPa, 0.42 MPa, and 0.08 MPa in the flexible and fixed configuration, respectively. Thereby, 0.42 MPa is equal to 1 kN force on the active cell area, 0.84 MPa to 2 kN. And a pressure of 0.08 MPa was selected, since it is the lowest achievable load in the introduced setup.

At least two to five cells were tested for each pressure level. The testing included the cycling with expansion measurement as well as EIS measurements after the formation and subsequently, after each 50 cycles at different SOC. A battery test system (Basytec CTS) was utilized to conduct the cycling. All cells were cycled with CC/CV charge at C/3 until C/20 and 1C discharge in the operation window of 2.7 – 4.2 V. Since the capacities of the cells depended largely on the particular compression configuration, the C-rate was determined based on the theoretical capacity of the cells, which is given in Table 3.3 for the different material combinations. Hence, every cell was loaded with the same current ensuring the comparability of the cycling results. Additionally, after every 50 cycles a C/20 charge/discharge cycle and a C-rate test was conducted. The C-rate test consisted of several cycles CC/CV charge at C/3 to 4.2 V until C/20 and discharge at different C-rates differing from C/3 to 2C to the lower cut off voltage of 2.7 V.

The EIS measurements of the full cells were performed using a VMP3 battery test system with a VMP3 booster (Biologic). The measurement was conducted with a galvanostatic stimulation at an amplitude of 10 mA in the frequency range of 10 mHz to 300 kHz. To measure the impedance spectra at defined SOCs, initially the discharge capacities were determined by a C/20 cycle. Afterwards, the cells were fully charged CC/CV to 4.2 V and then discharged stepwise to the particular SOCs. A relaxation time of 1.5 h was set before every EIS measurement. The impedance spectra were evaluated via EC fitting utilizing Matlab in accordance to the model introduced in 2.3.1. All electrochemical measurements were conducted at room temperature ( $25\text{ }^{\circ}\text{C} \pm 1\text{ }^{\circ}\text{C}$ ) in a climate-controlled room.

The expansion measurements were performed employing the displacement sensors via a serial interface and recorded with Python. The setup enables the parallel measurement of up to ten cells at the same time. The data was evaluated with self-written and automated Matlab scripts. Therefore, the Basytec data file and the expansion measurements were synchronized after the measurements by the time stamps. Figure 3.9 shows an example of the expansion of one cell during the three formation cycles. The irreversible (irr.) swelling, the reversible (rev.) swelling, and the sum of both, the total swelling, are determined for every cycle. Thereby, the irreversible swelling is defined as the expansion at the end of the discharge, the total swelling is the expansion at the end of the charge, and the reversible swelling is the difference of both. For a better comparison of the different cell types, the expansion will be given in percentage of the initial stack thickness of the cells (see Table 3.3).

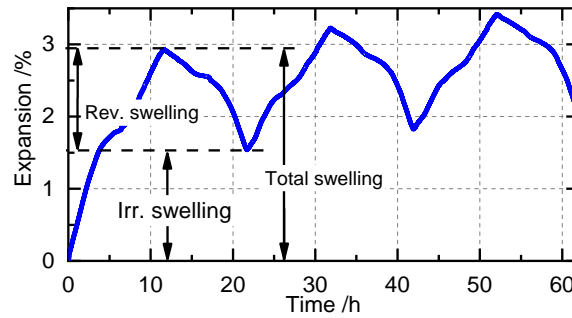


Figure 3.9: Example for Li-ion cell expansion with the definition of the reversible, the irreversible, and the total swelling.

The pressure and the expansion of the assembled PHEV1 cells were evaluated in an analogous way. Figure 3.10 shows the schematic illustration of a PHEV1 cell in a fixed (Figure 3.10a) and a flexible (Figure 3.10b) compression.

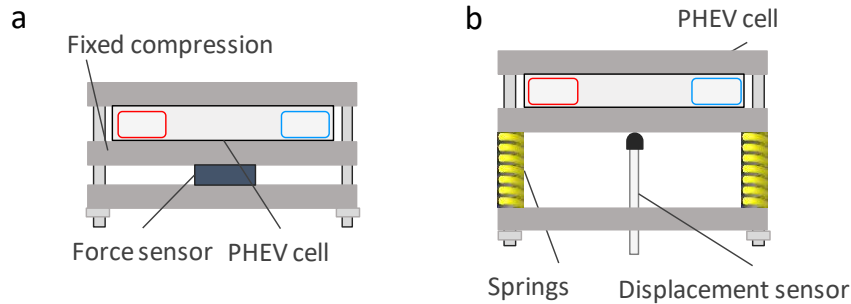


Figure 3.10: Schematic illustration of the fixed (a) and flexible (b) compression of the PHEV1 cells for pressure (a) and expansion (b) measurements.

For the fixed configuration, the cell is mounted between two steel plates and the force sensor is positioned between the middle and an outer plate. The complete fixture is placed in the bench vise shown in Figure 3.5a where the pressure is adjusted, and the outer screws are fixed. To achieve the flexible compression, springs were inserted. The expansion was measured with the displacement sensor introduced above. In both configurations, the cells were compressed to 0.1 MPa and cycled with a C/3 CC/CV charge until C/20 and 1C discharge in the voltage window of 2.7 – 4.2 V.

### 3.4 Mechanical characterization

The compressibility of all utilized anode and cathode coatings, the separator, the electrode stacks, and full cells was characterized. Figure 3.11 shows a schematic illustration of the measurement setup.

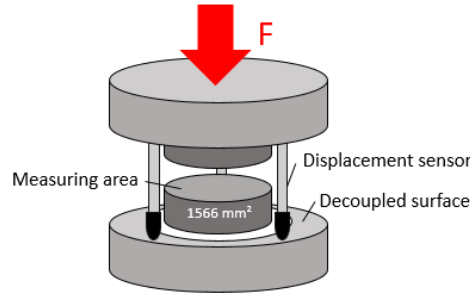


Figure 3.11: Schematic illustration of the compressibility measurement setup.

The measurement head shown in Figure 3.11 is employed in a tension and compression test machine (ProLine, ZwickRoell) for the compressibility measurement. The measurement head is in-house designed and is equipped with three high-precision displacement sensors (Dr. Johannes Heidenhain). These sensors enable the measurement of the compression of the tested material independently of the deformation of the traverse of the test machine. The electrodes, separators, stacks, or full cells were placed on the measurement head shown in Figure 3.11, which has a circular area of 1566 mm<sup>2</sup>. To investigate the influence of the number of layers in an electrode stack, the tests were performed with various number of layers of the probes. The number of tested layers varied from 1- to 14-layers. The same pressure level as for the full cell tests were applied on the probes (0.08 MPa, 0.42 MPa, and 0.84 MPa). Initially, a pressure of around 0.06 MPa was applied on the probe to close the gaps between the layers. Subsequently, the pressure on the probe was released again and compressed to the defined pressure levels. The displacement sensors measured the compressibility of the probes at a certain pressure. The resulting values were divided by the thickness of the probe and the number of tested layers resulting in the single layer compressibility. Table 3.4 provides the thicknesses of the tested probes.

Table 3.4: Thickness of the utilized materials for the compressibility measurement.

Material description	Thickness / $\mu\text{m}$
Graphite-anode	131
C/Si-anode	104
Si/C-anode	183 (uncalendered), 157 (calendered)
NMC622-cathode	112
NMC811-cathode	121
Separator	25

## 4 Effects of the mechanical pressure on the electrodes and the full cells

To understand the behavior of compressed LiBs, the general effects of the mechanical pressure on the electrochemical behavior of the electrode and the full cells have to be evaluated carefully. Initially, the compressibility of the electrodes and the stacks as well as the effects of the mechanical pressure on the ion mobility in the pores of the electrodes will be determined in section 4.1 and 4.2. Subsequently, the behavior of the compressed graphite|NMC622-cells will be discussed and summarized in section 4.3 and 4.4, respectively.

Some of the results presented in the following section are part of a publication<sup>126</sup> and are reused with the permission of the journal. The experimental work, the evaluation, and the writing was all done by me.

### 4.1 Nonlinear compressibility of electrodes and stacks

Figure 4.1 shows the measured single layer compressibility depending on the number of layers of the different anodes and cathodes as well as the separator. The single layer compressibility is the measured compression divided by the summarized thickness of the probes (see section 3.4). The single layer compressibility at the three pressure levels of 0.08 MPa, 0.42 MPa, and 0.84 MPa for the graphite-, the C/Si-, and the Si/C-anode (calendered and uncalendered) is given over the tested number of layers in Figure 4.1a, b, and c. Of course, the single layer compressibility is increasing with the applied pressure. Furthermore, the single layer compressibility of the C/Si-anode is higher in comparison to the graphite- and Si/C-anodes. The reason for this might be the smaller particle size of  $D_{50} = 10.1 \mu\text{m}$  of the C/Si-material in comparison to the Si/C- and graphite-material with  $D_{50} = 20.1 \mu\text{m}$  and  $D_{50} = 22.5 \mu\text{m}$ , respectively. Even though, the porosities of 41.1% and 41.5% of the C/Si- and the graphite-anode are almost similar, it seems that the particle size has a significant influence on the compressibility. Regarding the compressibility of the Si/C-anode in Figure 4.1c, the uncalendered Si/C-anode shows a higher compressibility than the calendered one. This is in accordance with the reduced porosity and increased density of the calendered anode. Similar observations are made regarding the single layer compressibility of the cathodes (compare Figure 4.1d and e). The NMC622-cathode with a porosity of 27.5% exhibits a higher compressibility than the NMC811-cathode with a lower porosity of 24.4%. Hence, the compressibility of the electrodes is increasing with an increasing porosity and a decreasing particle size of the active material.

Generally, the single layer compressibility  $d_{\text{slc}}$  exhibits an exponential shape for all materials depending on the number of layers  $n_{\text{layer}}$ , which can be written as

$$d_{\text{slc}} = a - \frac{1}{e^{n_{\text{layer}} - b}}. \quad (4.1)$$

Whereas  $a$  and  $b$  can be determined by curve fitting. The variables  $a$  and  $b$  were evaluated for each material. The achieved values are provided in the supplementary material in Figure

S0.1. Figure S0.2 shows an example of the comparison of the fitted and the measured data. From the evaluation of  $a$  and  $b$  presented in Figure S0.1, it seems that  $b$  is increasing with pressure for all materials. Contrariwise,  $a$  shows a higher increase with pressure for all anode materials compared to the cathode materials. This correlates well with the observed higher compressibility of materials with a higher porosity (see Figure 4.1).

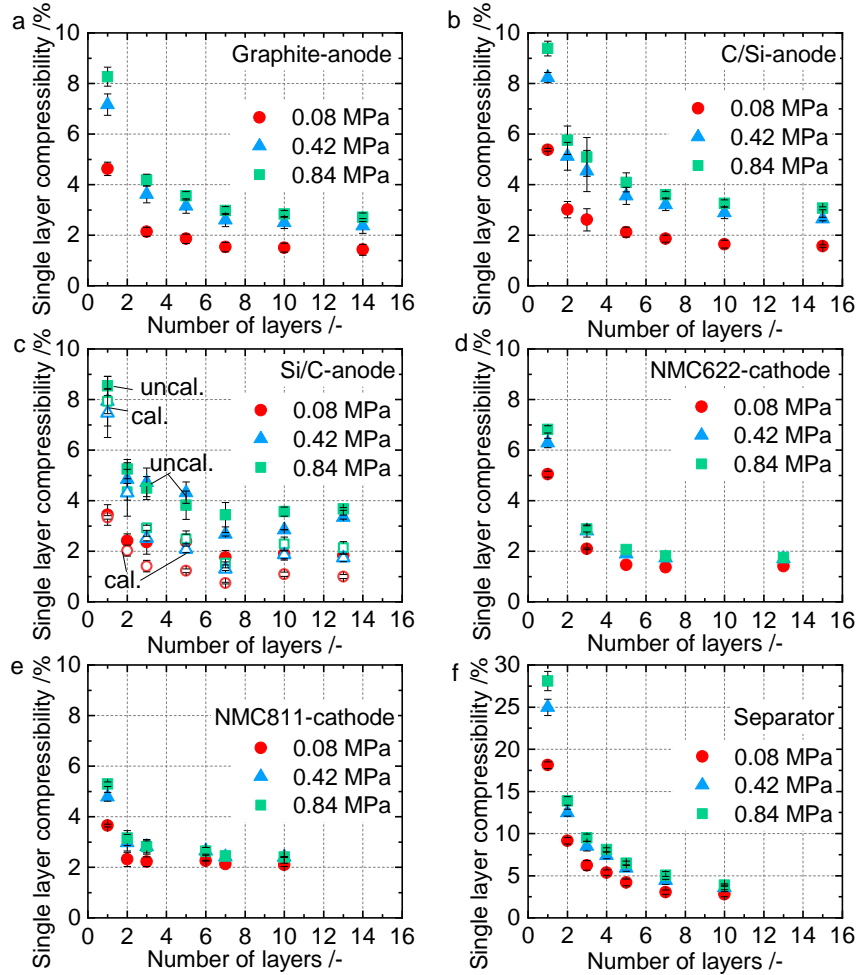


Figure 4.1: Single layer compressibility of the graphite-, the C/Si-, and the Si/C-anodes (a-c), the NMC622- and NMC811-cathodes (d, e) as well as the separator (f) over the number of layers of the probes.

Interestingly, the single layer compressibility is decreasing drastically with the number of tested layers (see Figure 4.1). Figure 4.2 illustrates this discrepancy schematically. When regarding a 2-layer system with e.g. one cathode and one anode (Figure 4.2a), the force is distributed via the contact areas of the contacting surfaces of the particles. For a system with more anode, cathode, and separator layers (Figure 4.2b), more contacting surface areas occur and the total contact area is increasing in comparison to the 2-layer system. The same force is applied on the differently sized contact areas i.e. the contact area is much smaller in case of the 2-layer system. Hence, the pressure is higher resulting in a much higher compression. With an increasing compression of the electrode, the porosity is decreasing, and the tortuosity is increasing. Therefore, the precise selection of the pressure depending on

the number of layers of a system is relevant. The effects of the decreasing porosity and the coherent increase of the tortuosity will be regarded closely in section 4.2.

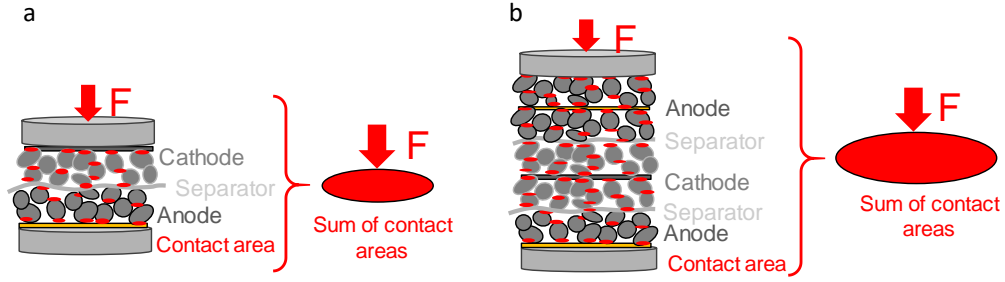


Figure 4.2: Schematic illustration of the compressibility of different number of layers. (a) Force on 2-layer electrode stack and (b) force on multi-layer electrode stack.

Figure 4.3a shows the single layer compressibility of the graphite|NMC622-stacks and the electrolyte filled graphite|NMC622-cells with 2-, 5-, and 27-layers over the applied pressure.

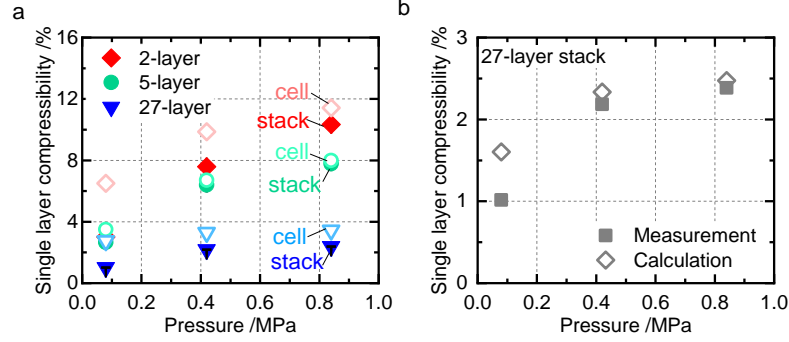


Figure 4.3: Single layer compressibility of 2-, 5-, and 27-layer stacks and electrolyte filled cells (a). Calculated single layer compressibility of 27-layer stack in comparison the measurement (b).

The same dependency of the compressibility and the number of layers as for the single electrodes is observable. E.g. at a pressure of 0.84 MPa, the thickness of the 2-layer stack is decreased by 10.3%, the 5-layer by 7.9%, and the 27-layer only by 2.4%. This means that a particular pressure has less effect in terms of the compression on a stack with a higher number of layers. As can be seen from the single electrode measurements in Figure 4.1, this effect is the highest for very small numbers and is saturating for number of layers higher than 10. Therefore, if cells are tested under compression, the number of layers in these cells should be at least 10 enabling a homogeneous pressure distribution and reproducible compression.

In addition, Figure 4.3a shows the compressibility values of the electrolyte filled cells with the exact same number of layers as in the dry stacks. These values are increased slightly in comparison to the dry stacks. The reason for this might be that the electrolyte needs to be removed from the pores of the electrode during the compression, increasing the stiffness of the stack. Similar results can be found in literature in the work of Sauerteig et al.<sup>116</sup>

With the help of these measurement results, the expected compressibility of the 27-layer stack was calculated and compared to the measurement results. Figure 4.3b shows the comparison of the measurement with the calculation. The calculations are in good agreement with the measurements for the higher loads (0.42 MPa and 0.84 MPa). However, it is important to note that the compressibility of different active materials is strongly differing in dependency of the particle size and the porosity and, therefore, is a critical value for estimations.

## 4.2 Ionic pore resistance of compressed electrodes and separators

As was shown in section 4.1, the applied pressure decreases the thickness of the porous electrodes. Therefore, the porosity of the electrodes is reduced leading to a change of the ion mobility in the pores. To quantify these effects for the utilized anode and cathode materials, symmetrical cells were assembled and the impedance spectra were measured in blocking condition (see section 2.3.2 and 3.2.1). After every measurement, the pressure on the cells was increased stepwise. Figure 4.4 gives an overview of the EIS measurements of the anodes and the cathodes conducted at different external pressure. As can be seen in the Nyquist impedance plots of an anode and cathode in Figure 4.4a and b, the spectra are shifted to higher resistances with an increased pressure.

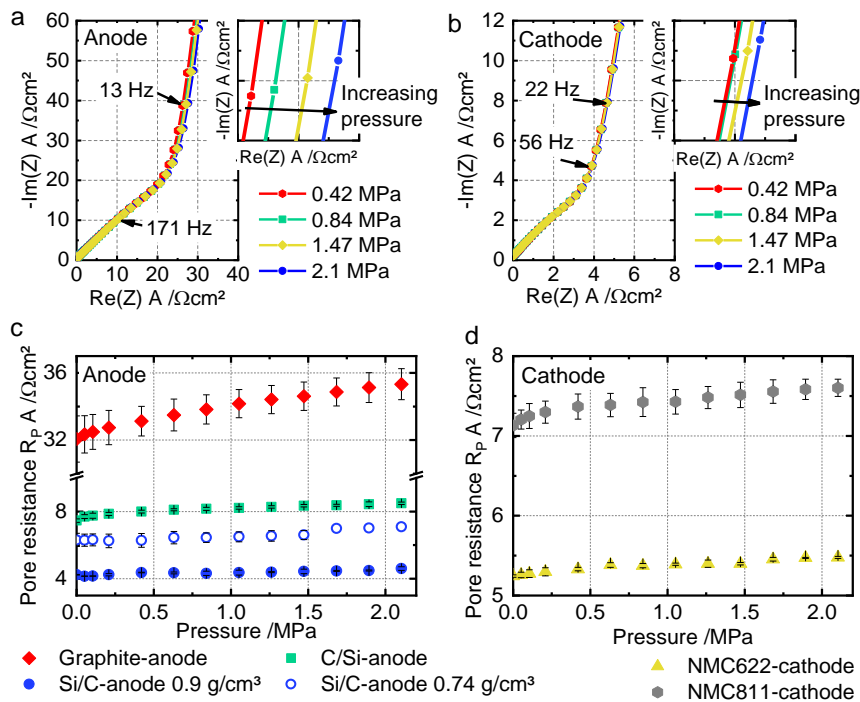


Figure 4.4: Nyquist impedance plot of the anode and cathode symmetrical cells at different applied pressure (a and b), and the extracted ionic pore resistance for all utilized anodes (c) and cathodes (d).

For a better comparability, the high frequency resistance  $R_{\text{HF}}$  is subtracted from the given impedance spectra. Figure 4.4c and d show the ionic pore resistances  $R_{p,A}$  and  $R_{p,C}$  of the different utilized anode and cathode materials. The values were derived by fitting of the



TLM function (2.6) defined in section 2.3.2. For all materials,  $R_p$  is increasing with an increasing pressure. This means that the ion mobility in the narrowed pores of the compressed electrodes is reduced. However, the materials are reacting differently on the compression. Due to the high mass loading of  $8.6 \text{ mg cm}^{-2}$  and a thickness of  $131 \text{ }\mu\text{m}$  of the graphite-anode in comparison to the mass loading of  $5.9 \text{ mg cm}^{-2}$  and a thickness of  $104 \text{ }\mu\text{m}$  of the C/Si-anode, the ionic pore resistance  $R_p$  is much higher for the graphite-anode. In addition,  $R_p$  of the graphite-anode is rising faster with the pressure. Even though, the thickness of the calendered and the uncalendered Si/C-anode with  $157 \text{ }\mu\text{m}$  and  $183 \text{ }\mu\text{m}$  is much higher than of the graphite- and the C/Si-anode, their  $R_p$  is the lowest. This is caused by the fact that the calendered and uncalendered Si/C-anodes have a low density of  $0.90 \text{ g cm}^{-3}$  and  $0.74 \text{ g cm}^{-3}$ , corresponding to high porosities of 50.4% and 53.9%, respectively. The large void space in the Si/C-anode enhances the ion mobility in the pores resulting in a decreased  $R_p$ . In case of the cathode materials, the general trend is the same,  $R_p$  is increasing with the increasing pressure. Whereas,  $R_p$  of the NMC811-cathode is around  $2 \text{ }\Omega\text{cm}^2$  higher than of the NMC622-cathode (see Figure 4.4d). This might be explainable by the higher mass loading of the NMC811-coating and the slightly higher particle size of the NMC811 active material.

Figure 4.5a presents the Nyquist impedance plots of the symmetrical separator cells (see section 3.2.1) at different applied pressure levels. The extracted ionic pore resistances  $R_{p,S}$  per layer for the measurements with 1-, 2-, and 4-layers of separator are shown in Figure 4.5b.

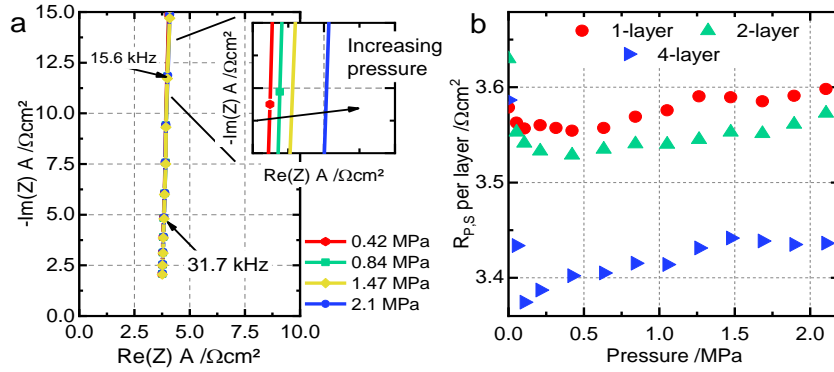


Figure 4.5: Nyquist impedance plot of the separator cells at different applied pressure (a) and extracted ionic pore resistance  $R_{p,S}$  over pressure for 1-, 2-, and 4-layer separator cells (b). Reused in parts with permission of the Journal of Power Sources.<sup>126</sup>©2019 Elsevier B.V.

$R_{p,S}$  was calculated by linear extrapolation of the impedance spectra in Figure 4.5a to the x-axis. To be able to separate the contribution of  $R_{p,S}$  from the Ohmic resistance  $R_{el,S}$  in the cell setup, the measurement was repeated with 1-, 2-, and 4-layers of separator in the symmetrical cell.  $R_{el,S}$  was calculated according to the literature<sup>106,116</sup> resulting in a value  $369.1 \text{ m}\Omega\text{cm}^2$  and is subtracted from the plotted values in Figure 4.5b. This enables to discuss  $R_{p,S}$  without any influences of the cell setup. In Figure 4.5b, it can be observed that  $R_{p,S}$  decreases to a minimum value when low pressure is applied and then increases with the pressure. This behavior is pronounced for measurements with multilayer separators, especially for the 4-layer cell. The initial decrease of the resistance can be explained by an



initial straightening and reduction of the distance between the copper foils and the separator layers. The minimum of  $R_{p,s}$  occurs at a pressure of 0.1 MPa. From there,  $R_{p,s}$  is rising almost linearly with the pressure due to an increase of the tortuosity, which is caused by the reduction of the pore volume within the separator. Furthermore,  $R_{p,s}$  per layer is differing for the 1-, 2-, and 4-layer cell measurement. The reason for this can be found in the nonlinear compressibility of the number of layers, which was shown in Figure 4.1f and is further discussed in one of my publications.<sup>126</sup> According to the work of Landesfeind et al. and Ogihara et al.,  $R_p$  is directly proportional to the tortuosity and indirectly proportional to the porosity of the electrode or the separator.<sup>102,106</sup> Therefore, by the usage of (2.8) from section 2.3.2, the tortuosity  $\tau$  can be roughly calculated. The results are in good agreement with the values from literature.<sup>116</sup> The NMC622-cathode has a tortuosity  $\tau$  of  $2.2 \pm 0.01$ ,  $\tau$  of  $15.5 \pm 0.63$  for the graphite-anode, and  $\tau$  of  $4.0 \pm 0.22$  for the separator at a pressure of 0.05 MPa. Landesfeind et al. determined  $4.1 \pm 0.2$  as tortuosity  $\tau$  of the Celgard2325 separator and values around 4 – 10 for graphite-anodes with much smaller loadings.<sup>106</sup> Sauerteig et al. determined a tortuosity  $\tau$  of  $3.0 \pm 0.1$  for a comparable NMC622-cathode.<sup>6</sup>

Figure 4.6 gives a schematic summary of the influence of the compression on the transport processes in the pores of the electrode. From the results of the EIS measurements in Figure 4.4 and Figure 4.5, it is derived that the ionic pore resistance  $R_p$  is increasing with the reduction of the pore volume by the application of a mechanical pressure. On the electrode level, this means a reduction of the accessible pore volume as schematically illustrated in Figure 4.6b. With the decreased pore volume, the ion mobility declines resulting in an increased ionic pore resistance  $R_p$ . This effect holds true for both, the anode and the cathode as well as the separator. However, as can be seen in Figure 4.4 the increase of  $R_p$  is the highest for the tested graphite-anode due to its high mass loading.

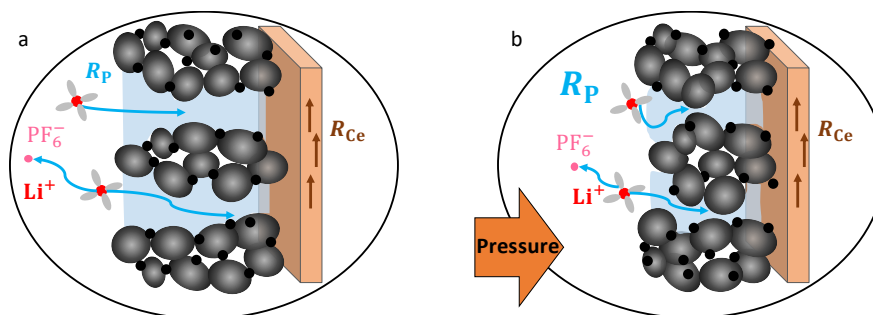


Figure 4.6: Schematic illustration of the ion mobility in the pores of an uncompressed (a) and a compressed (b) electrode.

### 4.3 Full cell impedance of compressed cells correlated to their performance

Now that the effect of the mechanical pressure on the electrode level was discussed in 4.1 and 4.2, the effect on the full cell is further analyzed. For that reason, the stacked graphite|NMC622-cells were cycled under different compression configurations (see Table 3.3 for the cell data). Characterization tests as C-rate tests and EIS measurements were conducted before and after 50 cycles. Figure 4.7 shows the Nyquist impedance plots and the

evaluated high frequency resistances  $R_{HF}$  as well as the sum of charge-transfer resistance  $R_{CT\_sum}$  of the cells after the formation and after the cycling.

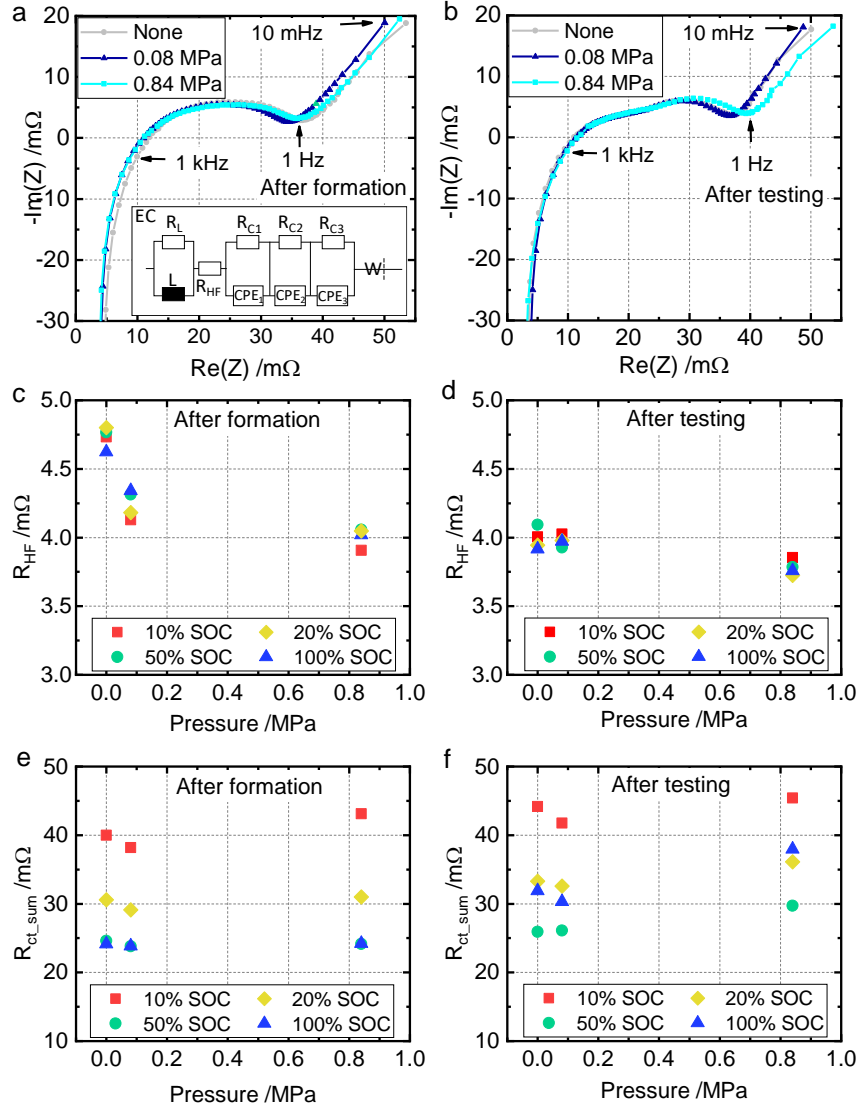


Figure 4.7: Nyquist EIS plots of the stacked graphite/NMC622 pouch cells after the formation (a) and after the cycling (b) compressed under different pressure configurations. Evaluated high frequency (c, d) and sum of charge transfer resistance (e, f) after the formation and after the cycling plotted versus the applied pressure. Reused in parts with permission of the Journal of Power Sources.<sup>126</sup>©2019 Elsevier B.V.

In addition, Figure 4.7a shows the EC utilized for the fitting (see section 2.3.1). The EIS results are provided for the cells cycled uncompressed (marked as “None” in Figure 4.7a and b) and with an applied pressure of 0.08 MPa and 0.84 MPa. To consider eventual discrepancies at a different lithiation degree of the electrodes, the EIS measurements were conducted at different SOC of 10%, 20%, 50%, and 100%. In the Nyquist impedance plots of the uncompressed cells after the formation (see Figure 4.7a), it seems that the spectrum is slightly shifted to higher resistances. This gets more obvious in the plot of the extracted  $R_{HF}$  in Figure 4.7c.  $R_{HF}$  is decreasing with increasing pressure. After the cycling (see Figure 4.7b and d)  $R_{HF}$  is generally slightly decreased and the decline of  $R_{HF}$  with the applied pressure is more flat. The decrease of  $R_{HF}$  with the increase of the applied pressure can be

explained by a shortened electric path through the full cell and a homogeneous contacting of all areas of the stack. One possible reason for the decreased  $R_{HF}$  after the cycling might be an increase in the conductivity of the electrolyte. Li et al. found a similar decrease of the high frequency resistance during the cycling and correlated it with the ongoing passivation reactions on the electrode surface, which consumes components of the electrolyte increasing the  $\text{Li}^+$  concentration.<sup>109</sup> The reduction of  $R_{HF}$  in compressed electrodes is adopted in Figure 4.8.  $R_{HF}$  is summing up different elements and processes i.e. the  $\text{e}^-$  transport  $R_{EI}$  and the  $\text{Li}^+$  transport through the separator  $R_{P,S}$ . Especially the electric transport of the electrons  $\text{e}^-$  is favored by the decreased distance and by an increased contact between the active material particles and the carbon black due to an increased packing density (illustrated in Figure 4.8b). Since this process is occurring at very high frequencies, it is mostly contributing to the measurable decrease of the high frequency resistance  $R_{HF}$ .

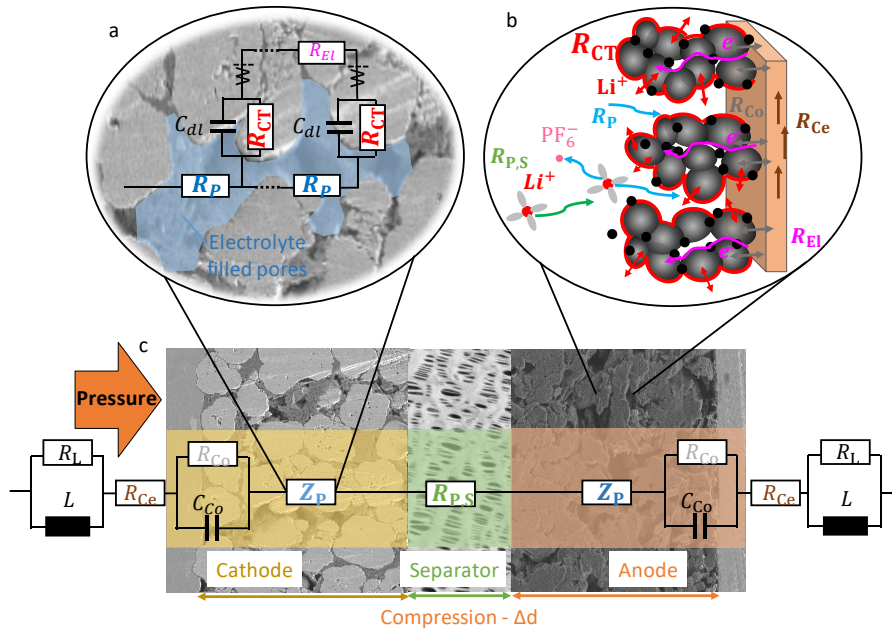


Figure 4.8: Schematic illustration of the influence of the mechanical pressure on the full electrode stack. (a) Processes in the uncompressed and (b) in the compressed stack.

In addition, Figure 4.7e and f provide the extracted sum of charge-transfer resistances  $R_{CT\_sum}$  for the differently compressed cells before and after the cycling.  $R_{CT\_sum}$  increases with a decreased SOC of the cells. In literature, this behavior is explained by a drastic change of the conductivity in layered-oxide cathode materials.<sup>132–134</sup> A marginal increase of  $R_{CT\_sum}$  with the pressure is observable. With an increased pressure on the stack, the pore volume of the electrode is compressed, and the active material particles are moved closer together minimizing the active surface of the particles. Figure 4.8 shows this decreased active surface area schematically. Decreasing the active surface area restricts the charge-transfer processes and increases the charge-transfer resistance. Other groups reported a comparable increase of the charge-transfer resistance for electrodes with a higher calendering density or higher mass loadings having a similar effect on the electrode structure.<sup>101,135</sup> As shown in section 4.2,  $R_p$  is increasing with the size of the applied pressure and is contributing to the semicircle in the EIS measurement of the full cells.

Figure 4.9 shows a summary of the cycling results of the differently compressed graphite|NMC622-cells for the cycling at a discharge rate of 1C (see Figure 4.9 a) and a C/2 (see Figure 4.9b). In addition, the results of the C-rate tests conducted before and after the cycling at 1C are plotted in Figure 4.9c and d.

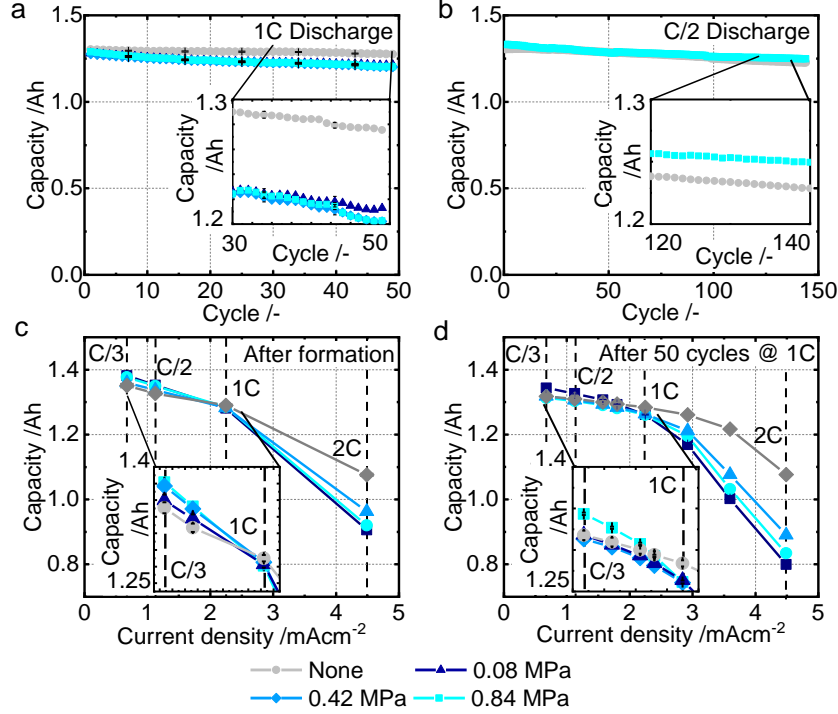


Figure 4.9: Capacity during cycling of differently compressed graphite|NMC622-cells at 1C (a) and C/2 (b) discharge rate. Capacity during C-rate test after the formation (c) and after 50 cycles at 1C discharge rate (d) of differently compressed graphite|NMC622-cells. Reused in parts with permission of the Journal of Power Sources.<sup>126</sup>©2019 Elsevier B.V.

During the cycling at a 1C discharge rate, all cells cycled under a mechanical compression (0.08 MPa, 0.42 MPa, and 0.84 MPa) exhibit a diminished capacity in comparison to the cells cycled without compression (see Figure 4.9a). The reverse behavior can be observed for the cells cycled with a discharge rate of C/2 where the cells under a mechanical compression of 0.84 MPa run more stable than without compression (see Figure 4.9b). It seems that the available capacity of the compressed cells depends strongly on the applied current rate. Therefore, the results of the C-rate tests in Figure 4.9c and d have to be evaluated. All compressed cells exhibit a higher capacity for C-rates below 0.8C. This is reversed at higher C-rates when the uncompressed cells demonstrate a higher capacity. This behavior fits perfectly with the above made assumptions regarding the influence of the pressure on the transport processes in the electrodes. Due to the reduction of the pore volume of the electrodes by the mechanical compression, the hindered ion mobility in the pores leads to polarization losses, which are rising with the applied C-rate. Hence, the improved electric contact with a decrease in  $R_{HF}$  results in lower polarization losses for low C-rates (in this case  $<0.8C$ ). Contrariwise, the polarization losses due to a diminished pore volume is dominating the available capacity of the compressed cells at higher C-rates than 0.8C. The capacity fading in Figure 4.9a cannot be assigned to irreversible aging effects but is caused

by an increased cell impedance leading to an over potential and a decrease of the available capacity. This effect is sometimes described as fatigue of the cell.<sup>136,137</sup>

Furthermore, the swelling behavior of the differently compressed graphite|NMC622-cells was investigated during the cycling. It is well known that both graphite and NMC622 exhibit only low volume expansion during the cycling, especially when compared to Si-containing anodes. However, different dilation methods were introduced in literature analyzing the lithiation process of different electrode materials with the focus on the Li intercalation in graphite during the first cycles.<sup>62,138–141</sup> Rieger et al. investigated the expansion on a multi-scale approach concluding an almost linear expansion of the graphite-anode with the lithiation of up to 3.4% and reported of the ability to detect the phase transitions in the graphite stages.<sup>142</sup> In addition, expansion measurements of LiBs have to be performed to assess their volume expansion enabling the design of the module or the pack constraint.<sup>143</sup> For that reason, Oh et al. reported of the rate dependency of the swelling of LiBs.<sup>144</sup> Furthermore, the expansion of the cells might be useful for online diagnostics on system level.<sup>145,146</sup> In addition, high precision dilation can be utilized as an input for the parametrization of a electrochemical-mechanical model of LiBs.<sup>116,147</sup> Louli et al. analyzed the expansion of pouch cells consisting of various anode and cathode materials.<sup>131,148</sup> However, most of the reported experimental setups prevent the application of a defined pressure on the electrode or the cell surface during the dilation measurement. Therefore, the expansion of the differently compressed graphite|NMC622-cells was measured in the setup developed in-house (see section 3.3) and serves as a reference for the comparison with the expansion of the Si-containing cells regarded in section 5.1 and 6.1. Figure 4.10a gives the irreversible and total swelling over the cycles. In addition, the irreversible swelling is plotted versus the relative capacity loss of the cells in Figure 4.10b.

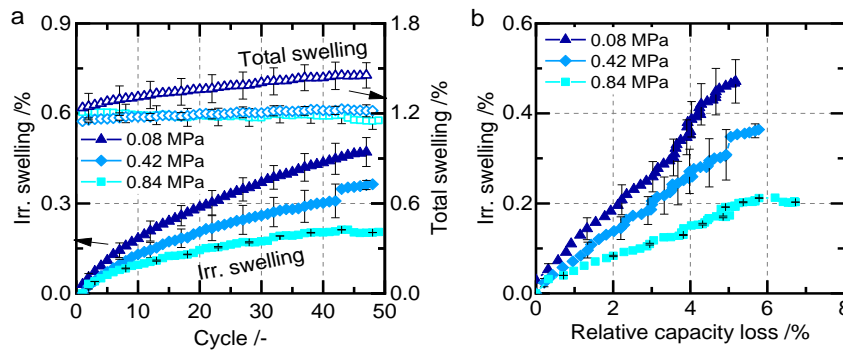


Figure 4.10: Irreversible and total swelling over cycles for differently compressed graphite|NMC622-cells (a) and irreversible swelling over the respective relative capacity loss of the cells (b).

As can be seen in Figure 4.10a, the expansion of the pouch cells is reduced by the application of a high mechanical pressure. Cells cycled with a mechanical pressure of 0.84 MPa exhibit the lowest values for the irreversible and the total swelling of 0.2% and 1.15%, respectively. While cells compressed with 0.08 MPa show an irreversible and total swelling of 0.47% and 1.45%. The relative capacity loss of the 0.84 MPa compressed cells of 6.7% is slightly higher than of the cells under lower compressions. The degree of lithiation into the anode during the charging of the cells is lower in the 0.84 MPa compressed cells due to

a higher impedance (see Figure 4.7), which leads to a smaller expansion. Furthermore, it can be possible, that the higher compression strength forces the material to expand more into the pores of the electrode than in vertical direction. Due to the fact that the irreversible swelling and the relative capacity loss show a good linearity (see Figure 4.10b), it can also be derived that the cell aging is mostly dominated by a ICL due to film formation reactions.<sup>131</sup>

## 4.4 Summary of the influence of mechanical pressure

Figure 4.11 sketches the effect of the mechanical pressure on the transport processes in a porous electrode.

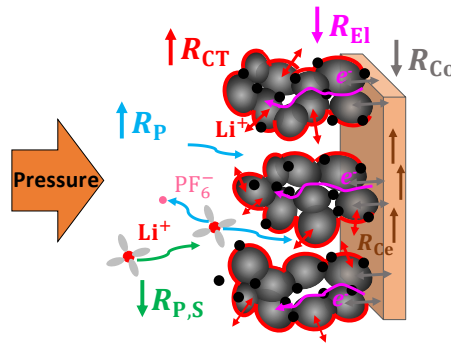


Figure 4.11: Schematic summary of the influence of mechanical pressure on the transport processes in a porous electrode.

Firstly, the reduction of the pore volume fraction, which was assessed by compressibility measurements in section 4.1, leads to an impaired ion mobility in the pores resulting in an increased ionic pore resistance  $R_P$  (see 4.2 for further discussion). In addition, the charge-transfer processes at the active particle surface are hindered due to a decreased surface area resulting in an increasing  $R_{CT}$ . As was measured in section 4.3, the high frequency resistance is reduced by the mechanical compression. The reason for this is a shortened electric path through the stack and an improved and more homogeneous contact decreasing  $R_{P,S}$ ,  $R_{EL}$ , and  $R_{CO}$ . Therefore, the compressed graphite|NMC622-cells showed an improved performance at low C-rates. Whereas higher polarization lead to a lower available capacity at increased C-rates. Expansion measurements of the cells revealed the highest irreversible swelling of 0.47% and the highest total swelling of 1.45% after 50 cycles.

Furthermore, the conducted compressibility measurements uncovered a nonlinear dependency of the number of electrode layers with the resulting compressibility (see section 4.1). The compressibility of an electrode stack with a small number of layers is much higher than for a stack with a large number of layers when compressed with the same pressure.

Hence, the operation conditions of the cell, as the applied pressure and the cycling rates, have to be defined well in dependency of the composition of the cell stack and the selected electrode materials.



## 5 Influence on the aging of C/Si|NMC811-cells with a high expansion

Based on the knowledge of the effects of mechanical pressure on the reference system graphite|NMC622 gained in section 4, the aging behavior of a Si-containing anode under mechanical pressure will be investigated in the following section. Firstly, the cycling results obtained with stacked C/Si|NMC811-cells (see Table 3.3 for further information) at different pressure conditions conducting operando expansion as well as pressure mapping measurements will be discussed in section 5.1. Secondly, a closer look will be taken on the aging mechanisms of cells under heavily fixed and flexible compression in section 5.2 employing post-mortem analyzes. Finally, uncompressed cycled cells will be assessed closely in section 4.3 before the summary in section 5.4.

Some of the results presented in the following section are published<sup>128</sup> and are reused with the permission of the journal. The experimental work, the evaluation, and the writing was done by me, except the analysis of the 18650 cells, which is not utilized in this work.

### 5.1 Cyclic aging and volume expansion in dependency of the applied pressure

Figure 5.1 gives an overview of the cycling results of cells cycled under flexible and fixed compression at pressure levels of 0.08 MPa, 0.42 MPa, and 0.84 MPa as well as without compression. Figure 5.1a depicts the discharge capacity and the Coulombic efficiency and Figure 5.1b shows the total and the irreversible swelling. Figure 5.1c and d provide the discharge capacity and the total swelling of the differently compressed cells after 100 cycles. Of course, the swelling cannot be measured for the cells under fixed compression. As can be seen in Figure 5.1a, the cells cycled under compression show a significantly increased initial discharge capacity of around 10% with an average of  $161.1 \text{ mAh (g}_{\text{AM}})^{-1}$  compared to the cells without compression with an average value of  $147.2 \text{ mAh (g}_{\text{AM}})^{-1}$ . Due to the absence of a mechanical compression on the uncompressed cells, the lower available capacity might be attributed to a missing connection of some active zones and layer detachments. Similar observations were made in literature employing X-ray CT to evaluate layer detachments in LiBs with Si-containing anodes.<sup>53</sup> The repetitive volume expansion and contraction of the C/Si-anode is accelerating these effects increasing the cell impedance. Therefore, the capacity throughput is decreased compared to the cells cycled under a mechanical compression. A similarly improved performance of Si-containing cells under mechanical pressure was reported by Berckmans and De Sutter et al.<sup>51,52</sup> In addition, a lower swelling can be observed for the uncompressed cells compared to the cells cycled under a flexible pressure of 0.08 MPa and 0.42 MPa (see Figure 5.1b). This is explainable by the decreased capacity throughput in the uncompressed cells. Due to a smaller degree of lithiation in the C/Si-anode, the expansion is reduced. Furthermore, it becomes obvious from Figure 5.1a that the uncompressed cells experience an abrupt change of the aging rate

at around the 70<sup>th</sup> cycle. The discharge capacity drops drastically while the Coulombic efficiency exhibits a minimum at around cycle 83 before it increases again. The same turning point can be observed regarding the graphs of the irreversible and the total swelling in Figure 5.1b. The cells cycled at a low flexible pressure of 0.08 MPa show the same characteristics. This effect can most likely be contributed to an occurring contact loss in the C/Si-anode, which was e.g. assessed by Wetjen et al. and Yoon et al. for C/Si-anodes with comparable properties on coin cell level.<sup>79,80,149</sup> This is enhanced by the absence of a strong enough mechanical pressure that is necessary to maintain the particle-particle contact in the anode when it is shrinking during the delithiation. Yu et al. draw similar conclusions during their dilatometry study of graphite-Si-anodes.<sup>150</sup> They found that the electrode is not brought back in its origin structure without a compressive driving force leading to electrical separation of the active material particles. These results will be further discussed in the section 5.3.

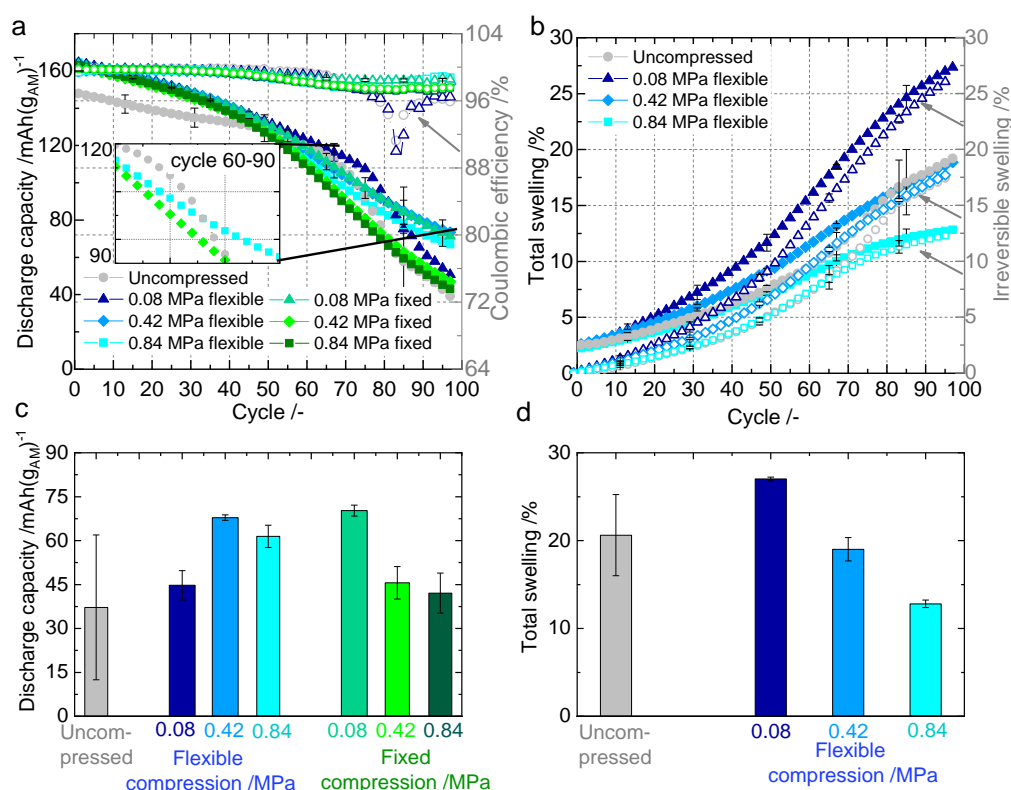


Figure 5.1: Discharge capacity and Coulombic efficiency (a) and total and irreversible swelling (b) over cycling for cells under different compression. Comparison of the discharge capacity (c) and the total swelling (d) after 100 cycles. Reused in parts with permission of the Journal of The Electrochemical Society.<sup>128</sup> ©2019 ECS.

As can be seen from Figure 5.1c, the cells cycled at 0.42 MPa flexible pressure together with the cells cycled at 0.08 MPa fixed pressure show the highest remaining capacity that is 1.7 – 2 times higher than the remaining capacity of the cells cycled uncompressed and low flexibly compressed (0.08 MPa). With an increasing flexible pressure of 0.84 MPa, the remaining capacity is decreasing. In addition, a much lower total swelling of only 13% of the initial stack thickness is observable. Therefore, it seems as if the increasing pressure hinders the cell's expansion. One reason for this decreased vertical expansion might be that



the Si-particles are forced to expand into the pores of the anode. As mentioned in section 4, a decreased porosity can lead to a reduction of the available capacity by a hindered ion mobility in the pores, which can explain the smaller capacity of the cells under a heavily flexible compression of 0.84 MPa. Furthermore, it seems that an increasing fixed pressure (above 0.08 MPa) has a negative impact on the lifetime of the cells. The cells cycled at 0.42 MPa and 0.84 MPa fixed compression exhibit a remaining capacity of only 45.6 mAh (g<sub>AM</sub>)<sup>-1</sup> and 42.1 mAh (g<sub>AM</sub>)<sup>-1</sup>, which means a capacity fading of 71.7% and 73.8%, respectively. Hence, a high fixed compression reduces the lifetime of the cells drastically.

Summarizing, the 0.42 MPa flexible and the 0.08 MPa fixed compression seem to be beneficial for the cycling performance of the C/Si|NMC811-cells. However, the question remains why the application of a higher pressure impairs the performance of the cells. Hence, the aging mechanisms of the cells cycled under 0.84 MPa flexible and 0.42 MPa fixed compression will be investigated in more details in section 5.2. In addition, the reasons for the failure of the uncompressed cells will be evaluated in section 5.3.

## 5.2 Aging mechanisms of cells under a heavily fixed and flexible compression

Initially, the pressure distribution of the cells cycled under 0.42 MPa fixed and 0.84 MPa flexible compression is evaluated with the pressure mapping system introduced in 3.3. Figure 5.2 provides an overview of the pressure mapping results of the cells. Figure 5.2a and d show the pressure distribution on the cells' surfaces after the formation, Figure 5.2b and e after 50 and Figure 5.2c and f after 100 cycles. To evaluate the pressure gradients, the pressure is plotted for one line across the cells' surfaces in x- and y-axis for each measurement. The lines were placed on the areas with the highest detected pressure. The average pressure measured with the externally attached load cell is added to every pressure map. The pressure maps were measured operando during the cycling of the cells, whereas the snapshots show the pressure distribution in the fully charged state after CC/CV charging. As can be seen in Figure 5.2a and d, the pressure distribution on both cell surfaces was homogeneous at the start of the measurement. Although, the average pressure on the surface of the cell under fixed compression increased to 0.66 MPa from its initial value of 0.42 MPa already after the formation. After 50 cycles, the average pressure of 0.85 MPa reached twice the initially applied value and exceeded the pressure of the cell cycled under 0.84 MPa flexible compression, which stayed under a constant pressure during the complete procedure. Regarding the pressure distribution, extreme differences of the cells cycled under 0.42 MPa fixed and 0.84 MPa flexible pressure can be observed (compare Figure 5.2b and e). On the surface of the cell cycled under 0.42 MPa fixed compression, pressure hot spots in the regions close to the current collectors occurred after 50 cycles. Thereby, a maximum value of 5.21 MPa is reached whereas the cell under 0.84 MPa flexible compression exhibits only a maximum value of 2.95 MPa. These areas of extreme pressure mostly occur close to the anode terminal. This is explainable, since the C/Si-anodes experience much higher volume changes in comparison to the NMC811-cathodes. After 100 cycles, the red zones with the highest pressure level moved to the middle of the cell's surface (see

Figure 5.2c). The average pressure of the fixed compression increased further to 1.01 MPa, which means a pressure increase of 140% based on the initially applied pressure of 0.42 MPa. It seems as if the high utilization of the regions close to the current collectors was relocated to beforehand less exploited regions. Contrariwise, the pressure distribution on the cell cycled under 0.84 MPa flexible compression seems to be slightly more uniform after 100 cycles than after 50 cycles. This correlates with the steady capacity fading observed in Figure 5.1 and the decreased difference of the total and the irreversible swelling resulting in a diminished reversible breathing of the cells. Less  $\text{Li}^+$  is cycled between the anode and the cathode reducing the reversible swelling, which results in a less pronounced and a more uniform pressure distribution on the cell surface.

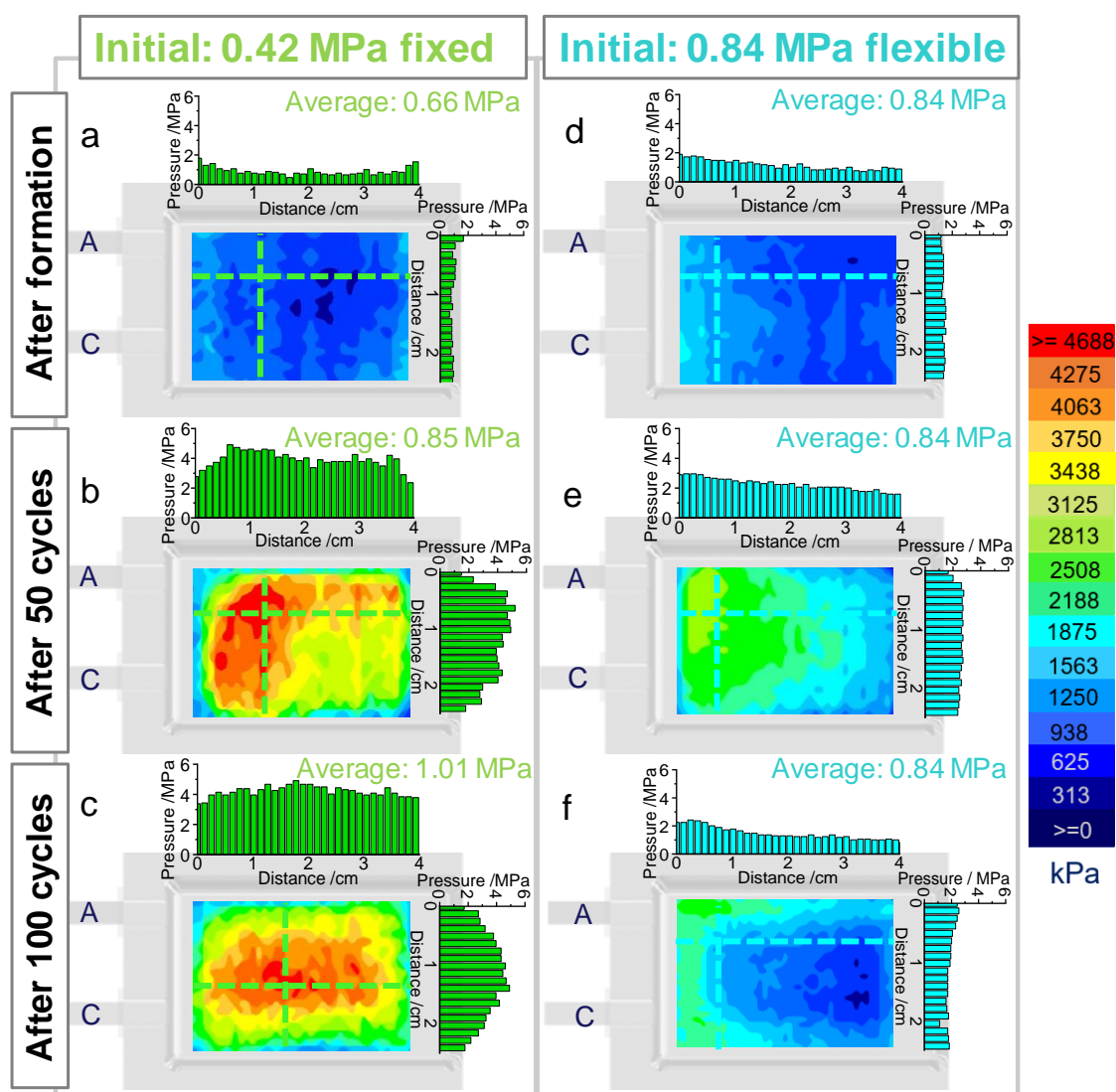


Figure 5.2: Pressure distribution on the surfaces of a cell under 0.42 MPa fixed (a-c) and 0.84 MPa flexible compression (d-f) after the formation, after 50 cycles, and after 100 cycles. Reused in parts with permission of the Journal of The Electrochemical Society.<sup>128</sup> ©2019 ECS.

Interestingly, the presented results of the cell cycled under 0.42 MPa fixed compression correspond well with thermal characterizations and modelling of LiBs in literature. All conducted studies showed a higher current distribution in the regions close to the current

collectors, which occurred due to the cell geometry and the composition of the current collectors.<sup>151–153</sup> Resulting higher current densities are leading to locally increased temperatures on the cell surface, which are mostly located close to the current collectors.<sup>153</sup> Furthermore, Veth et al. found that the occurrence of these inhomogeneous temperature gradients can indicate local aging effects resulting in electrically inactive areas.<sup>151</sup> According to the herein shown findings, it can be concluded that the increased current density close to the current collectors leads to a drastic increase of the pressure across the surface of the cells compressed at a fixed compression. For the herein tested C/Si|NMC811-cells, maximum pressure hot spots of up to 12 times the initially applied pressure emerge on the surface. These observed pressure inhomogeneities are most likely one reason for the accelerated cyclic aging of the cells under heavily fixed compression seen in Figure 5.1.

For a further understanding of the aging mechanisms, an extensive post-mortem analysis was conducted. Initially, the aging of the anodes is regarded by SEM-cross sectioning, by EIS measurements of the aged anodes, and by mercury porosimeter as well as coin cell measurements of both, the aged anodes and the aged cathodes. Finally, the aged separators are analyzed employing SEM and EIS techniques. Figure 5.3 shows the SEM cross-sections of the aged C/Si-anodes harvested from the cells cycled without compression (Figure 5.3a), under 0.84 MPa flexible compression (Figure 5.3b), and under 0.42 MPa fixed compression (Figure 5.3c). In addition, Figure 5.4 shows the Nyquist impedance plot of the symmetrical cell measurements of the harvested anodes from cells cycled under 0.42 MPa fixed compression and under 0.84 MPa flexible compression. Figure 5.5 depicts the results of the mercury porosimeter measurements conducted post-mortem of both, the anodes and the cathodes, respectively. Since the harvested anodes from the cells cycled without compression exhibited some Li deposition and a diminished adhesion, it was not possible to harvest enough areas of the anode to assemble symmetrical pouch cells nor to perform porosimeter measurements.

As can be seen in Figure 5.3, the aged anodes differentiate strongly depending on the respective compression condition. The anode cycled uncompressed shows the highest irreversible swelling of around 84.1% compared to the initial thickness. Additionally, the Si/C-particles show a strong increase in the size, especially when comparing to the anode cycled in a cell under 0.42 MPa fixed compression (compare Figure 5.3a and c). Furthermore, the particle boundaries are clearly visible and free space can be observed between most of the particles leading to the assumption of an ongoing particle-particle contact loss. The anode harvested from a cell cycled under 0.84 MPa flexible pressure shows a smaller swelling of 61.9% (see Figure 5.3b). The particle structure of the anode seems to be completely pulverized and passivated with electrolyte decomposition products frequently reported in literature.<sup>149,154</sup> EDX measurements confirmed the presence of F, P, and O in the regions of passivation. In addition, almost no remaining porosity is observable. Contrariwise, the anode harvested from a cell cycled under 0.42 MPa fixed compression appears in a different manner (Figure 5.3c). The anode expanded only by 29.1 % of its initial thickness. The particles can be recognized in their initial structure without being completely pulverized. A much lower passivation with electrolyte decomposition products is visible and a higher remaining porosity is recognizable. All these observations are confirmed by both, the EIS

measurements of the harvested anode symmetrical cells in Figure 5.4 and by the mercury porosimeter measurements in Figure 5.5. The ionic pore resistance  $R_p$  of the anode harvested from a cell cycled under 0.84 MPa flexible compression of  $21.6 \Omega \text{ cm}^2$  is much higher than of the anode harvested from a cell cycled under 0.42 MPa fixed compression of  $14.3 \Omega \text{ cm}^2$ . The values differentiate by the factor of 1.5. This is a result of the much more narrowed space in the pores of the anode harvested from the cell cycled under 0.84 MPa flexible compression. The mercury porosimeter measurements confirm the strongly reduced porosity of 30.4% compared to the initial value of 41.1% (see Figure 5.5a). Furthermore, the main peak of the pore size distribution at a radius of around  $0.75 \mu\text{m}$  shifted to lower pore radii of around  $0.18 \mu\text{m}$ . This indicates the reduced pore space caused by the strong film formation in the pores. Contrariwise, the anode harvested from the cell cycled under 0.42 MPa fixed compression shows a remaining capacity of 36.5% and only a slight reduced main peak of the pore distribution at a radius of around  $0.7 \mu\text{m}$ .

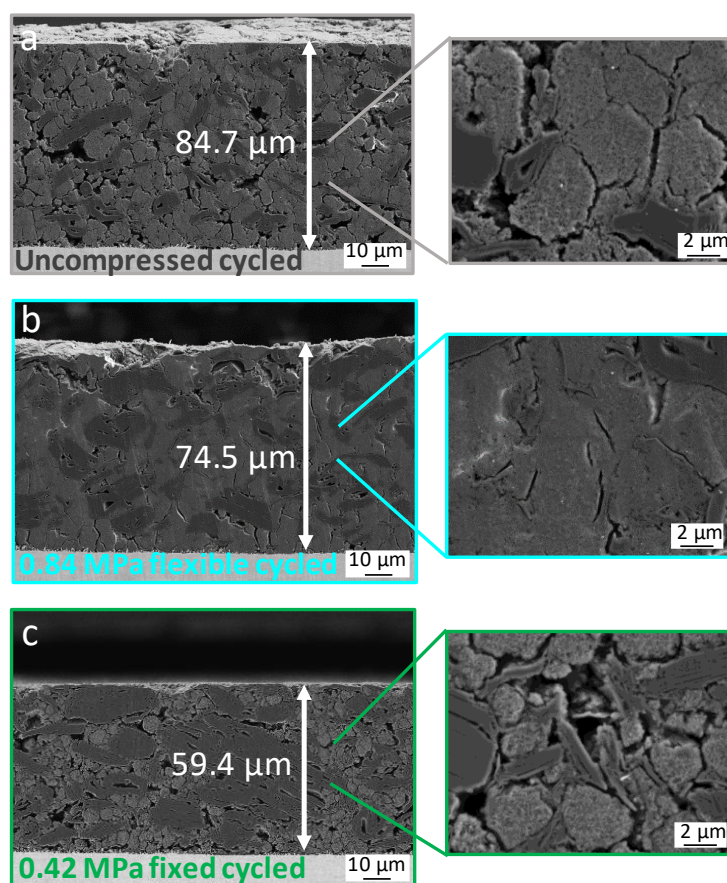


Figure 5.3: SEM cross-sections of the C/Si-anodes harvested from cells cycled without pressure (a), under 0.84 MPa flexible compression (b), and 0.42 MPa fixed compression (c) after 100 cycles. Reused in parts with permission of the Journal of The Electrochemical Society.<sup>128</sup> ©2019 ECS.

Figure 5.4 reveals that  $R_p$  of the anode harvest from the cell cycled under 0.42 MPa fixed compression is only slightly higher than  $R_p$  of the pristine anode. This is in good agreement with the SEM cross-section and the porosimeter measurements shown in Figure 5.5. Furthermore, the slope of the Nyquist impedance plot of the aged anodes is different in comparison to the pristine anode. This might be explainable by a changed pore structure and

hence, a differing electrode structure of the aged anodes in comparison to the pristine one. As was already derived by Keiser et al. in 1976 and adapted by some other groups, the low frequency behavior of the Nyquist impedance plot of porous electrodes is strongly influenced by the pore shape.<sup>122,155–158</sup> Song et al. found a correlation between the penetration depth in the porous electrodes and the slope of the EIS spectra.<sup>159,160</sup> Malifarge et al. ascribes the deviation of the low frequency angle in the Nyquist impedance plot to electrode properties i.e. the roughness of the surface of the particles and the stacking of the particles in the electrodes.<sup>161</sup>

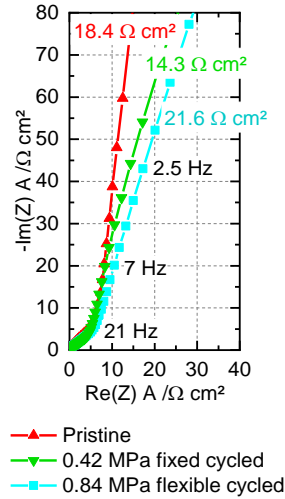


Figure 5.4: Nyquist impedance plots of the symmetrical cell measurement of the anodes harvested from cells cycled under different compressions in comparison to the pristine anode.

Figure 5.5a shows the pore size distribution of the aged cathodes in comparison to a pristine one.

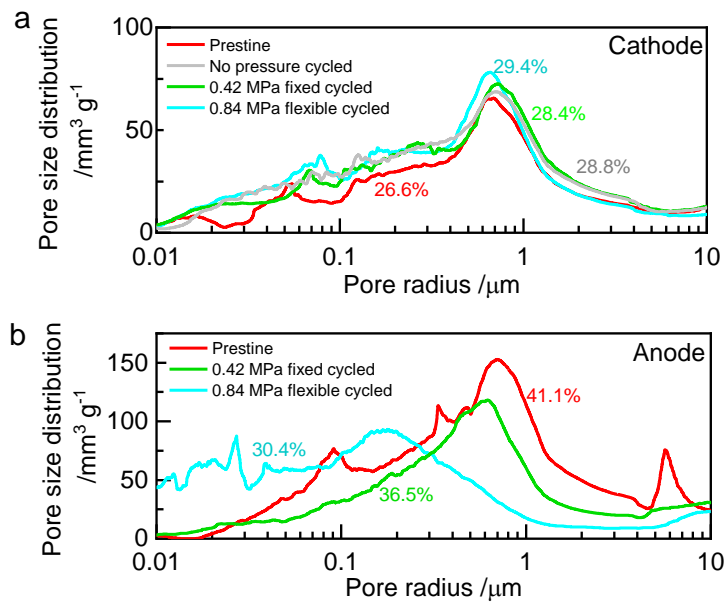


Figure 5.5: Mercury porosimeter measurement results for the harvested cathodes (a) and anodes (b). The resulting porosity of each electrode is presented in the graphs.



The resulting porosity of each electrode is presented as written value in the graphs. As can be expected, the porosity as well as the pore size distribution did not change significantly.

For a further determination of the aging effects of the differently compressed cells, the aged anodes and cathodes were tested post-mortem in re-assembled coin cells (see 3.2.5 for further information). Figure 5.6a shows the discharge capacity of the anodes harvested from cells cycled without, with 0.42 MPa fixed, and with 0.84 MPa flexible pressure at different current densities. The remaining capacities of the harvested cathodes are shown in Figure 5.6b. Thereby, the NMC loss and the ICL are determined as described in section 3.2.5 and are presented as ratio based on the initial capacity of the cells during the formation in percentage.

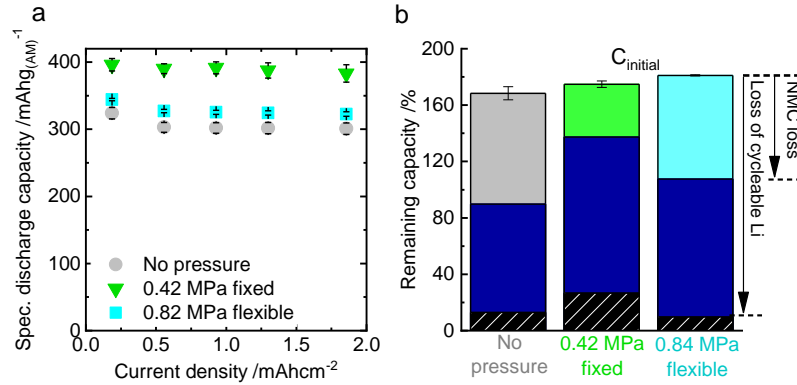


Figure 5.6: Specific discharge capacity of the harvested anodes (a) and determined remaining capacity of the harvested cathodes (b) in comparison to their initial capacity after cycling at different pressure conditions. The balcony diagram shows the NMC losses and the ICL determined in accordance with the explanation in section 3.2.5 divided by the initial capacity of the cells during the formation in percentage.

The discharge capacity of the anode harvested from a cell cycled under 0.42 MPa fixed pressure demonstrates the best performance with a remaining capacity of  $400 \text{ mAh}(\text{g}_{\text{AM}})^{-1}$  closest to the initial capacity of the pristine C/Si-anodes of  $576 \text{ mAh}(\text{g}_{\text{AM}})^{-1}$ . Both, the anodes harvested from the cells cycled uncompressed and 0.84 MPa flexibly compressed, show a drastically reduced capacity of  $302 \text{ mAh}(\text{g}_{\text{AM}})^{-1}$  and  $327 \text{ mAh}(\text{g}_{\text{AM}})^{-1}$  at a current density of  $0.55 \text{ mAh cm}^{-2}$ , respectively. It seems that the anode harvested from the cells cycled under 0.42 MPa fixed compression shows a less distinct aging agreeing well with the optical impressions from the SEM cross-sections in Figure 5.3c. Regarding the cathode losses, the cathodes harvested from the cells cycled under fixed compression show the lowest NMC and cycleable Li loss (see Figure 5.6b). However, the losses of all harvested cathodes are not negligible, which will be discussed in section 6.2.

The mass and the thickness of the cycled anodes and cathodes were determined post-mortem. Figure 5.7 shows the evaluated changes of the thickness and the masses of the anodes and the cathodes. As expected based on the previous results, the anodes harvested from the cells cycled under 0.42 MPa fixed compression show the lowest increase of their thickness and mass. The masses of the anodes cycled under flexible compression and without pressure are very similar. However, the thickness of the anodes harvested from the cells cycled

under 0.84 MPa flexible compression is much reduced. This indicates a much reduced porosity of this anodes and agrees well with the porosity results shown in Figure 5.5. A reduction of the cathode mass can be observed for all cycling conditions. The mass loss of the cathodes agrees well with the ICL confirmed by post-mortem conducted coin cell measurements shown in Figure 5.6b, proving that the Li from the cathode is irreversible bond in the anode. In addition, the thickness of the cathodes decreased in case of the cycling under 0.84 MPa flexible and 0.42 MPa fixed compression. However, the reduction of the thickness is especially pronounced for the cathodes harvested from the cells cycled under 0.42 MPa fixed compression. Due to the high pressure in the cells induced by the prevention of the cell expansion, the anode swelling compresses the cathode irreversibly.

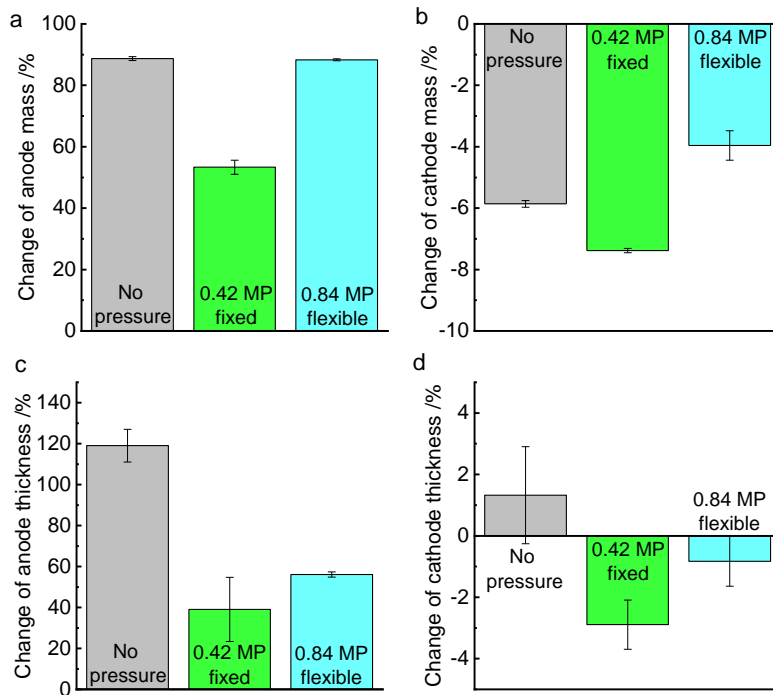


Figure 5.7: Change of the mass (a and b) and the thickness (c and d) of the harvested anodes and cathodes of the cells cycled without pressure, at 0.42 MPa fixed, and 0.84 MPa flexible pressure calculated based on the properties of the pristine electrodes.

Since both, the aged anode and the aged cathodes from the cells cycled under 0.42 MPa fixed compression showed the best performance, the high capacity fading of these cells is still not explainable. Therefore, further analyses of the aged separators from the differently compressed cells were conducted and the aged separators were analyzed employing EIS measurements. Figure 5.8 shows the SEM top views of the pristine separator as well as the aged separators harvested from the cells cycled under different pressure conditions. The separator surfaces of both, the cells cycled without and under flexible compression, exhibit no drastic modifications in comparison to the pristine separator (compare Figure 5.8b and d). However, an increased thickness to 30  $\mu\text{m}$  of the initial 25  $\mu\text{m}$  and visible deposition products can be found for the separator harvested from the cells cycled uncompressed. During the cell opening, the separators of the cells cycled uncompressed always appeared in a

yellow color leading to the assumption of the deposition of electrolyte decomposition products. To confirm this, EDX analysis was employed confirming the presence of a higher amount of F on the separator. The separator from the cell cycled under 0.42 MPa fixed compression exhibits remarkable differences compared to the others (see Figure 5.8c). Firstly, the thickness of the harvested separator shows an average value of 20  $\mu\text{m}$ , which is 5  $\mu\text{m}$  thinner than the pristine separator. Secondly, it appears as if there are several larger zones of strong irreversible compression on the surface of the separator. The pore structure seems to be damaged and it looks as if particles from the anode or the cathode were irreversible pressed into the soft separator. This leads to particle imprints and pore closure, which might be caused by plastic flow due to the immense pressure. This is in good agreement with the pressure mapping results in Figure 5.2 confirming the occurrence of extreme pressure hot spots.

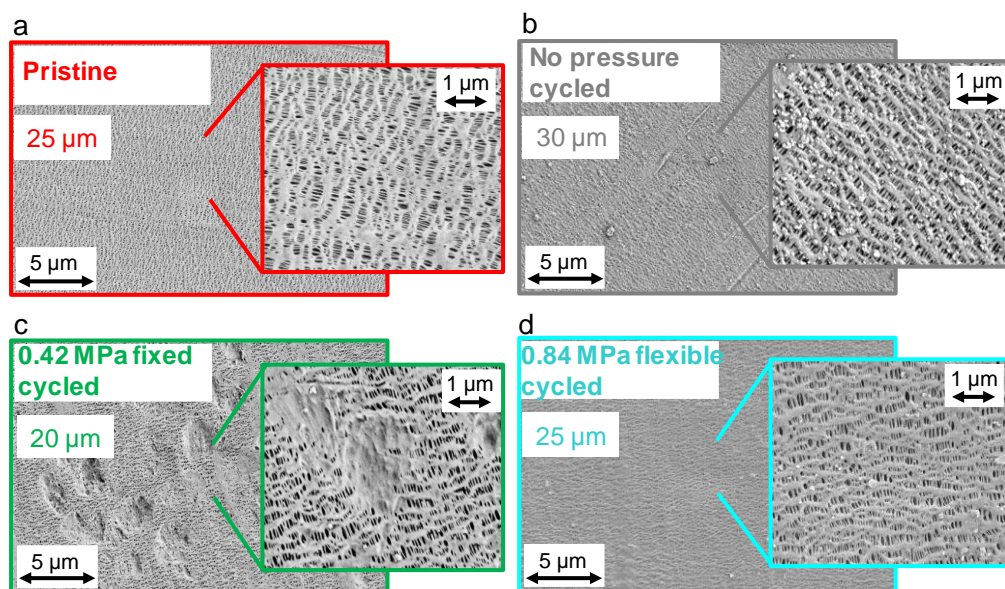


Figure 5.8: SEM images of the pristine (a) and the cycled separator from an uncompressed cycled cell (b) and under 0.84 MPa flexible (c) and 0.42 MPa fixed (d) compression cycled cells. Reused in parts with permission of the Journal of The Electrochemical Society.<sup>128</sup> ©2019 ECS.

Since the SEM analysis considers only small areas of the separator, EIS measurements were conducted to confirm the visual appearance of the permeability of the different separators. As can be seen in Figure 5.9, the results from the SEM analysis are confirmed showing the highest ionic pore resistance  $R_{P,S}$  for the separator harvested from the cell cycled under 0.42 MPa fixed compression.  $R_{P,S}$  is divided by the thickness of the respective separator to enable the comparison.  $R_{P,S}$  is increased by 37.8% in comparison to the pristine separator. This fact together with the visual appearance of the separator can lead to the assumption that the capacity fading of the cells under a highly fixed compression is issued by local pore closure and a strongly decreased  $\text{Li}^+$  mobility in the compressed separator. Other groups made similar derivations. Peabody and Arnold investigated a comparable polymer separator (Celgard2340) and found mechanically induced viscoelastic creep leading to pore closure and a reduced  $\text{Li}^+$  transport.<sup>162</sup> Cannarella and Arnold pointed out that the occurrence



of an external or an internal stress, e.g. initiated by electrode expansion, can lead to localized pore closure causing an inhomogeneous current distribution and a non-uniform electrode utilization.<sup>163</sup> The group of Wood simulated the deformation of PE and PP separators under local compressive stresses.<sup>164,165</sup> As input for the simulation, the real microstructures of the separators were utilized gained by FIB-SEM tomography. The results showed a strongly decreasing  $\text{Li}^+$  permeability, an increasing tortuosity, and a thereby, induced voltage drop due to an increased impedance. They introduced a scheme describing the impermeability and the collapse of the connecting network in the PE separator when local stress is applied e.g. by the imprint of particles.<sup>164,165</sup> Since the herein utilized separator (Celgard 2325) is consisting of a three-layered structure of PP/PE/PP,<sup>58</sup> the deformation of the PE layer can cause a drastically decrease of the  $\text{Li}^+$  mobility leading to an accelerated capacity fading.<sup>164–166</sup> The circumstances that the separator is blocking the  $\text{Li}^+$  diffusion and is leading to a strongly decreased permeability could also explain the almost unutilized and less passivated appearance of the anode harvested from the cell cycled under 0.42 MPa fixed compression (see the SEM cross-section in Figure 5.3c).

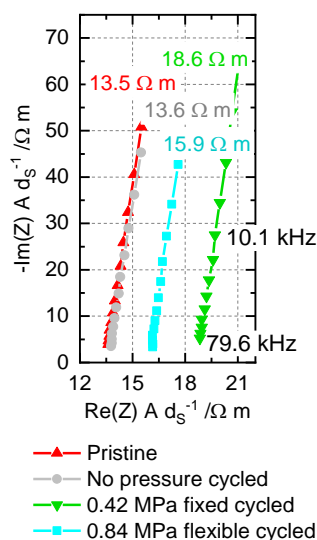


Figure 5.9: Nyquist impedance plots of the symmetrical cell measurement of the separators harvested from cells cycled under different compression in comparison to the pristine separator. Reused in parts with permission of the Journal of The Electrochemical Society.<sup>128</sup> ©2019 ECS.

Figure 5.10 sketches the main findings of the effect of a heavily flexible or a heavily fixed pressure on the aging of the cells with C/Si-anodes with a high vertical expansion. Figure 5.10a shows the electrode stack in the starting condition before the start of the cycling. The separator is shown as a conductive network of paths through the polymer, which Wood et al. utilized as a model of a PP separator.<sup>165</sup> The simplification of the herein utilized PE/PP/PE separator to a PP network is made for a better clarity of the ongoing mechanisms. As can be seen in Figure 5.10b, the thickness of the electrode stack is kept constant in the heavily fixed compression. Since the Si in the C/Si-anode is expanding anyway, the thickness of the anode is increasing around 29.1% (see SEM cross-sections in Figure 5.3c). Hence, the cathode and the separator are forced to shrink. The thereby induced mechanical stress on the separator network leads to pore closure and a reduction of the  $\text{Li}^+$  mobility

through the pores. This results in an increase of the impedance and of the voltage drop across the separator. Ultimately, the capacity of the cells under heavily fixed compression is reduced because the voltage limits are reached earlier.

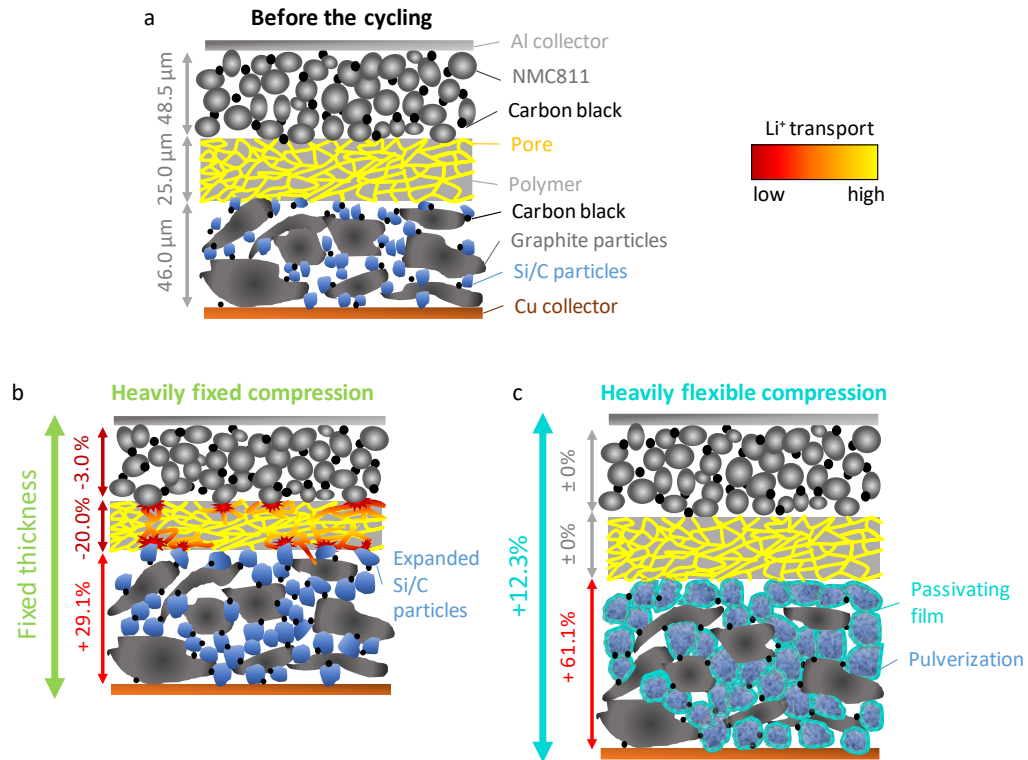


Figure 5.10: Schematic illustration of the aging mechanisms in compressed Li-ion cells with C/Si-anodes. (a) Before cycling, (b) after cycling under heavily fixed compression, and (c) after cycling under heavily flexible compression.

As was seen in Figure 5.3c, the anode seemed to be less utilized in comparison to the other two harvested anodes. This can be explained by the diminished  $\text{Li}^+$  transport in the separator reducing the utilization of the anode. In contrast, the aging of the cells under a heavily flexible compression is dominated by the ongoing formation of a passivating film on the anode due to the repetitive and unhindered expansion. As is illustrated in Figure 5.10c, the volume of the Si is increasing significantly. This was confirmed by the conducted operando expansion measurements revealing a total swelling of 12.3% of the cells under 0.84 MPa flexible compression after 100 cycles (see Figure 5.1). The post-mortem investigation of the harvested anode uncovered an increase of up to 61.1% of its initial thickness. This immense expansion destroys the SEI formed in the previous lithiation cycle and induces further electrolyte decomposition at the newly exposed particle surfaces. The result is the deposition of insulating films<sup>36,46</sup> and the trapping of cycleable Li, e.g. by the formation of Li silicates as  $\text{Li}_4\text{SiO}_4$ .<sup>167–169</sup> As a result, the ICL leads to an almost linear capacity fading of the cells under a heavily flexible compression.<sup>78,170</sup> This is confirmed by the evaluation of the Li loss of the aged cathodes in Figure 5.6b. A total loss of around 95% of the cycleable Li was determined after 100 cycles in the cell under 0.84 MPa flexible high.

Hence, it can be concluded that both, a too high fixed (0.42 MPa and 0.84 MPa) and flexible (0.84 MPa) compression, have a negative influence on the lifetime of the C/Si-anodes applied in LiBs. This can mostly be attributed to their high vertical expansion upon the lithiation. In case of the fixed compression, the high expansion leads to the increase of the pressure impairing the  $\text{Li}^+$  transport in the separator. Under a heavily flexible compression, the strongly accelerated film formation and pulverization of the active material particles results in a linear decrease of the cycleable Li accelerating the capacity fading.

### 5.3 Impact of the absence of a mechanical pressure

After the effects of the fixed and the flexible compression on the aging of the C/Si|NMC811-cells have been evaluated, the absence of a mechanical pressure will be discussed in the following.

Figure 5.11 shows the average cycling performance and the standard deviation of the uncompressed cells in comparison to the cells cycled under a flexible compression of 0.84 MPa. The Coulombic efficiency, the charge, the discharge, and the CV charge capacities as well as the irreversible and the reversible swelling are plotted. Regarding Figure 5.11a, the Coulombic efficiency of the uncompressed cells shows a sudden breakdown starting at around cycle 70 approaching its minimum at cycle 83. In contrast, the compressed cells decrease only slightly with the number of cycles. Regarding the capacities of the cells, similar discrepancies can be observed in Figure 5.11b. The charge and discharge capacity of the cells uncompressed cells drops at around cycle 70 while the flexibly compressed cells show an almost linear fading. In addition, the CV charge capacity peaks starting from cycle 70 with the maximum at cycle 83. The reason for the drop of the Coulombic efficiency can be seen in Figure 5.11d, where the charge and the discharge capacities of the uncompressed cells are shown for selected cycled. Since the discharge capacity drops several cycles before the charge capacity, the ratio of both, the Coulombic efficiency, decreases significantly. Figure 5.11c depicts the irreversible and the reversible swelling of the cells. The reversible swelling of the flexibly compressed cell increases slightly during the initial cycles. After around 45 cycles, it starts to decrease with a higher negative gradient. The reason for the initial increase might be that some areas in the stack are activated during the cycling, which could be compared to the often observed initial increase of the Coulombic efficiency. This activation can be explained by a delayed contacting of previously not reachable regions of the active material. Another explanation can be the delayed soaking with the electrolyte. Furthermore, it could also be correlated with the ongoing SEI growth during the first approx. 20 cycles.<sup>136,171</sup> After the maximum capacity throughput is reached, the ICL gets dominant and reduces the reversible volume expansion. At the same time, the irreversible swelling increases almost linearly. The uncompressed cells exhibit a completely different behavior. The reversible swelling peaks at around the 70<sup>th</sup> cycle, while the irreversible swelling shows an extremely increased rise. For a better comparison, the irreversible swelling is plotted vs. the ICL in Figure 5.11e. Here, the different behavior gets even more obvious. While the flexibly compressed cells show a proportional trend of the

irreversible swelling with the ICL, this trend degenerates at around cycle 80 for the uncompressed cells. The proportional increase of the irreversible swelling with the ICL of the Si-containing cells was already described from Louli et al.<sup>131</sup> They utilized pressure sensors to evaluate the irreversible pressure increase during the cycling and correlated it with the SEI growth. Here it gets obvious that the nonlinear increase of the irreversible swelling occurs exclusively for the uncompressed cells.

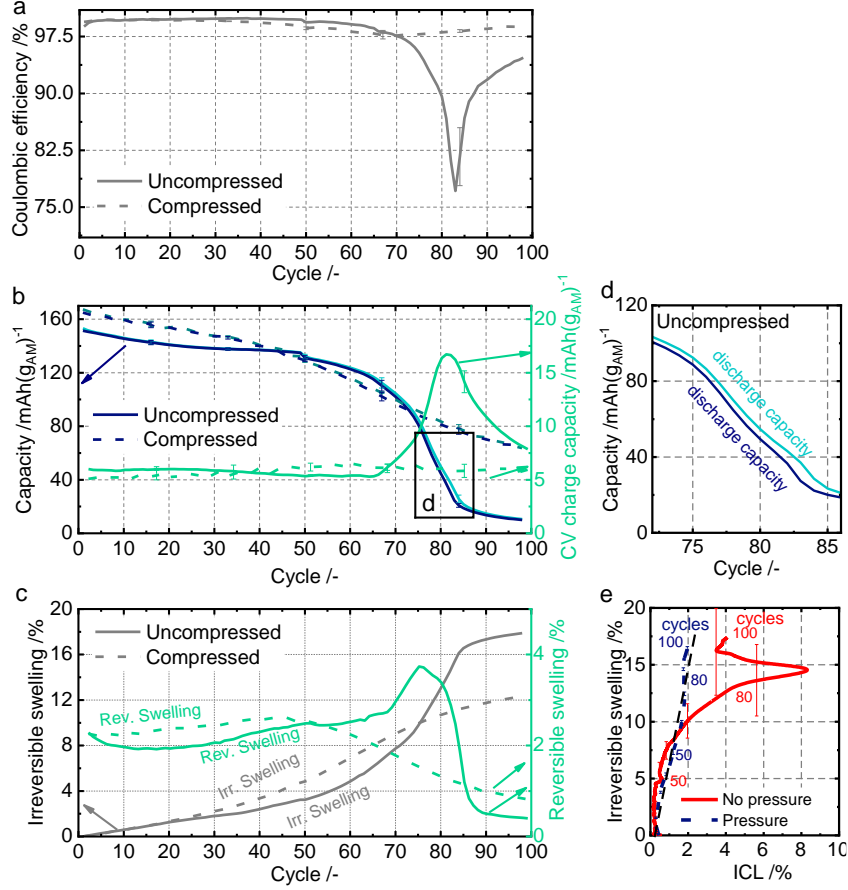


Figure 5.11: Comparison of the cycling performance of cells cycled compressed (0.84 MPa flexible) and uncompressed. (a) Coulombic efficiency, (b) charge, discharge, and CV charge capacity, (c) irreversible and reversible swelling, (d) discharge capacity for selected cycles, and (e) irreversible swelling vs. irreversible capacity loss (ICL) for cycles 1 to 100. Vertical error bars show the standard deviations of the measurements.

To understand the ongoing processes in the cycled cells, EIS measurements were conducted. Figure 5.12 shows the EIS spectra, the extracted high frequency  $R_{HF}$ , and the sum of charge transfer resistance  $R_{CT\_sum}$  of the uncompressed and the compressed cells after the formation and after the subsequent cycles. Since the compressed cells showed an almost linear aging, the EIS measurements were conducted exclusively after the formation, after 50, and after 100 cycles. Contrariwise, EIS measurements were performed after every 10<sup>th</sup> cycle with a gap at the 20<sup>th</sup> cycle for the uncompressed cell. For the fitting of  $R_{HF}$  and  $R_{CT\_sum}$ , the EC shown in Figure 5.12b was utilized, which is explained in section 2.3.1.

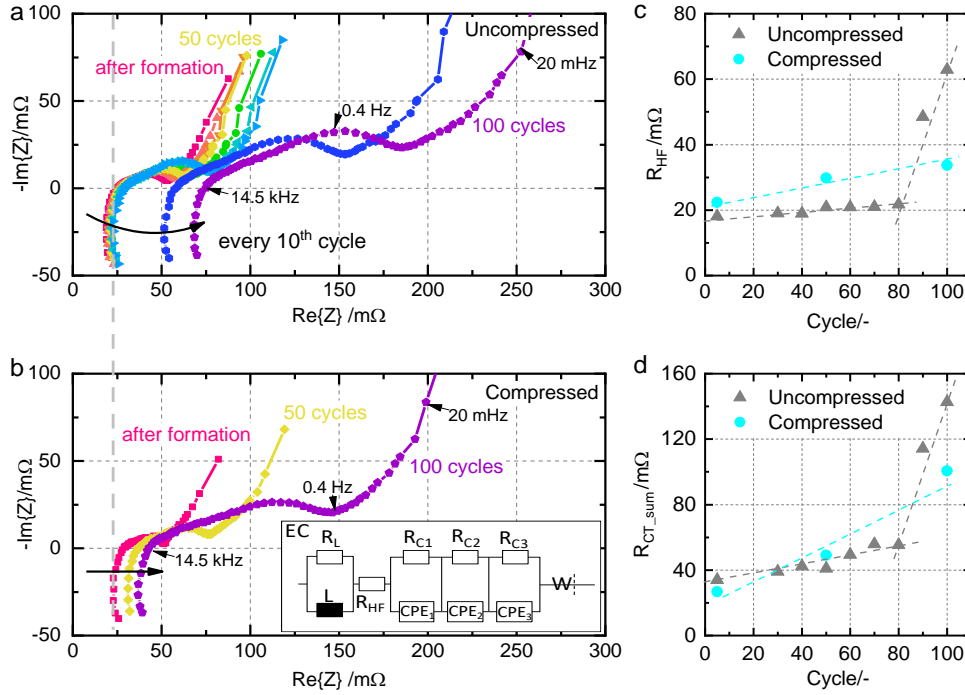


Figure 5.12: EIS measurement of the uncompressed (a) and flexibly compressed (b) cells after 5 cycles and subsequent cycles at a SOC of 50%. Extracted high frequency resistance and sum of charge transfer resistance over cycles (c and d).

Initially,  $R_{HF}$  of both cells is almost similar at around 20 m $\Omega$ . Its value increases linearly with the cycle number in case of the flexibly compressed cell (see Figure 5.12c). During the initial cycles,  $R_{HF}$  of the flexibly compressed cell exceeds  $R_{HF}$  of the uncompressed cell. The reason for this might be the already discussed repetitive passivation of the anode in the flexibly compressed cells. Due to the deposition of insulating passivation layers on the Si/C-particles, the electric conductivity can be hindered. This effect is often described in literature.<sup>77,78,172</sup> However, after around cycle 80,  $R_{HF}$  of the uncompressed cell suddenly increases to more than twice of the prior value. The same can be seen when regarding the EIS spectra in Figure 5.12a. The spectra are not changing significantly until after cycle 80. The same accounts for  $R_{CT\_Sum}$  in Figure 5.12d. Its value increases linearly until cycle 80 and almost doubles during the next 10 cycles. Interestingly, the increase of both,  $R_{HF}$  and  $R_{CT\_Sum}$ , occurs at the same cycle number of about cycle 80 as the drop of the Coulombic efficiency and the peak of the CV charge capacity were observed in Figure 5.11.

SEM cross-sections and EDX mappings of a fully charged C/Si-anode harvested from an uncompressed cell after 83 cycles were performed. To enable the investigation of the SEI film, the anode was investigated unwashed and was treaded inert without contact to air during the complete measurement. Figure 5.13 shows the SEM cross-section as well as the EDX mapping results. From the SEM cross-sections, it can be concluded that the Si/C-particles show a strong volume expansion and some parts seem to be pulverized. Furthermore, a thick passivation layer of around 5.3  $\mu m$  can be seen on the surface of the anode (see Figure 5.13a-1). F and O can be observed as deposition products of the electrolyte from the EDX mapping (see Figure 5.13b). In addition, it seems as if these deposits cannot



only be found on the surfaces of the particles but also inside of the pulverized Si/C-particles.

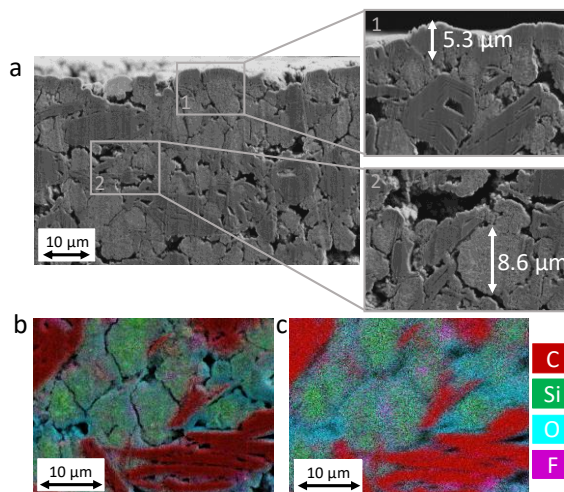


Figure 5.13: SEM cross-section (a) and EDX mappings (b and c) of a C/Si-anode harvested from a cell at a potential of 4.2 V cycled without pressure after 83 cycles.

This fact can lead to the assumption, that pulverized and cracked parts of the particles react with the electrolyte. Since the anode is harvested from a fully charged cell, all the cycleable Li should be lithiated in the anode and it should be fully expanded. However, distinct distances can be observed between the particles. This means, that these distances will get even larger during the subsequent delithiation of the anode. Similar contact loss mechanisms can be found in literature.<sup>80,154,170</sup> The derived aging phenomenon is summarized in Figure 5.14 schematically. Before the cycling, there is an electric contact between the particles, a large active surface for the charge transfer processes, and enough space for the ion transport in the electrolyte filled pores. During the cycling of the uncompressed cell, no mechanical pressure helps to hold the electric contact during the delithiation process when the Si/C-particles are shrinking. Furthermore, the repetitive volume expansion leads to cracking and pulverization of the Si/C-particles exposing new surface areas for electrolyte decomposition reactions. Consequently, the particles do not only loose electric contact due to enlarged distances but also insulating passivation deposits hinder the electron and the ion transport. Similar conclusions were made by Guo et al. describing a hindered charge transfer due to the insulating film deposits on the Si/C-particles.<sup>172</sup> Kim et al. proved an extreme reduction of the conductivity of their investigated Si/C-composite particles during cycling by scanning spreading resistance microscopy (SSRM).<sup>77</sup> Due to the repetitive volume change, the particles are mechanically separated from each other hindering the electrical transport and causing a reduction of the cell capacity. Similar results were shown by Ruther et al. employing vibrational spectroscopy on Si/C-composite|NMC532 cells.<sup>78</sup> Yu et al. found an increase of the porosity of the anode during the cycling.<sup>150</sup> They concluded that the absence of a compressive driving force leads to an extreme particle-particle detachment during the delithiation of the anode. Dong et al. proved the development of a lithiation gradient inside of the Si-particles employing operando synchrotron X-ray radiography, which causes fracture of the inner Si structure, the loss of active materials by isolation, and the formation of new SEI.<sup>31</sup>

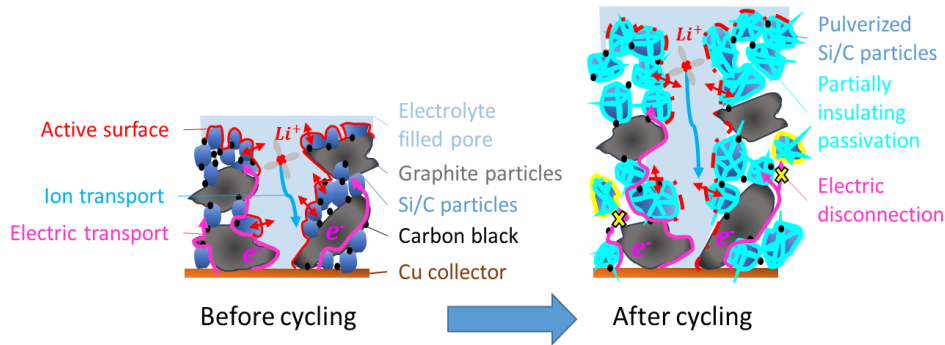


Figure 5.14: Schematic illustration of the aging mechanism in uncompressed C/Si|NMC811-cells.

Based on these assumptions, the impedance of the cells cycled uncompressed should significantly improve when applying mechanical pressure. To verify this, the cell cycled uncompressed was compressed to 0.84 MPa after the cycling at a SOC of 50%. Afterwards, the cell was cycled one time under compression and left for a relaxation time of 1.5 h before employing the EIS measurement. Figure 5.15 shows the EIS measurement result of this cell in comparison to the spectra conducted during the cycling without compression. As expected, the impedance decreased significantly. The compression seems to reconnect some beforehand disconnected particle-particle contacts decreasing the electric resistance in the cell. Due to the reconnection of the particles, they become available to participate at the charge-transfer. Hence, a drastic reduction of the charge-transfer semicircle can be observed. This result agrees well with the schematic aging mechanism presented in Figure 5.14.

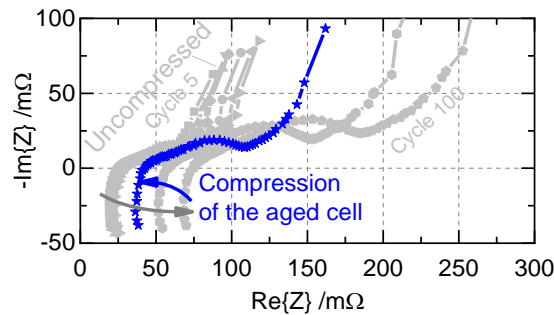


Figure 5.15: EIS spectra of the uncompressed cell for selected cycles and spectrum of the subsequently compressed cell.

Still, the questions remains, why the reversible expansion is increasing and decreasing again and how this correlates to the increase of the CV charge capacity and the drop of the Coulombic efficiency observed in Figure 5.11. Therefore, the expansion of the cycled cells is evaluated closely. Figure 5.16 shows the voltage and the reversible swelling versus the specific capacity of the uncompressed and the compressed cell for selected cycles. Since the capacity fading proceeds linearly until around cycle 65, the shown cycles are selected between cycle 65 and 98. A strong increase of the hysteresis of the voltage curves of the uncompressed cell can be observed in comparison to the compressed cell (see Figure 5.16a and b). Starting at cycle 75, the CV charging capacity increases drastically. After cycle 83, the remaining capacity of the uncompressed cells drops below  $30 \text{ mAh (g}_{\text{AM}})^{-1}$ . In contrast

to that, the compressed cycled cell shows only a linear shift of the voltage curves to lower capacities, while the hysteresis stays constant. These findings confirm the results of the EIS measurement showing a linear increase for the compressed cell (see Figure 5.12). Regarding the swelling curves in Figure 5.16c and d, the reversible swelling of the uncompressed cell exhibits a completely nonlinear trend in comparison to the compressed cell. The reversible swelling is increasing suddenly and reaches the maximum value at cycle 75. Afterwards, the amplitude is decreasing again, while the hysteresis between the charge and the discharge expansion is rising.

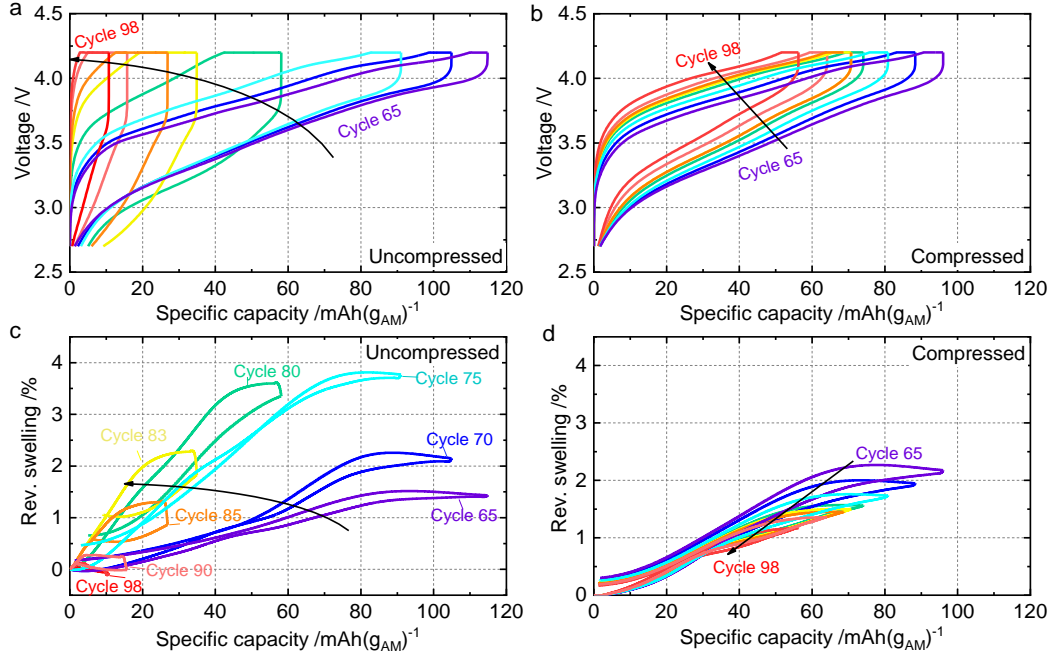


Figure 5.16: Voltage (a and b) and reversible swelling (c and d) over the specific capacity of the uncompressed and the compressed cells plotted for selected cycles.

For a better understanding of the measurement data, Figure 5.17 shows the reversible swelling plotted versus the voltage instead of the specific capacity.

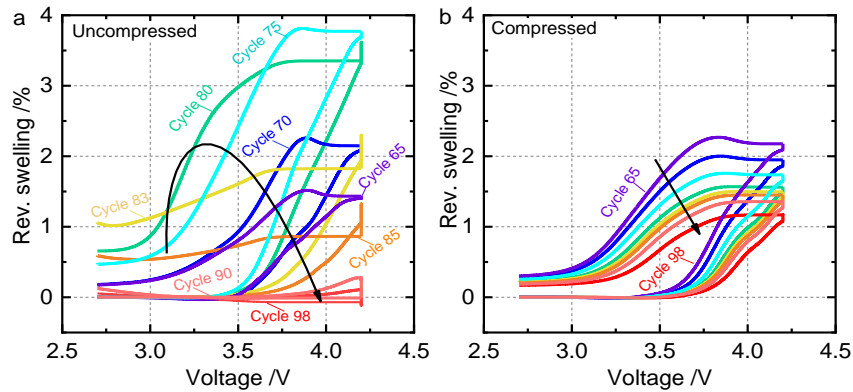


Figure 5.17: Reversible swelling over voltage of the uncompressed (a) and the compressed (b) cells for selected cycles.

As expected, the reversible swelling of the compressed cell in Figure 5.17b shows a linear decrease of the amplitude. At the same time, the hysteresis of charge and the discharge



expansion is not rising. Contrarily, the reversible swelling of the uncompressed cell starts to increase drastically at cycle 75. Afterwards, at cycle 80 a conspicuous behavior of the expansion during the CV charging step at a constant cell voltage of 4.2 V can be observed. As can be seen in cycle 80 to 85, the cell is expanding and shrinking while the cell voltage is hold at 4.2 V. Hence, the CV charging step has to be evaluated closer. Figure 5.18a and b show the expansion of the uncompressed and the compressed cell during the CV charging step.

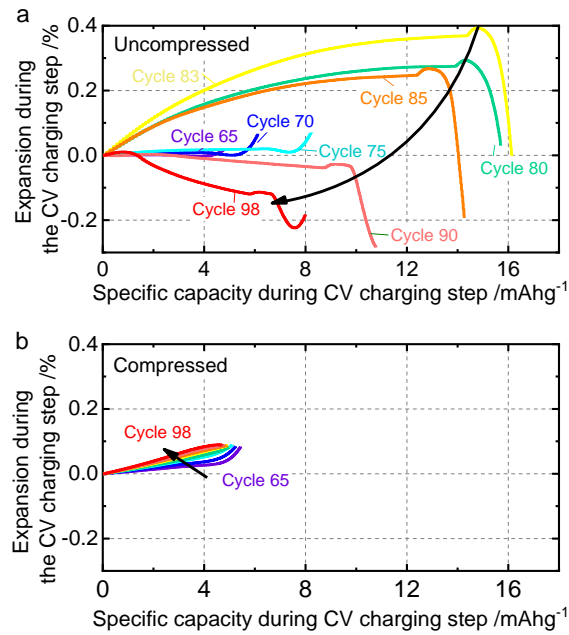


Figure 5.18: Expansion during the CV charging step over the specific capacity for the uncompressed (a) and the compressed (b) cells for selected cycles.

The expansion during the CV charging step of the uncompressed cells evinces an extreme rise with a subsequent shrinking. This phenomenon is highest at cycle 83 where the CV charge capacity peaks and the Coulombic efficiency exhibits its minimum (see Figure 5.11a). In addition to the contact loss mechanism illustrated in Figure 5.14, there is an unexpected effect occurring during the CV charging step forcing the cell to expand and to shrink. There are not too many possible reasons for such a behavior. One possible reason could be Li deposition on the anode surface. Since it is well known, that Li deposition mostly occurs when the cell is fully charged<sup>76</sup> and that the deposited Li can re-intercalate to the anode,<sup>145,173</sup> this might be the case for the observed abnormality of the expansion. However, this can be excluded as explanation since the uncompressed graphite|NMC622-cells described in section 4.4 tend to Li deposition.<sup>126</sup> No abnormal expansion behavior was observed during any tests. Furthermore, literature in the re-intercalation of Li into the anode reports of a long-term process of several hours.<sup>174,175</sup> Hence, such an abrupt decrease of the expansion cannot be explained by this effect. Another possible reason for the measured expansion during the CV charging step might be gas formation and subsequent diffusion of the gas to the adjoining gas bag of the cell. Such a behavior was often detected during

the initial formation cycle of the C/Si|NMC811-cells. Figure 5.19a and b show the expansion of an uncompressed cell in comparison to a compressed cell during the first and third cycle of the initial formation of the cells.

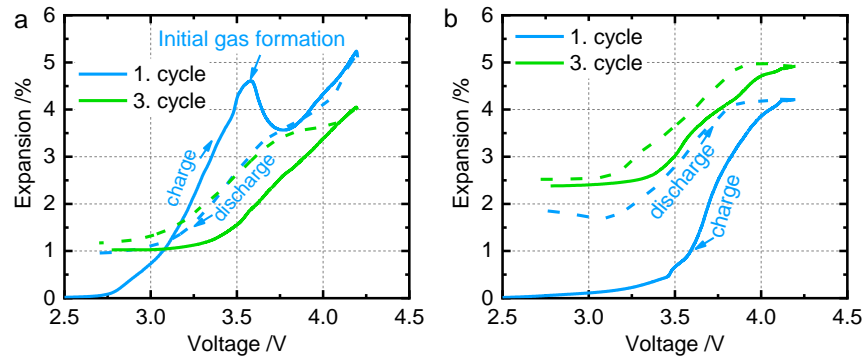


Figure 5.19: Expansion during the initial formation cycles of an uncompressed (a) and a compressed (b) cell.

The expansion of the uncompressed cell peaks at a voltage of around 3.6 - 3.7 V indicating the formation of gas. It is well known that most of the initial gas formation during the SEI formation takes place in this voltage range.<sup>176–178</sup> At an increased voltage, the cell thickness shrinks again suggesting, that the evolved gas moved out of the cell stack to the adjoining gas bag. However, this only applies for the uncompressed cell in Figure 5.19a. The compressed cell in Figure 5.19b shows no gas peak. The reason for this is that the mechanical compression forces the formatted gas directly to the gas bag ensuring that the expansion measurement is not distorted. Coming back to the emerging expansion peak during the CV charging step in Figure 5.18, the similarity to the initial gas formation peak in Figure 5.19 is undeniable. Furthermore, this hypothesis is confirmed by the fact, that the uncompressed cells were completely dry without remaining electrolyte during the cell opening after the cycling. All cells cycled under compression showed remaining electrolyte in the stack. This suggests that the decomposition of all remaining parts of the electrolyte in the stack leads to gas formation, which is detectable by the operando expansion measurement.

Figure 5.20 shows a schematic illustration of the proposed mechanism leading to gas formation during the CV charging of the uncompressed cells.

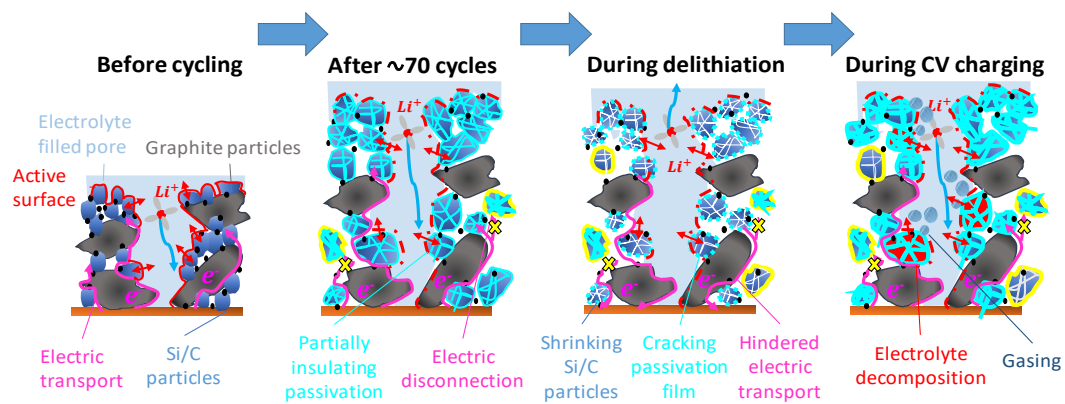


Figure 5.20: Schematic illustration of the gas formation during the accelerated aging of the uncompressed cells.

As already discussed above, the C/Si-anode suffers from particle pulverization and cracking of the protective passivation layer due to the high volume change of the Si/C-particles. Therefore, the passivation film has to be repaired every cycle under electrolyte consumption. This status is represented in Figure 5.20. After around 70 cycle, the particles are pulverized exposing new surface for electrolyte decomposition reactions and film formation. Due to high expansion of around 19  $\mu\text{m}$  per anode, some particle might be electrically disconnected. These particles are marked in yellow and cannot participate at the charge-transfer reactions anymore. During the delithiation of the uncompressed anode, when the Si/C-particles are shrinking, there is no driving force to hold to contact of the particles. More and more particles get electrically disconnected. Therefore, Li is trapped not only in the passivation films, but stays lithiated in the particles contributing to the high ICL (see Figure 5.6b). During the subsequent charging steps of the cell, this process repeats, and the Si/C-particles participate unequally to the lithiation and delithiation. Furthermore, the passivation film has to be repaired every cycle under electrolyte consumption and new Si/C-particles become disconnected. At some point, the electrolyte consumption gets too high, so that almost no electrolyte is available anymore. However, especially during the CV charging at low currents, the particles get lithiated anyway. This leads to the significant increase of the CV charging capacity. This charge cannot be distributed on all particles equally and some particles might be forced to form higher lithiated Si-alloys. The combination of these effects seems to lead to the formation of gas as side-reaction of the electrolyte decomposition causing the cell to expand abnormally during the CV charging step. The group of Dahn et al. investigated the aging behavior of LCO|Si/graphite pouch cells and found a similar fading mechanism with a linear capacity retention followed by a sudden death of the cells.<sup>179</sup> By employing gas evolution measurements and differential voltage analysis, they concluded that SEI growth and SEI repair is responsible for the linear capacity fading. Whereas the sudden death of the cells is caused by the depletion of the FEC in the electrolyte. These results perfectly match the behavior observed herein.

## 5.4 Summary of the influence of mechanical pressure on C/Si|NMC811-cells

The type of mechanical pressure influences the performance and the aging behavior of the C/Si|NMC811-cells in a number of ways. The slightly fixed (0.08 MPa), and medially flexible (0.42 MPa) compression showed the most beneficial influence in terms of the capacity fading of the cells. In case of a heavier fixed compression (0.42 MPa and 0.84 MPa), the prevention of the vertical expansion of the cells leads to the emergence of pressure hot spots in areas with a high current density. Since the capacity of the Si in the C/Si-anode is utilized to 100%, the Si/C-particles exhibit a high volume change forcing the anode to expand into the separator and the cathode. Due to the imprint and the penetration of the separator, pore closure and a strong decrease of the  $\text{Li}^+$  transport properties is the result. This in turn leads to capacity fading. Contrariwise, the repetitive cracking and reformation of the protective passivation layer leads to a linear aging of the cells under a heavy flexible compression (0.84MPa). In the uncompressed cells, the absence of the mechanical pressure holding the

contact between the particles during the delithiation and the shrinking of the Si/C-particles, leads to a significant contact loss. As a result, some particles lost their connection and cannot contribute to the de-/lithiation anymore. Hence, the charge is inhomogeneously distributed. Together with the repetitive cracking and exposure of surface regions where new SEI has to be formed under electrolyte consumption, the uncompressed cells show a sudden drop of the Coulombic efficiency, a decrease of the capacity, and a significant increase of the swelling. This increase of the swelling was attributed to the CV charging of the cells and can be explained by the formation of gas as side reaction of the immense electrolyte decomposition. Summarizing, the operation conditions of Si-containing cells with a high vertical expansion have to be adjusted carefully depending on the present system.

## 6 Influence on the aging of Si/C|NMC811-cells with particle included porosity

In contrast to the C/Si-anode discussed in section 6, the concept of the Si/C-anode regarded herein is to prevent the vertical expansion by an embedded porosity in the C-matrix of the composite (see Figure 3.1 in section 3.1). This is a well-established approach in literature.<sup>33,34,180,181</sup> By encapsulating Si-nanoparticles in a pomegranate like carbon structure, Liu et al. showed a high cycling stability with a relatively high volumetric capacity of  $1270 \text{ mAh cm}^{-3}$ .<sup>180</sup> Xu et al. introduced a watermelon-inspired Si/C-structure providing a high capacity retention of 75% after 500 cycles with a relatively high areal capacity of  $2.54 \text{ mAh cm}^{-2}$ . Other groups proposed to control the porosity of their Si/C-composite by encapsulation in a carbon core-shell<sup>34</sup> or the utilization of pore forming agents during the electrode manufacturing.<sup>33</sup> These material designs join several advantages i.e. providing void space for the Si expansion without the risk of particle cracking, high electric conductivity due to the carbon framework, and limiting SEI formation to the carbon surface.<sup>180</sup>

However, all approaches regarding an embedded porosity in the particle structure reported in literature are accomplished based on lab-scale coatings and coin cell measurements. Therefore, a Si/C-composite providing embedded porosity in a C-matrix is evaluated herein in stacked pouch cells as well as in large-format prismatic cells. This enables the understanding of the behavior of such new materials in applications relevant for the industrial scale. To prevent cracks of the C-matrix, the capacity of the composite is limited to 30%, i.e.  $560 \text{ mAh g}^{-1}$ . This partial lithiation concept showed promising results in literature.<sup>41,125,182–184</sup> Due to the reduced volume expansion, the composite is protected from cracking and the necessity of a repetitive SEI formation is reduced.<sup>38,125</sup>

Firstly, the pressure-dependent cyclic aging and the expansion behavior of the Si/C|NMC811-cells will be discussed in detail in section 6.1 taking into account influences as the calendaring density and the applied pressure on pouch cells. In addition, the shift of the NMC811-cathodes will be examined when cycled in cells with Si-containing anodes in section 6.2. Finally, the results gained on pouch cell level will be transferred to large-scale prismatic (PHEV1) cells in section 6.3.

Some of the results presented in the following section are published<sup>124</sup> and are reproduced with the permission of the journal. Whereas, all presented results on pouch and PHEV1 cell level were generated and evaluated as well as presented by me.

### 6.1 Pressure-dependent cyclic aging and expansion

Stacked Si/C|NMC811-cells were cycled at different flexible and fixed compressions as well as uncompressed. Due to the sensitive geometry of the C-matrix of the Si/C-composite, the anodes were utilized calendared and uncalendered with densities of  $0.9 \text{ mg cm}^{-3}$  and  $0.74 \text{ mg cm}^{-3}$ , respectively. In the following, the results of the cycling with operando expansion and pressure mapping will be presented in section 6.1.1. Afterwards, the outcome

of an extensive post-mortem analysis of the anodes and the separators as well as the cathode losses will be shown in section 6.1.2 and will be summarized in 6.1.3.

### 6.1.1 Cyclic aging and pressure distribution

Figure 6.1 shows the specific capacity, the Coulombic efficiency, the irreversible swelling, the reversible swelling, and the total swelling during 150 cycles of cells under flexible compression with calendered and uncalendered anodes.

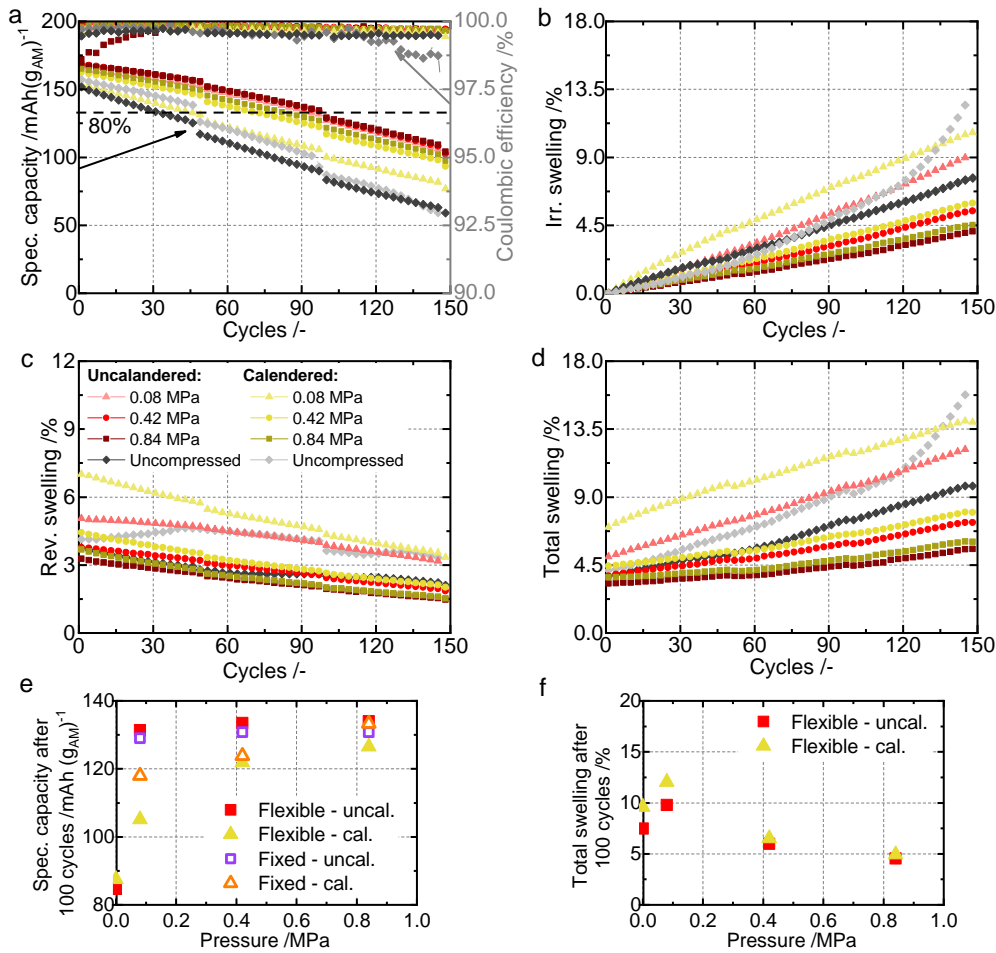


Figure 6.1: Cycling performance of differently compressed Si/C/NMC811-cells with calendered and uncalendered anodes. Specific capacity and Coulombic efficiency (a), irreversible swelling (b), reversible swelling (c), and total swelling (d) over 150 cycles as well as the specific capacity (e) and the total swelling (f) after 100 cycles. Reused in parts.<sup>124</sup> ©2020 Wiley.

Enabling a better comparison, the specific capacity and the total swelling of all cells compressed at various pressure configurations after 100 cycles are summarized in Figure 6.1e and f. The cells under fixed compression show the same trend as obtained by the cells cycled under flexible compression. To improve the clarity, the cycling results obtained with cells under fixed compression are not illustrated in Figure 6.1a-d but can be found in the supplementary material in Figure S0.3 and are added to Figure 6.1e providing the resulting specific capacities after 100 cycles. As can be seen in Figure 6.1a, the highest specific capacity is observed for the 0.84 MPa heavily compressed cells. After 100 cycles, the 0.84

MPa flexibly compressed cells with uncalendered anodes show the highest remaining capacity of 81.1%. Generally, the cells with calendered anodes perform worse than the cells with uncalendered anodes. Their highest capacity retention of 79.2% can be gained for the 0.84 MPa fixed compression (see Figure 6.1e). The reason for the generally reduced capacity is most likely related to cracking of the C-matrix of the Si/C-composite active material during the calendaring process. However, with an increasing applied pressure, the performance approaches the cells with uncalendered anodes. It seems that the negative influence of the calendaring process is diminished by a higher mechanical compression on the pouch cell. One possible reason for this could be the lower reversible swelling of the heavier compressed cells, i.e. the cells compressed to 0.08 MPa show a reversible swelling of 7.0% while the cells compressed to 0.84 MPa only expand by 3.6% during their initial cycle (see Figure 6.1c). The lower repetitive expansion reduces the occurrence of cracking of the particles and fracture of the protective SEI layer. Hence, less Li is irreversible lost in the anode in each cycle reducing the capacity fading.

Furthermore, the swelling of the cells with calendered anodes is generally higher in comparison to the cells with uncalendered anodes (see Figure 6.1b, c, d and f). This can be explained by the void space provided in the anodes. The same behavior was determined for the graphite|NMC622- and C/Si|NMC811-cells in section 4 and 5. In case of the calendered anode, there is less void space available for the volume expansion of the active material leading to a higher vertical expansion compared to the uncalendered anode providing a higher porosity. Once, again this behavior is reduced by highering the applied pressure on the cells (see Figure 6.1f). It seems that the higher pressure helps to utilize the void space in the anode material, preventing the vertical expansion. In general, it has to be noted that the expansion of the 0.84 MPa flexibly compressed cells with a total swelling of 5.6% after 150 cycles is relatively small for Si-containing anodes. The reason for this is the partial lithiation to only 30% of the available Si capacity and the provided void space in the C-matrix. The uncompressed cells in Figure 6.1 show a comparable behavior as observed for the uncompressed C/Si|NMC811-cells in section 5.3. The capacity fading as well as the swelling is much higher. This behavior suggests that the material suffers from contact loss due to the absence of a homogeneous pressure on the cells. In addition, the cells cycled under a slightly fixed pressure of 0.08 MPa show a high capacity fading and an accelerated irreversible swelling. This might indicate that the application of a 0.08 MPa flexible pressure is not enough to prevent contact loss in the Si/C-anodes. Similar results were observed for the C/Si|NMC811-cells in section 5.1. For all compressed cells, the reversible swelling linearly decreases with the cycle number. This indicates a linear ICL due to an ongoing SEI formation on the anode.

Operando pressure mapping measurements were conducted to assess the pressure distribution during the cycling of the Si/C|NMC811-cells. Figure 6.2 shows the pressure mapping results of two cells cycled under 0.84 MPa fixed and 0.84 flexible compression with uncalendered anodes after the formation, after 50 and 100 cycles in the fully charged state. The pressure distribution at the large and at the wide side across the cells' surfaces is plotted separately for the regions with the highest inhomogeneities. Regarding the cell under fixed compression, the average pressure increases from initially 0.84 MPa to 1.0 MPa after 100



cycles. The distribution remains mostly uniform with a slightly increased pressure close to the anode terminal. The same trend is observed for the flexibly compressed cell. However, the average pressure is not changing at all during the cycling. As discussed for the C/Si|NMC811-cells in section 5.2, the higher pressure close to the anode terminal is in good accordance with the literature determining a higher current density in these regions.<sup>151–153</sup> However, in contrast to the C/Si|NMC811-cells exhibiting a high pressure increase (see Figure 5.2), the partial lithiation and the provided void pore volume in the composite helps to reduce the expansion of the Si/C-anode and keeps a homogeneous pressure distribution even at heavily fixed compression.

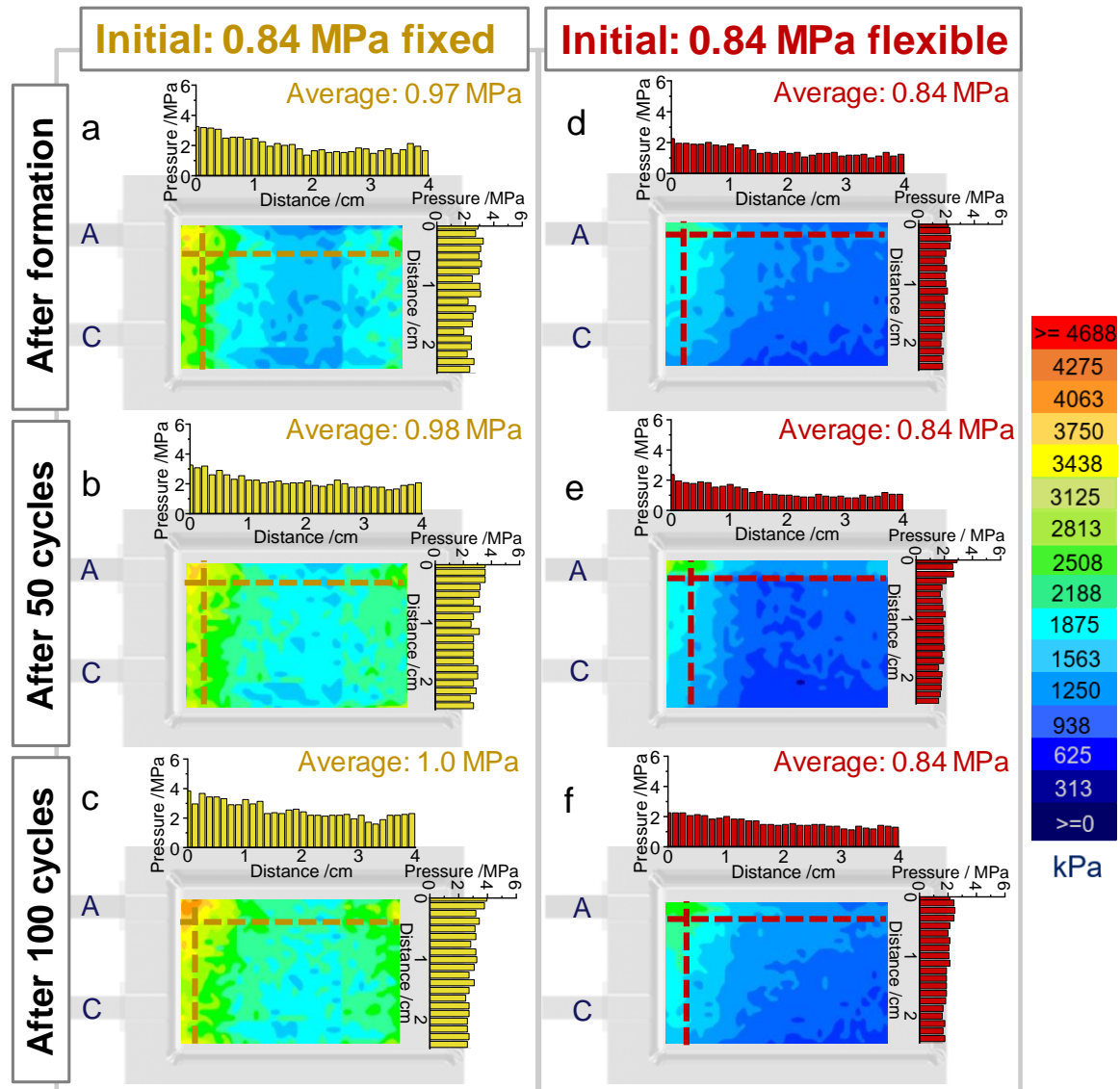


Figure 6.2: Pressure mapping of Si/C|NMC811-cells under an initial 0.84 MPa fixed (a-c) and 0.84 MPa flexible (d-f) compression. The mappings were recorded after the formation (a, d), after the 50<sup>th</sup> cycle (b, e), and after the 100<sup>th</sup> cycle (c, f). Reused in parts.<sup>124</sup> ©2020 Wiley.

EIS measurements were conducted to understand the cyclic aging tests presented in Figure 6.1. Figure 6.3 shows the Nyquist impedance spectra of the cells cycled at a 0.84 MPa flexible and 0.42 MPa fixed pressure and uncompressed with calendered and uncalendered anodes. The measurements were conducted at a SOC of 100% after the formation (initial),

after 50 cycles, and after 100 cycles. The spectra of the cells under fixed and flexible pressure show a similar impedance increase during the cycling. Furthermore, the cells with calendered and uncalendered anodes overlap completely. The high frequency part of the spectra stays constant during the cycling. Contrariwise, the spectra of the uncompressed cells shows a severe increase in both, the semicircle as well as the high frequency part. The extreme increase of the high frequency resistance indicates a loss of contact and might be influenced by the thickening of the passivating film, which reduces the conductivity in the anode. A differing behavior of the uncompressed cells with calendered and uncalendered anodes can be observed. The high frequency resistance of the uncompressed cells with calendered anodes increases much more than of the cells with uncalendered anodes. After 100 cycles, the high frequency resistance of the former reaches a value of 235.5 m $\Omega$  while the latter only shows a resistance of 121.5 m $\Omega$ . This agrees well with the theory that the calendaring process leads to additional cracking of the Si/C-composite accelerating the contact loss and subsequent capacity fading.

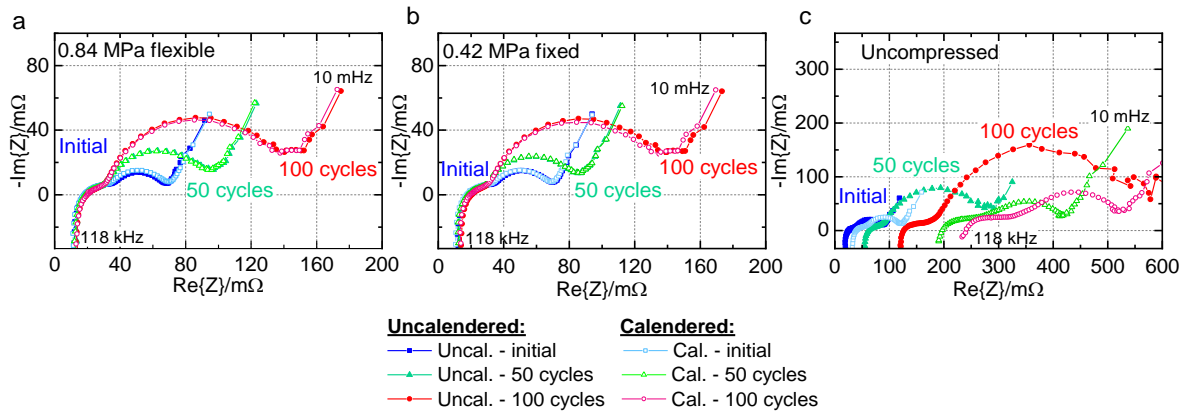


Figure 6.3: EIS spectra of Si/C|NMC811-cells cycled at a 0.84 MPa flexible (a), 0.42 MPa fixed pressure (b) and uncompressed (c) with calendered and uncalendered anodes. The measurements were conducted at a SOC of 100% after a relaxation time of 1.5 h after the formation (initial), after 50 cycles, and after 100 cycles. The axis scaling of the spectra of the cells cycled without compression differs from the others.

### 6.1.2 Post-mortem investigations

To evaluate the aging mechanism of the Si/C|NMC811-cells, SEM cross-sections of the aged anodes were prepared and are compared with the pristine ones. Since the cycling and EIS results presented above showed no severe differences of the compressed cells with calendered and uncalendered anodes, the focus will be put on the uncalendered anodes in the following. Figure 6.4 depicts SEM cross-sections of the pristine (Figure 6.4a) and of the harvested anodes from a cell cycled without compression (Figure 6.4b) and under 0.84 MPa flexible compression (Figure 6.4c). All shown anodes are uncalendered. The concept of the Si/C-composite, i.e. encapsulating the Si-particles and providing void pore volume, gets more distinct in Figure 6.4a-1. After the cycling in an uncompressed cell, the one-side coating thickness increased drastically to 134.9  $\mu\text{m}$  from its initial value of 85.5  $\mu\text{m}$  (compare Figure 6.4a and b). In addition, to the observable detachment of the Si/C-composite particles from each other, some severe cracks through the particles can be seen

in Figure 6.4b-1. Closer examinations in Figure 6.4b-2 and b-3 show a foam-like film formation on the Si-particles inside the Si/C-composite. This indicates that the Si/C-composite gets untight due to the high volume expansion exposing the Si to the electrolyte where decomposition reactions can occur.<sup>124</sup> On the contrary, the anode cycled in a heavily compressed cell only shows a lower thickness increase, a more dense structure, no cracks through the particles, and only less foam-like film formation exclusively outside of the composite particles (see Figure 6.4c). It is obvious that the reduced volume expansion due to the applied pressure is beneficial for the aging of the anode.

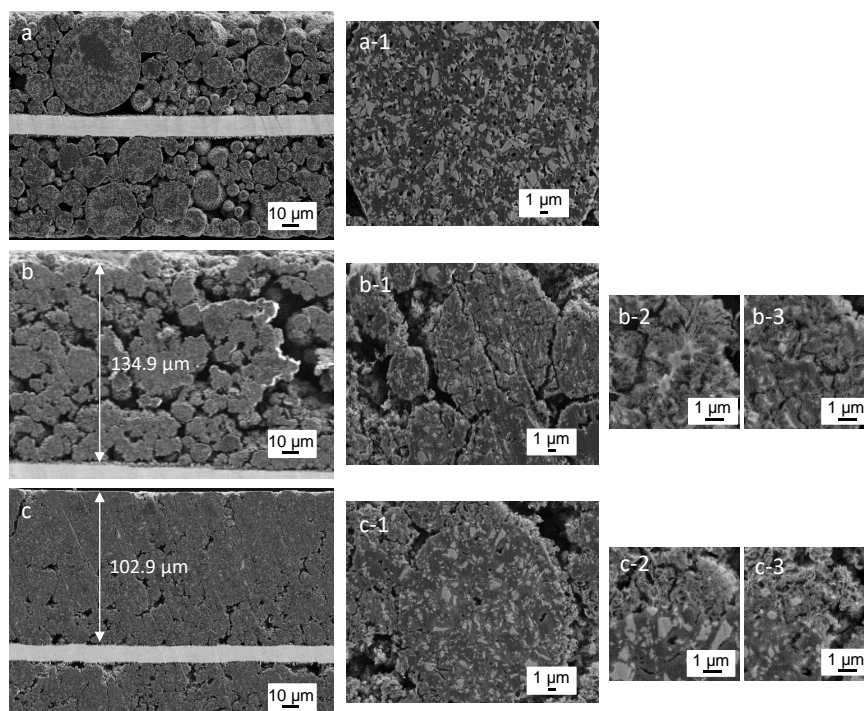


Figure 6.4: SEM cross-sections of the pristine Si/C-anode (a) as well as harvested Si/C-anodes harvested after 200 cycles without compression (b) and under 0.84 MPa flexible compression (c). All anodes are uncalendered and images at different magnifications are provided. Reused with permission.<sup>124</sup> ©2020 Wiley.

Figure 6.5 shows the porosity of the aged anodes determined by Mercury porosimetry. The porosities were measured for calendered and uncalendered Si/C-anodes harvested of cells cycled at different flexible pressure as well as without pressure. Interestingly, the porosity of calendered anodes increased from initially 50.4% to around 54.0% during the cycling without compression. At the same time, a reduction of the porosity of the uncalendered anodes can be observed. Similar behavior can be seen for the anodes harvested from the cells cycled at a pressure of 0.08 MPa. The calendered anodes show a higher porosity than the uncalendered ones. Therefore, it seems that the calendered anodes experience a much higher expansion causing a higher porosity compared to the uncalendered anodes. In case of the anodes of the uncompressed cells, the observed contact loss might lead to an additional increase of the porosity. This agrees well with the operando determined total swelling of the cells cycled without compression. The total swelling of the cell with calendered anodes was 16.0% compared to 9.8% of the cell with uncalendered anodes after 150 cycles (see Figure 6.1). A second assumption is confirmed by the porosity measurements in Figure 6.5. As can be seen, the remaining porosity is decreasing with an increased pressure on the

cells. Hence, the applied pressure seems to force the Si/C-composite to expand into the pores. In addition, the high expansion of the calendered anodes seems to be hindered when compressed at a higher pressure. Furthermore, the remaining porosity is decreased for the calendered anodes compared to the uncalendered ones at pressures of 0.42 MPa and 0.84 MPa. This indicates that the applied pressure is high enough to reduce the expansion in vertical direction forcing it to expand in the pores. This is why the remaining porosity of both is reduced dramatically compared to their initial values. Obviously, the Si/C-composite is expanding into the pores reducing the pore volume. Additional film formation and electrolyte decomposition might further reduce the pore volume.

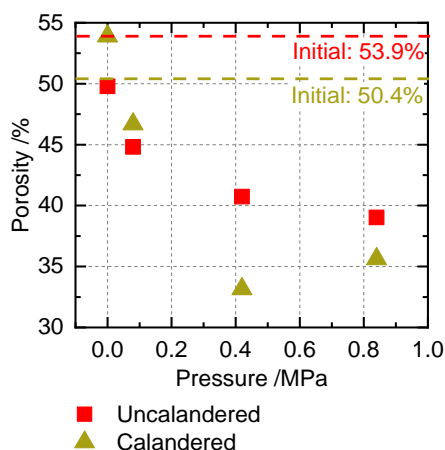


Figure 6.5: Remaining porosity over the applied pressure of the Si/C-anodes harvested from Si/C|NMC811-cells cycled at different pressure with calendered and uncalendered anodes.

Figure 6.6 shows the SEM top views of the separators harvested from Si/C|NMC811-cells with uncalendered anodes cycled at different compression at a flexible pressure of 0.08 MPa and 0.84 MPa, a fixed pressure of 0.08 MPa and uncompressed. The harvested separators from cells with calendered anodes appeared the same as of the cells with uncalendered anodes. Hence, the herein shown results focus on the separators of cells with uncalendered anodes. The thickness of the separators was measured during the cell opening and is included in the images. On both, the separators harvested from the cells cycled uncompressed and under 0.08 MPa flexible compression, circular depositions can be observed (see Figure 6.6a and b). In addition, the thickness of these separators increased to high values of 33.7  $\mu\text{m}$  and 34.4  $\mu\text{m}$  compared to the initial separator thickness of 25  $\mu\text{m}$ . The images with higher magnifications indicate the presence of many small particles in the polymeric grid of the separators, which were not removed during the prior dip washing in DMC. EDX measurements of these depositions confirmed a high amount of F (see supplementary material Figure S0.2). Therefore, it seems as if the ongoing decomposition of the electrolyte leads to depositions on the separators. Contrarily, much less deposition can be observed on the separators harvested from cells cycled under compression (see Figure 6.6c and d). It can be concluded that the parasitic reactions leading to the deposition are enhanced in the uncompressed and slightly flexible (0.08 MPa) compressed cells. This agrees well with the cyclic aging results shown in Figure 6.1. The cells cycled uncompressed and under 0.08 MPa flexible pressure showed a higher capacity fading and an accelerated increase of



the irreversible swelling (see Figure 6.1). In addition, the analysis of the SEM cross-sections of the anodes harvested from cells cycled uncompressed confirmed the more pronounced film formation (see Figure 6.4). Therefore, it seems that the absence of a high enough mechanical pressure causes an enhanced electrolyte decomposition and passivation of the anode, which is reflected by the deposition of the electrolyte decomposition products in the separator. For this specific material, this means that the protective C-matrix breaks during the cycling exposing the embedded Si to the electrolyte. Here it has to be noted that a slightly flexible pressure of 0.08 MPa is not enough to prevent these aging effects.

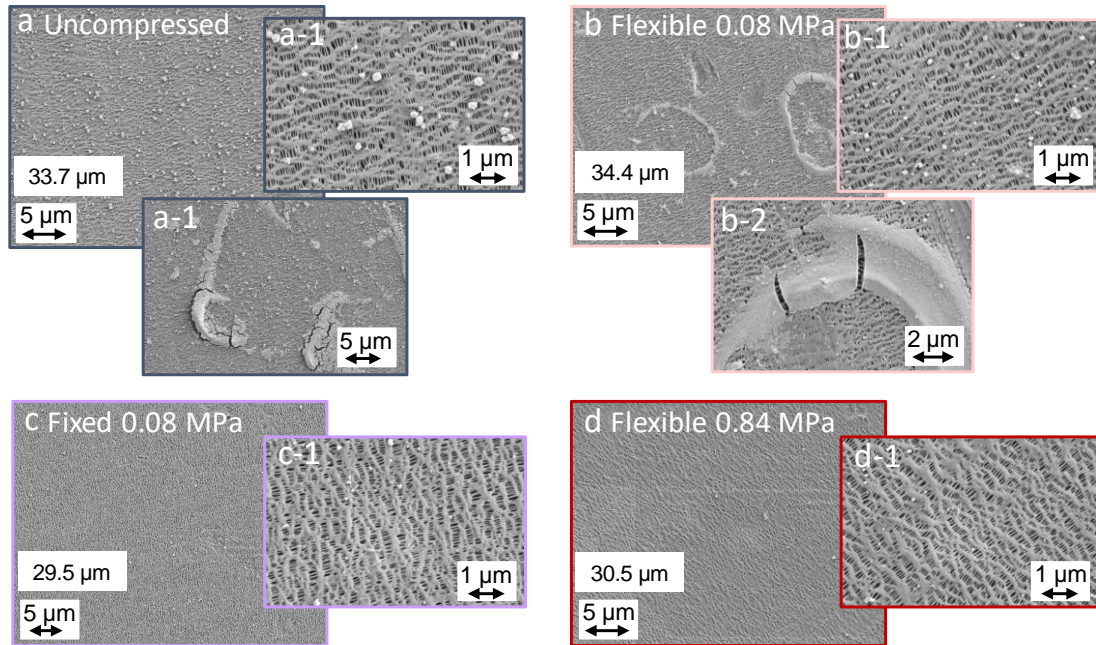


Figure 6.6: SEM top-views of separators harvested from cycled Si/C/NMC811-cells at different compression and uncompressed. SEM images are shown at different magnification. The post-mortem thickness of each separator is marked in the images.

However, in case of a heavily flexible compression or a fixed compression, the lifetime of the cells is improved significantly (see Figure 6.1). On the separators harvested from the cells cycled under slightly fixed or heavily flexible pressure, much less electrolyte decomposition products can be found. In addition, it has to be mentioned, that the separators of all cells cycled under fixed compression were not penetrated as was observed for the separators of the C/Si|NMC811-cells in section 5.2. Contrarily, all harvested separators from cells cycled under fixed compression showed a slight thickness increase or constant thickness after the cycling. The reason for this is obvious. Due to the lower volume expansion of the Si/C-anodes, the cathode and the separator are not compressed. This is confirmed by the pressure mapping results presented in Figure 6.2.

Finally, the post-mortem analysis is completed by an investigation of the remaining capacity of the NMC811-cathodes harvested from the cells after 200 cycles. The provided results are concentrated on the flexible compression, since no difference was observed in the cycling and the pressure distribution. Figure 6.7 shows the remaining Li and the remaining NMC content, which was evaluated by employing the method described in 3.2.5. The initial capacities of the full cells during the formation are indicated as a reference value. The ICL

and the loss of NMC capacity are shown in proportion to this initial capacity for each cell. The remaining cyclable Li of all harvested cathodes shows a maximum value of  $10.5 \text{ mAh (g}_{\text{AM}})^{-1}$ , which is around 6% of the initial value. This is in good agreement with the beforehand presented results of the cathodes harvested from the cycled C/Si|NMC811-cells in Figure 5.6b exhibiting a remaining Li content of around 11.4% after 100 cycles. The compression as well as the calendering process seem to have no severe influence on the Li loss. All cells show a loss between 94.0 – 98.0% of their Li even though the relative capacity loss of the pouch cells was only between 65.1% and 76.2%. Here, it has to be noted that the ICL is determined in coin cells in a voltage window of 3.0 – 4.3 V vs.  $\text{Li/Li}^+$  (see section 3.2.5), while the Si/C|NMC811-cells are cycled in a full cell voltage window of 2.7 – 4.2 V. Therefore, one possible reason for the differing values might be the shift of the cathode potential to higher values than 4.3 V, which would explain the higher remaining capacity in the pouch cells. At the same time, the NMC811 capacity of the harvested cathodes in Figure 6.7 decreased significantly for all pressure levels. This might be one indication for a potential shift of the cathode and will be discussed in detail in section 6.2.

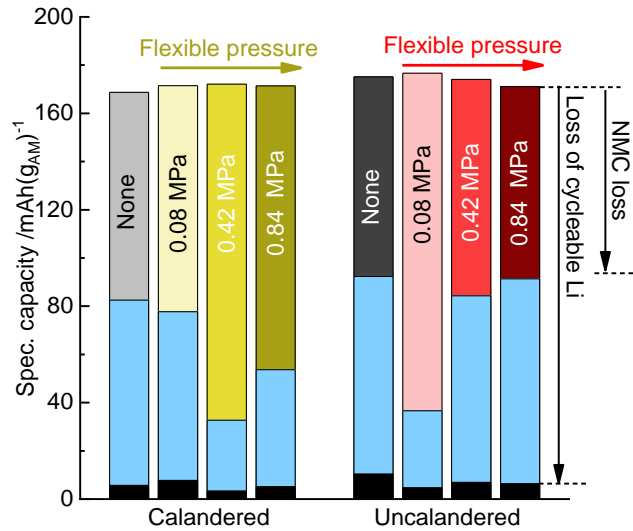


Figure 6.7: Evaluation of the remaining Li and the remaining NMC in comparison to the initial capacity of the NMC811-cathodes harvested after 200 cycles in pouch cells under different flexible compression and with calandered and uncalandered Si/C-anodes.

At the same time, the mass of the cathodes decreased by maximum values of 5.7% and the mass as well as the thickness of the Si/C-anodes increased drastically. Figure 6.8 shows the change of the anode and cathode mass as well as of the thickness. The Si/C-anodes showed a maximum mass increase of 87.8% in case of an uncalandered anode cycled in a cell under 0.84 MPa flexible compression and a maximum thickness increase of 91.2% for a calandered anode cycled in a cell without compression (see Figure 6.8 a and c). The decrease of the cathode mass with the concurrent increase of both, the mass and the thickness, of the Si/C-anode confirm the repetitive SEI growth and trapping of cycleable Li. Since the average anode mass increased more than the cathode mass decreased, it can be derived that the mass increase of the anode is not only caused by Li trapping but is strongly increased by electrolyte decomposition products. Similar results were found by our project partners

based on coin cell cycling results and are presented in our recent publication.<sup>124</sup> In addition, the cathode thickness did not decrease. This confirms the findings of the pressure mapping results in Figure 6.2. Due to the low volume expansion of the Si/C-anode, the cathode thickness is not decreased. Even in case of the fixed compression, no reduction of the cathode thickness was observed. Contrariwise, the cathode thickness increased by an average value of +7.5%. Therefore, the reduced volume expansion of the Si/C-anode leads to a less pronounced pressure increase without penetrating the cathodes in the stacks. Regarding the change of the anode thickness and mass in Figure 6.8a and c, another interesting fact is noticed. The thickness and the mass of the calendered and uncalendered anodes cycled in cells under a pressure of 0.42 MPa and 0.84 MPa show almost the same increase. However, the thickness increased less than the mass. This fits together with the assumption that a heavily applied pressure forces the material to expand in the pores, which was confirmed by the porosity measurements presented in Figure 6.5.

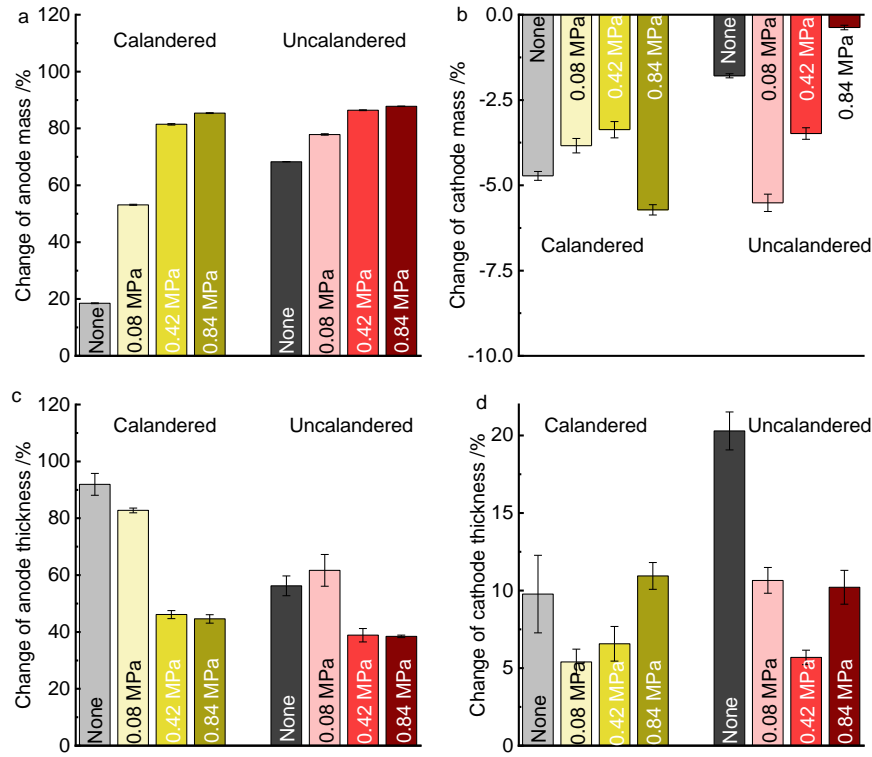


Figure 6.8: Change of the anode and cathode mass (a and b) and thickness (c and d) on basis of the mass and the thickness of the pristine electrodes evaluated from harvested Si/C-anodes and NMC811-cathodes after cycling.

### 6.1.3 Summary of the influence of mechanical pressure

Summarizing, the lifetime of the Si/C|NMC811-cells is prolonged drastically by the application of a mechanical pressure. The highest remaining capacity was achieved for heavily compressed cells with uncalendered anodes. The capacity retention was improved by around 33% compared to cells cycled without compression. In case of a heavily flexible compression, the capacity decreases linearly with a simultaneous increase of the irreversible swelling of the cells. This indicates the repetitive ICL by parasitic reactions at the anode,



which was confirmed by an extensive post-mortem analysis. In addition, it was shown that the calendaring process seems to harm the stability of the C-matrix of the Si/C-composite applied herein. Since this C-matrix should protect the embedded Si-particles from the contact with the electrolyte to prevent SEI growth, the calendaring of the anodes lead to an accelerated capacity fading. However, this was improved significantly by the application of a high enough mechanical pressure. For a pressure of 0.84 MPa, the capacity retention of the cells with calendered anodes was the same as with uncalendered anodes. Figure 6.9 depicts the aging mechanism of the Si/C-anodes in compressed and uncompressed cells schematically.

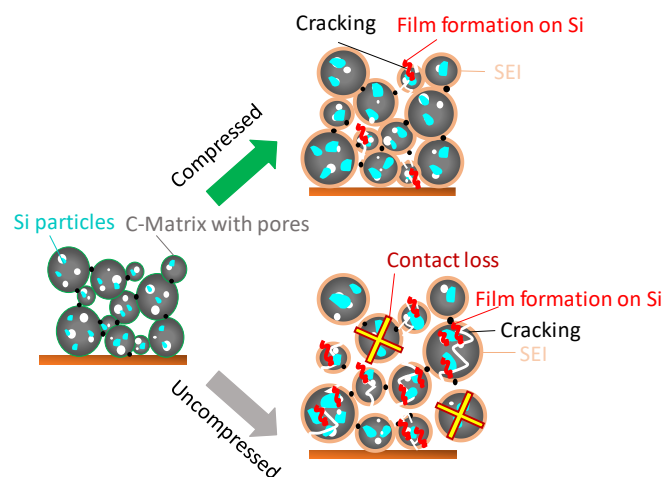


Figure 6.9: Schematic illustration of the aging mechanism of the Si/C-anode in compressed and uncompressed cells.

From the SEM investigation in Figure 6.4, it was noticed that the Si/C-anodes harvested from cells cycled under compression showed much less cracking of the C-matrices compared to the uncompressed ones. It seems that the applied pressure helps to keep the particle structure intact preventing the contact of the Si to the electrolyte. Therefore, the SEI formation was mainly concentrated on the edges of the particles. Contrariwise, the Si/C-anodes showed severe contact loss after the cycling in uncompressed cells. Due to the detachment of some Si/C-particles, other particles are lithiated more. The lithiation of the Si-particles to higher capacities than the dictated 30% lead to fracture of the C-matrix exposing the Si to the electrolyte. This, in turn leads to reactions of the electrolyte at the Si surface under decomposition of the electrolyte and trapping of cycleable Li causing an accelerated capacity fading. These effects were observed in uncompressed cells and in cells cycled at a slightly flexible pressure of 0.08 MPa.

The partial lithiation of the Si combined with the embedded pore volume in the Si/C-composite reduces the expansion of the anode in vertical direction leading to an uniform pressure distribution during the cycling. Therefore, the separator of the cells cycled under fixed compression was not compressed by the swelling of the anode. In contrast to the observations of the C/Si|NMC811-cells in 5.4, the ion mobility in the separator of the cells is maintained even at heavily fixed pressures. The operando conducted expansion measurements revealed that the application of a high pressure leads to a reduced swelling. Cells cycled at

a flexible compression of 0.84 MPa exhibited a total swelling of only 5.6% while 0.08 MPa compressed cells ended up at 13.9% after 150 cycles. The reason for this is the higher utilization of the provided void space in the anode, which was confirmed by post-mortem conducted porosity measurements.

Even though the lifetime of the cells is prolonged with the increase of the pressure, the application of a much higher mechanical pressure on the cell surface is not feasible for two reasons. Firstly, the application of a high mechanical pressure increases the risk of short-cuts through the separator leading to indistinguishable safety risks. Secondly, the application of a higher mechanical pressure is restricted by the technical implementation. When thinking of larger cell formats in automotive applications, the force has to be increased to apply the same pressure on larger cell surfaces. This pressure is limited by the design of the battery module or pack. Commonly, a maximum pressure between 0.05 – 0.5 MPa is utilized in current applications.

## 6.2 Cathode potential shift

Even though, this thesis focuses on the influence of the mechanical pressure on the Si-containing anodes, the cathode aging cannot be neglected completely. As was observed in section 5.2 and 6.1 for the C/Si/NMC811- and Si/C|NMC811-cells, the cathodes evaluated post-mortem showed an extreme ICL initiated by the anode aging. In addition, an unneglectable loss of the specific capacity of NMC811 was determined (see Figure 5.6 b and Figure 6.7). Hence, harvested cathodes from cycled Si/C|NMC811-cells were further investigated employing SEM cross-sectioning. Figure 6.10 shows the SEM cross-sections of a pristine NMC811-cathode in comparison to the cycled one. As can be seen in Figure 6.10 b, the cycled NMC811 particles are completely cracked. According to literature, layered NMC with higher Ni-content suffer from a number of problems as a reduced thermal stability due to the reduction of the highly reactive  $\text{Ni}^{4+}$  to the more stable  $\text{Ni}^{2+}$  under oxygen release.<sup>84,185</sup> Furthermore, cation mixing on the surface of the NMC particles is leading to spinel formation and eventually to the formation of an inactive phase.<sup>13,186</sup> Commonly, the layered oxides consist of submicron primary particles ( $\sim 0.2 \mu\text{m}$ ) which are agglomerated as larger secondary particles ( $\sim 5 \mu\text{m}$ ).<sup>187</sup> Especially for NMC811, cracking along the grain boundaries of the primary particles is a well-known and often described problem.<sup>13,186,187</sup> The large, anisotropic shrinking and expansion of the crystal lattice dimensions of the Ni-rich layered oxides can lead to intergranular cracking of the boundary between the primary particles. The thereby increased surface area causes further active sites for parasitic reactions and the isolation of the newly separated particles can cause a loss of active material and a decreased electrical contact.<sup>93,156,187</sup> Various XRD- studies in literature revealed a correlation of the upper cathode potential or the DOD (depth-of discharge) with the crack formation. Since the crystalline structure gets opened with the removal of Li, the crack formation depends strongly on the degree of delithiation of the layered oxide.<sup>92</sup> Hence, cracks are mostly observable for 100% DOD whereas, almost no cracks occur for a limited operation window of 70% DOD for  $\text{LiNi}_{0.76}\text{Co}_{0.14}\text{Al}_{0.1}\text{O}_2$  (NCA).<sup>13,156</sup> The group of Dahn showed a much higher contraction of the unit cell volume of Ni-rich materials such as

NMC811 than of  $\text{LiNi}_{0.42}\text{Mn}_{0.42}\text{Co}_{0.16}\text{O}_2$  (NMC422) employing in-situ-XRD measurements.<sup>93</sup> According to them, the c lattice parameter of the NMC811 is already increasing for potentials of 4.3 V vs.  $\text{Li/Li}^+$  leading to a normalized unit cell volume change of  $\sim 5.5\%$  while NMC422 only shows a much lower change of  $\sim 2\%$ .<sup>13,93</sup> This severe volume change puts a high inner stress on the material and is likely the reason for the micro cracks.

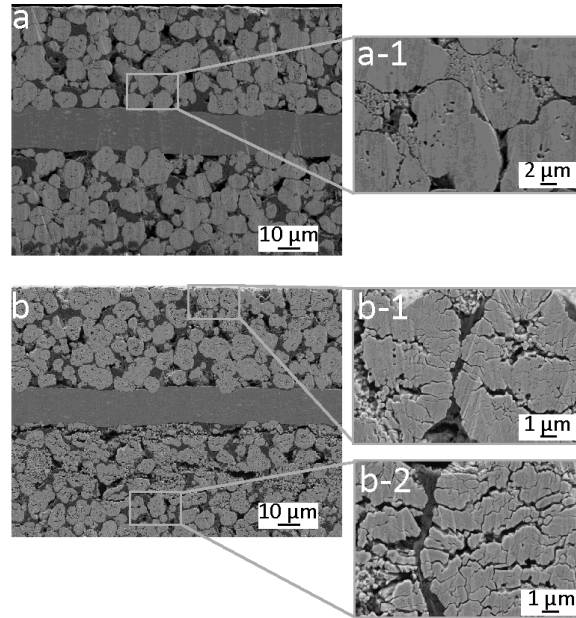


Figure 6.10: SEM cross-sections of a pristine NMC811-cathode (a) and a cycled one harvested after 200 cycles from a Si/C|NMC811-cell (b) in different magnifications.

A schematic illustration of the occurrence of cracks is shown in Figure 6.11.

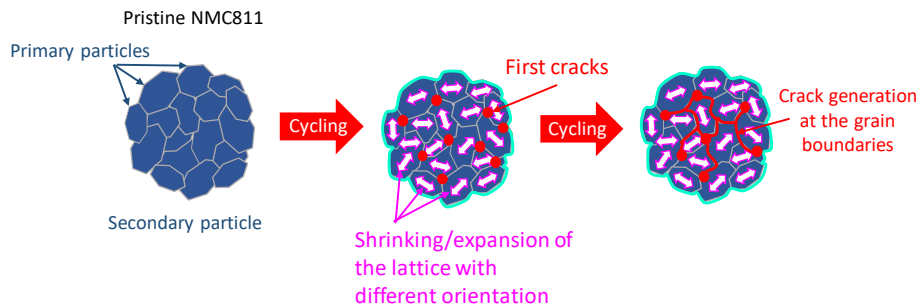


Figure 6.11: Schematic illustration of the cracking of NMC811 particles.

Due to the lattice contraction and expansion of the primary particles with different crystal-line orientation during the cycling, the inner stress is increasing drastically. And the formation of micro cracks is getting more likely at the grain boundaries of the primary particles.<sup>93,187–189</sup> This might also enable the penetration of electrolyte in the particles followed by the formation of  $\text{Li}^+$  isolating layers, i.e.  $\text{NiO}$ -like interface layers, which can cause higher impedance as well as the loss of electrical contact resulting in the loss of NMC active material.<sup>93,188,190</sup>

The question remains why crack forming is observed in the NMC811-cathodes cycled herein, although the full cell voltage is controlled to an upper limit of 4.2 V. Therefore,

reference cells with Si/C-anodes and NMC811-cathodes were assembled and cycled (see section 3.2.2). Figure 6.12a and b give the anode, the cathode, and the full cell potential during the initial cycle. Subsequent cycles and the extracted upper cut off potential of the cathode during the cycling are shown in Figure 6.12c and d. As a comparison, reference cells consisting of graphite-anodes and NMC811-cathodes were cycled. The upper cut off potential of the NMC811-cathode cycled versus a graphite-anode is shown in Figure 6.12d.

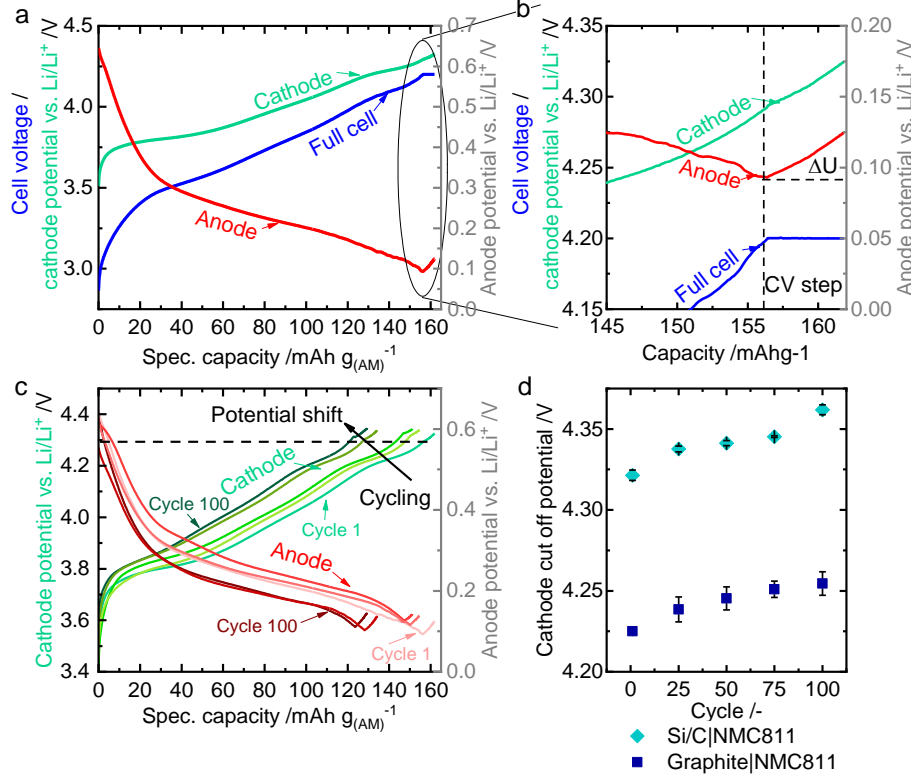


Figure 6.12: Reference cell measurements of a Si/C|NMC811-cell with Li-metal reference. Charge potential of the cathode, the full cell, and the anode during the first cycle (a and b) and for selected cycles from cycle 1 to 100 (c). (d) Extracted cathode cut off potential of the Si/C|NMC811-cells in comparison to graphite|NMC811-cells over cycles.

It is observable that the anode potential is increasing as soon as the constant voltage step starts (see Figure 6.12b). This relaxation effect is increasing with the number of cycles (see Figure 6.12 c and d) causing the shift of the cathode potential to higher values of up to 4.37 V after 100 cycles. Hence, it seems that the delithiation potential of the cathode is shifted to higher potentials due to the increasing overpotential of the Si/C-anode. At the same time, the upper cut off potential of the NMC811-cathode measured in the graphite|NMC811-cells approaches a value of only 4.25 V after 100 cycles. These results show the importance of controlling the potential window of full cells consisting of Si/C-anodes and Ni-rich cathodes. Reuter et al. concluded the same effects.<sup>191</sup> During their study of the influence of the balancing of NMC811|Si-cells, they found an accelerated degradation of the cathode due to overcharging caused by a higher end of charging potential of the Si-anode, which was not fully utilized.<sup>191</sup> Beattie et al. investigated the anode potential shift by a three electrode setup confirming the results presented herein.<sup>41</sup> Due to the ICL, less Li can be lithiated to the anode. This leads to a rise of the end of charge voltage increasing the

upper cathode voltage. Therefore, new Li is liberated from the cathode to be lithiated to the anode. However, this leads to an accelerated capacity fading caused by cracking of the NMC811-particles. According to the reference cell measurements shown in Figure 6.12, it is necessary to limit the full cell voltage to 4.05 V to keep the cathode potential below 4.25 V. Hence, to evaluate the influence of the accelerated NMC811 aging on the cycling behavior of the Si/C|NMC811-cells, cells were cycled with an upper voltage limit of 4.05 V and compared to the results gained with a cut off limit of 4.2 V. Figure 6.13 shows the resulting specific capacity and swelling over 200 cycles.

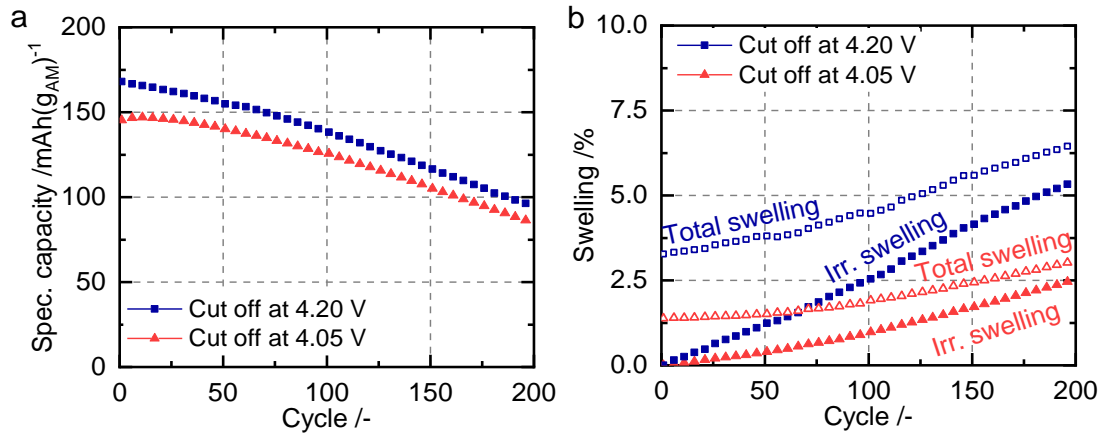


Figure 6.13: Specific capacity (a) and swelling (b) of Si/C|NMC811-cells cycled under 0.84 MPa flexible compression with an upper cut off potential of 4.2 V compared to 4.05 V.

As can be expected, the specific capacity is reduced by decreasing the upper cut off limit of the full cell to 4.05 V (see Figure 6.13a red curve). The specific capacity is reduced from 168.0 mAh (g<sub>AM</sub>)<sup>-1</sup> to 145.2 mAh (g<sub>AM</sub>)<sup>-1</sup>. Due to less Li delithiated from the cathode and lithiated in the anode during the charging, the total swelling is reduced (see Figure 6.13b). Furthermore, the irreversible swelling is reduced indicating a lower ICL trapped in the Si/C-anode. However, the capacity fading over 200 cycles is almost the same independently of the cut off potential. The cells with a cut off potential of 4.2 V and 4.05 V show a remaining capacity of 57.3% and 58.2%, respectively. Therefore, it seems that the reduction of the upper cut off potential influences the lifetime of the cells only insignificantly. The aging of the Si/C-anode seems to be the key driver for the aging of the full cells. At the same time, the reduction of the upper cut off potential decreases the volumetric energy density of the cells substantially from 450.5 Wh L<sup>-1</sup> to 398.7 Wh L<sup>-1</sup>.

### 6.3 Upscaling to PHEV1 cell format

Due to the fact, that the cell geometry has a major influence on the aging mechanisms in nowadays LiB applications, PHEV1 cells are assembled consisting of Si/C-anodes and NMC811-cathodes. Since the uncalendered anodes performed better than the calendered ones, uncalendered Si/C-anodes were utilized in the PHEV1 cells. Furthermore, the jelly roll of the cells was dimensioned as large as possible to fit into the housing while providing a well distributed contact of the layers. To evaluate the cycling results of the PHEV1 cells



under different pressure, the cells were cycled in a fixed and a flexible compression employing operando pressure and expansion measurements (see setup in Figure 3.10). The applied pressure was set to 0.1 MPa. In addition, cells were cycled uncompressed conducting operando expansion measurements.

Figure 6.14a and b show an exemplary pressure and expansion measurement during the cycling of the PHEV1 cells under fixed and flexible compression. In the fixed pressure configuration in Figure 6.14a, the pressure is increasing repetitively during the charging starting at the initially applied value of 0.1 MPa. Its value increases to 0.216 MPa and decreases during the discharging again. During these first 16 cycles, the pressure increases irreversibly only to 0.103 MPa. The same behavior can be observed for the expansion of the PHEV1 cell in the flexible pressure configuration in Figure 6.14b. As the pressure is hold constant by springs, the cell is able to expand by a maximum value of 1.84 mm during the charge. The cell shows an irreversible thickness increase of 0.21 mm in the discharged state during these first 16 cycles.

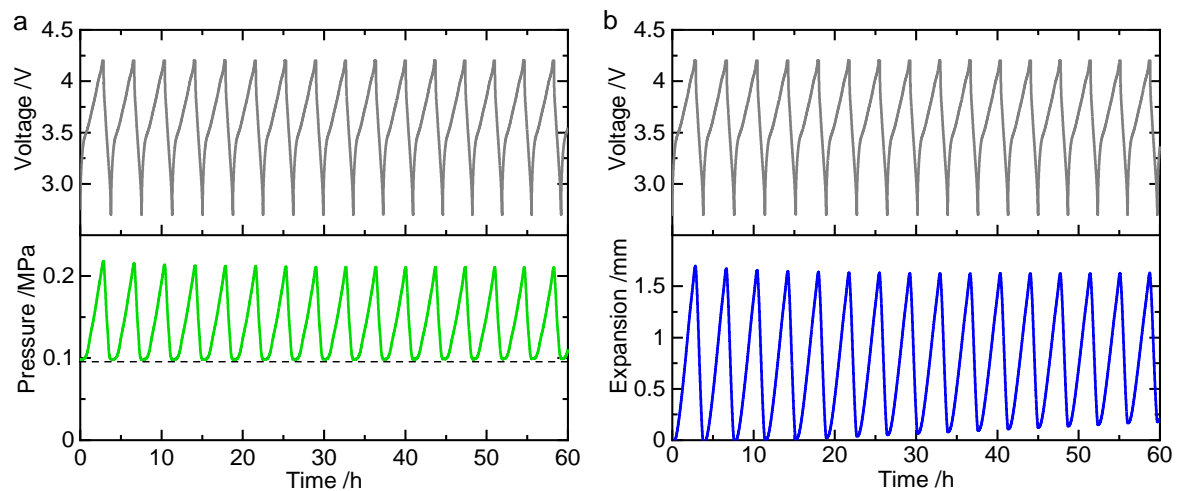


Figure 6.14: Exemplary pressure (a) and expansion (b) of Si/C|NMC811-PHEV1 cells cycled at a pressure of 0.1 MPa. Reused in parts.<sup>124</sup> ©2020 Wiley.

Figure 6.15 shows the cycling results of the PHEV1 cells without and under fixed as well as flexible compression during 100 cycles. As can be seen in Figure 6.15a, b, and c, the uncompressed PHEV1 cells show the worst performance with the lowest Coulombic efficiency, an accelerated capacity fading, and a significant increase of the CV charge capacity. Compared to the swelling and pressure behavior of the compressed PHEV1 cell, the uncompressed cells exhibit a much higher irreversible swelling (see Figure 6.15d). While the irreversible swelling of the flexibly compressed cell increases linearly with the number of cycles, the irreversible swelling of the uncompressed cells rises significantly during the initial 20 cycles and flattens afterwards. Generally, the irreversible swelling, the reversible swelling, and the total swelling of the uncompressed cells (pink) is almost twice as high as of the flexibly compressed one (blue). This proves that the housing of a prismatic cell is not enough to counteract the expansion of Si-containing anodes.

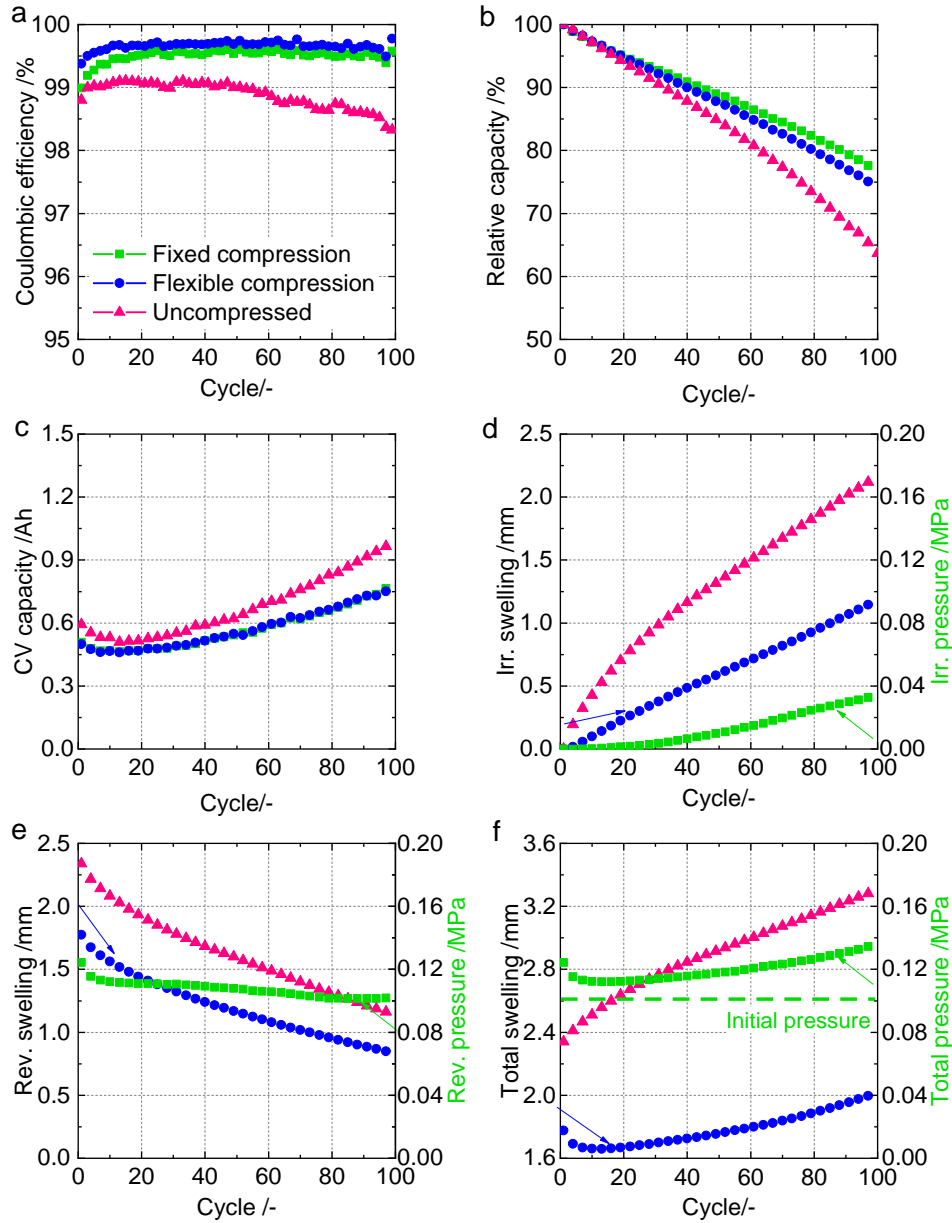


Figure 6.15: Coulombic efficiency (a), discharge capacity (b), CV capacity (c), irreversible swelling and irreversible pressure (d), reversible swelling and reversible pressure (e), and total swelling and total pressure (f) of PHEV1 cells without compression and under flexible and fixed compression.

These results perfectly match the pouch cell results discussed above. It seems that the housing of the PHEV1 cell cannot keep a high enough compression on the electrode layers to prevent contact loss causing an accelerated capacity fading. Regarding the PHEV1 cells under fixed and flexible compression, the cycling results show a similar trend. The capacity of the cells under fixed and under flexible compression decreased to 77.2% and 74.5%, respectively. The capacity of the CV step shows a completely overlapping rise (see Figure 6.15c). Both, the irreversible swelling and the irreversible pressure, increase almost linearly with the number of cycles. Whereas, the rise of the irreversible pressure is delayed to cycle number 30. In terms of the reversible and the total pressure and swelling, similar trends are noticed. Generally, the reversible swelling and the reversible pressure show a decreasing slope. However, the values are dropping with a higher gradient during the initial 10 cycles.



The same accounts for the total swelling and the total pressure, which sums up the contributions from the irreversible and reversible swelling/pressure. During the very first 10 cycles, both, the total swelling and the total pressure, are decreasing before they are rising again.

To understand these nonlinear trends of the reversible swelling/pressure, X-ray computer tomography (CT) measurements of the PHEV1 cells were conducted. Figure 6.16 shows the CT cross-sections through the jelly rolls of a pristine PHEV1 cell (before the electrolyte filling), a cell after the formation, a cell after 100 cycles under compression, and a cell after 100 cycles without compression.

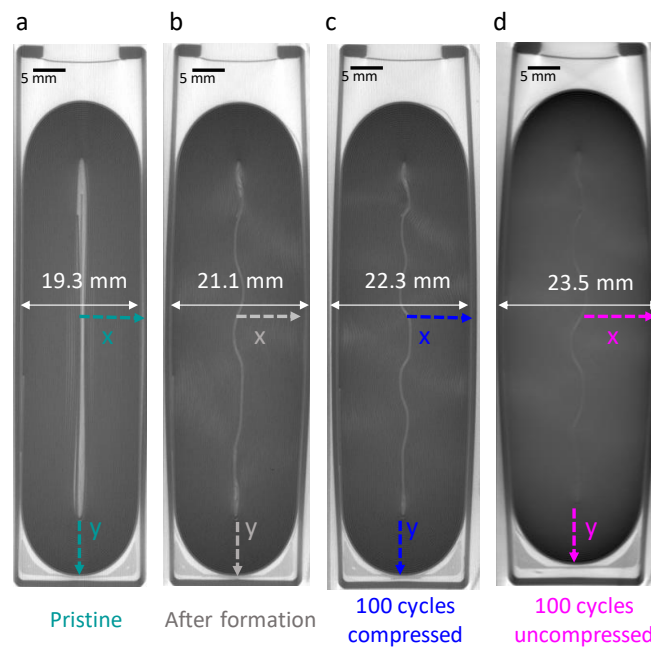


Figure 6.16: X-ray CT images of a pristine PHEV1 cell (a) and PHEV1 cells after the formation (b), after 100 cycles under a pressure of 0.1 MPa (c), as well as without pressure (d). The x- and the y-direction of the jelly roll as well as their thicknesses are marked. Reused in parts.<sup>124</sup> ©2020 Wiley.

The thickness of the jelly roll increased drastically after the formation due to the wetting of the electrodes with the electrolyte and the initial volume expansion of the anode (compare Figure 6.16a and b). The void space inside of the jelly roll is filled and a small corrugation is visible. After the cycling under compression in Figure 6.16c, the thickness of the jelly roll increased by 1.2 mm and the inner corrugation increased slightly. This effect is much more dominant in case of the cell cycled without a compression in Figure 6.16d. The thickness increased by 2.4 mm. This is twice the value of the compressed PHEV1 cell, which is in very good agreement with the expansion measurements in Figure 6.15c indicating a doubled swelling of the uncompressed cells.

Because differences in the CT images are hardly visible with the eye, the intensity of the pixels in the images was evaluated utilizing OriginLab. The evaluation was conducted along the x- and y-axis displaying the two different regions of the jelly roll. Figure 6.17 shows the intensity along the x- and the y-axis for the four CT images.

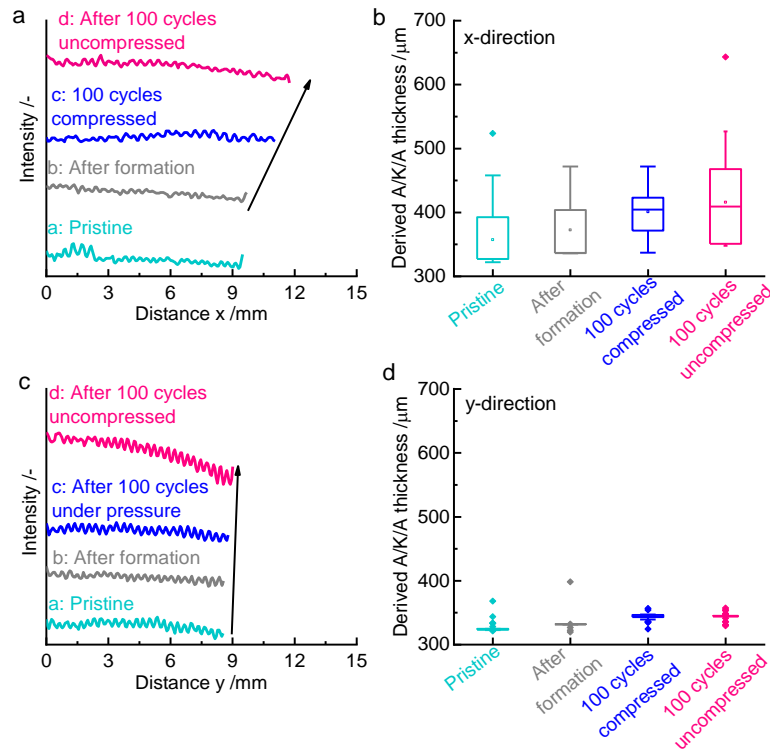


Figure 6.17: Evaluation of the pixel intensity and derivation of the distance of the Cu current collectors representing the thickness of one A/K/A-unit cell along the x-axis (a and b) and along the y-axis (c and d). Reused in parts.<sup>124</sup> ©2020 Wiley.

The x-direction marks the behavior of one-half of the jelly roll at its longest edge where the most deformation is possible. Contrarily, the y-direction represents the curved region of the half jelly roll where a high tensile stress holds the layers in position (see positions in Figure 6.16). Since the Cu current collector foils of the anodes have a high density of  $8.9 \text{ g cm}^{-3}$  compared to the other materials, the Cu foils appear very dark on the CT images. The intermediate layers consisting of the anode coating, the separator, the cathode, the second separator, and the second anode coating appear lighter in the images and will be referred to as A/K/A-unit cell. Based on that information, the Cu foil is represented as minima with a low intensity in the line scans provided in Figure 6.17a and c. Hence, the thickness of such an A/K/A-unit cell can be determined and is presented in Figure 6.17b and d. The actual thickness of an A/K/A-unit cell in the pristine state is  $316 \text{ μm}$ .

Regarding the intensity of the pristine jelly roll in x-direction in Figure 6.17a, the void space between the inner layers gets obvious by high peaks and an inhomogeneous distribution. After the formation, the void spaces are closed and the layers are distributed more uniform. The half jelly roll thickness did not increase. However, the average A/K/A-thickness in x-direction increased from  $355.9 \pm 100.7 \text{ μm}$  to  $374.1 \pm 67.8 \text{ μm}$  while the standard deviation decreased (see Figure 6.17b). This indicates an irreversible increase of the anode thickness during the formation filling up the void spaces in x-direction. In y-direction, the curvature holds a high tensile stress on the layers and the thickness of the A/K/A-unit cells increases only slightly from  $327.1 \pm 23.4 \text{ μm}$  to  $331.7 \pm 22.9 \text{ μm}$  (see Figure 6.17c and d).

The determined value for the A/K/A-thickness of the pristine jelly roll is very close to the effective thickness of 316  $\mu\text{m}$ .

After the cycling under compression, the inner corrugation increased and the jelly roll expanded to a total thickness of 22.3 mm. However, the layer distribution in y-direction stayed constant during the cycling (see Figure 6.17c). The thickness of the half jelly roll in y-direction reached a value of 8.78 mm which is only marginally more than the thickness after the formation of 8.56 mm. In addition, the average A/K/A-thickness increased only to  $343.8 \pm 16.1 \mu\text{m}$  remaining a very low standard deviation. The high pressure in the curved region counteracts the thickness increase of the Si/C-anode. Compared to the A/K/A-thickness in y-direction after the formation, this means an irreversible thickness increase of only 3.6%. Regarding the layers in x-direction, the layers are still distributed homogeneously even though the A/K/A-thickness increased to  $400.8 \pm 67.7 \mu\text{m}$  during the cycling under compression (see Figure 6.17a and b). This means an irreversible thickness increase of around 6.9% of the A/K/A-unit cells in x-direction, which is almost twice the value compared to the y-direction. The thickness increase in x-direction agrees well with the irreversible swelling determined by the operando expansion measurement (see Figure 6.15).

Contrariwise, the PHEV1 cell cycled uncompressed shows a more inhomogeneous distribution of the electrode layers in the x-direction. Furthermore, some lighter regions can be seen in the CT-image (see Figure 6.16c). These regions can be interpreted as regions with void space between the layers. This is outpointed by higher peaks in the intensity along the x-axis in Figure 6.17a. The layers are especially uneven distributed in the middle regions of the half jelly roll at a distance  $x$  of 2 – 3 mm. However, these regions are not uniformly distributed in the jelly roll and are most likely caused by the increased inner corrugations and the high tensile stress inside the jelly roll. The average A/K/A-thickness increased to 415.7  $\mu\text{m}$  in the cycled cell without compression, which is equal to an irreversible thickness increase of 11.1%. The maximum value reaches 643.0  $\mu\text{m}$  and a minimum value of 347.0  $\mu\text{m}$  is determined. This shows the tendency to layer detachments and contact loss when cycled without compression. Still, in y-direction no change of the total and the A/K/A-thickness can be observed. The irreversible thickness increase in the y-direction is only 3.7%. This indicates the strong deformation of the jelly roll in x- and y-direction resulting in an uneven utilization of the jelly roll in prismatic cells. The lower utilization of the active material in the curved regions of the jelly roll is a known problem and was evaluated by several groups e.g. by X-ray diffraction radiography,<sup>192</sup> by EIS measurements of harvested electrodes from prismatic cells,<sup>193</sup> and by simulation of the pressure distribution in the jelly roll.<sup>194</sup> Here, the layer detachments and the high deformation explain the higher capacity fading of the uncompressed PHEV1 cells observed in Figure 6.15. This highlights the necessity of a mechanical compression to keep the contact of the electrode layers in prismatic cells containing Si/C-anodes.

Finally, the performance and the expansion of the compressed PHEV1 cells are compared to the pouch cells cycled at a comparable compression. Figure 6.18 shows the Coulombic

efficiency, the remaining capacity, the relative CV charge capacity as well as the irreversible, the reversible, and the total swelling of the Si/C|NMC811 pouch cell (red) and the Si/C|NMC811 PHEV1 cell (blue).

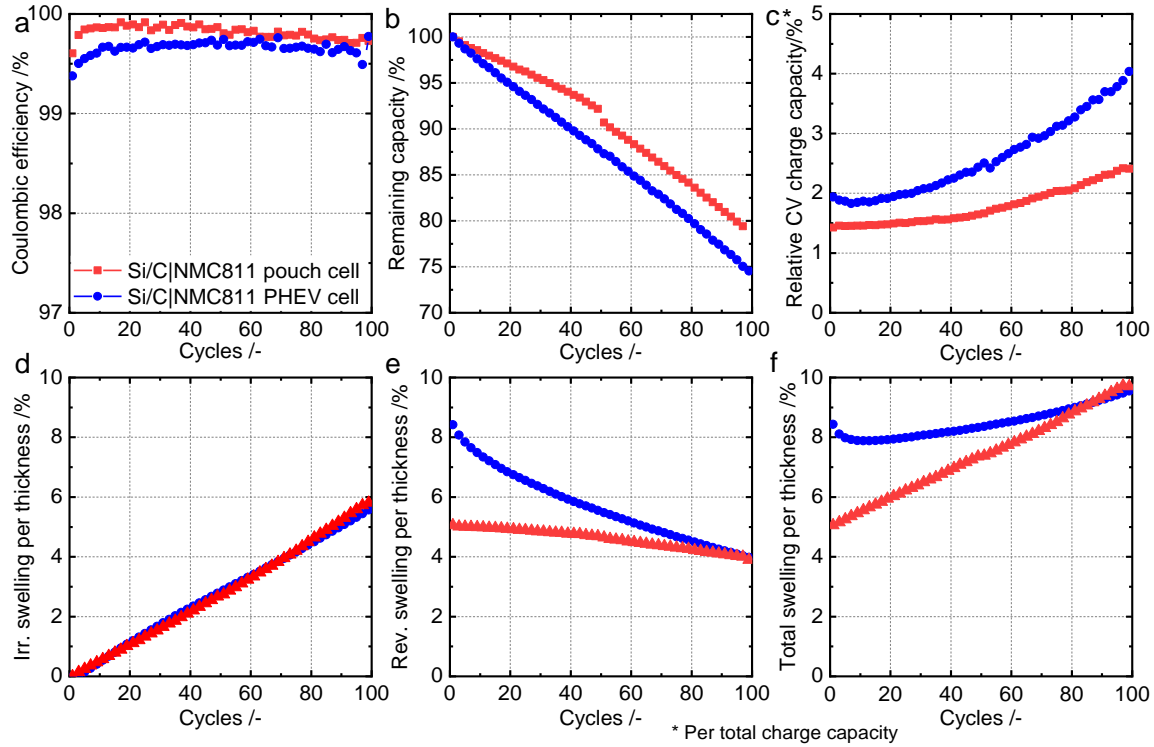


Figure 6.18: Comparison of the performance and the expansion of a Si/C|NMC811 pouch and PHEV1 cell. Coulombic efficiency (a), remaining discharge capacity (b), relative CV charge capacity (c), irreversible swelling (d), reversible swelling (e), and total swelling (f) over 100 cycles at comparable pressure conditions. Reused in parts.<sup>124</sup> ©2020 Wiley.

For a better comparability, the irreversible, the reversible, and the total swelling are shown as the ratio of the expansion and the initial thickness of the electrode stack and the jelly roll, respectively. A slightly decreased performance of the PHEV1 cells compared to the pouch cells in terms of the Coulombic efficiency, the remaining capacity, and the CV charge capacity is observed (see Figure 6.18a, b, and c). After 100 cycles, the PHEV1 cell shows a remaining capacity of 74.5% while the pouch cells demonstrate a higher value of 79.2%. In addition, the CV capacity rises to around 4.0% whereas the pouch cell's CV charge capacity rises only to 2.4%. Summarizing, the PHEV1 cells experience a somewhat accelerated aging. The reason for this is evident and was confirmed by the CT evaluations in Figure 6.16 and Figure 6.17. The inhomogeneous pressure distribution causes an unequal utilization of the active material reducing the available capacity in the PHEV1 cell.<sup>192–194</sup> State of health and current density simulation proved this inhomogeneous utilization in cylindrical and prismatic cell designs.<sup>195</sup> On the contrary in the pouch cell, the pressure is distributed very uniform, which was proven by the pressure mapping results in Figure 6.2 in section 6.1.1. However, the capacity fading differs only by 4.3%, which is relatively small especially when comparing to the uncompressed PHEV1 cells with a remaining capacity of only 63.7% after 100 cycles (see Figure 6.1).

Having a closer look on the expansion measurements of the pouch and PHEV1 cells in Figure 6.18d, e, and f, it gets obvious that the irreversible swelling of both, the pouch and the PHEV1 cell, is completely overlapping. Therefore, it seems that the irreversible thickness increase of the anode is mostly caused by film formation reactions in the anode and is independent of the cell geometry. Figure 6.19a and b show a schematic illustration of the irreversible thickness increase of the PHEV1 cell after the formation and during the subsequent cycling. The anode thickness is increasing drastically due to the film formation reactions, the trapping of cycleable Li as well as the deposition of electrolyte decomposition products. Even though the jelly roll starts to corrugate, the increase of the irreversible thickness is dominated by this thickness increase of the anode. This is confirmed by the evaluated A/K/A-thickness in x-direction of the CT images (see Figure 6.17), which increased by 6.9% and agrees well with the irreversible swelling determined outside of the cell housing (see Figure 6.18d). Hence, the irreversible expansion of the jelly roll in x-direction can be compared to that of a stacked electrode configuration and is influenced primarily by the irreversible thickness increase of the Si/C-anode.

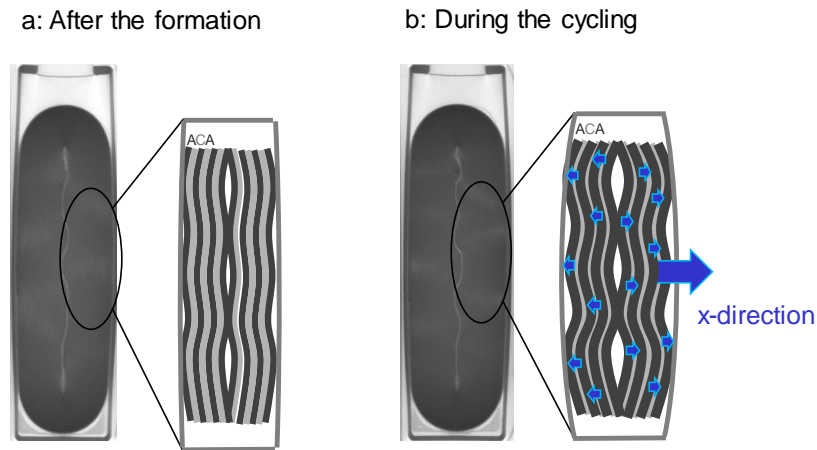


Figure 6.19: Schematic illustration of the irreversible swelling in x-direction of the PHEV1 cells after the formation (a) and during the subsequent cycling (b).

Regarding the reversible and the total swelling of the PHEV and the pouch cell, a significant difference can be observed (see Figure 6.18e and f). The pouch cells exhibit an almost linear decrease of the reversible swelling correlated with the ICL at a gradient of -0.011% per cycle. Contrarily, the reversible swelling of the PHEV1 cells decreases with a high gradient of -0.136% per cycle during the initial 20 cycles. Afterwards, the gradient is reduced to -0.039% per cycle. Generally, the reversible swelling of the PHEV1 cell is higher compared to the pouch cell. This behavior can be explained by a simple schematic illustration presented in Figure 6.20a. The geometry of the PHEV1 cell provokes regions with different ability for movement of the jelly roll. In the middle of the housing, the layers are held by the lowest mechanical resistance. The deformation of the jelly roll in x-direction is preferred and was around twice as high as in the y-direction (see Figure 6.17). Caused by the geometry of the cell housing and the curvature in y-direction, the jelly roll is put under a high tensile stress. Therefore, the expansion of the jelly roll is amplified in the x-direction where it is able to expand. Contrariwise, the electrodes in an electrode stack in the pouch

cells can expand uniformly (Figure 6.20b). Therefore, the observed expansion is lower than in the PHEV1 cell.

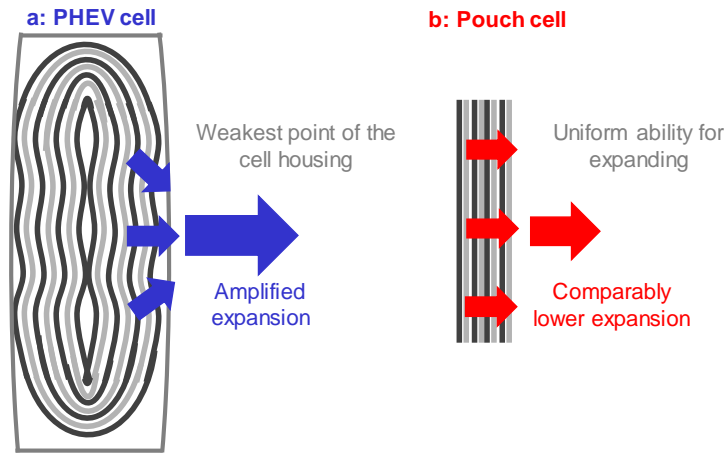


Figure 6.20: Schematic illustration of the higher reversible swelling of a PHEV1 cell (a) in comparison to a pouch cell (b).

The question remains why the gradient of the reversible swelling of the PHEV1 cell is changing after around 20 cycles. Unfortunately, there is no literature on the expansion and the mechanical deformation of Si-containing PHEV1 cells available as comparison. However, the phenomenon can be explained by a closer evaluation of the CT-images. Figure 6.21a and b show CT images of the PHEV1 cell after the formation and after the cycling under compression. Inside of the jelly rolls, the corrugation is marked in blue.

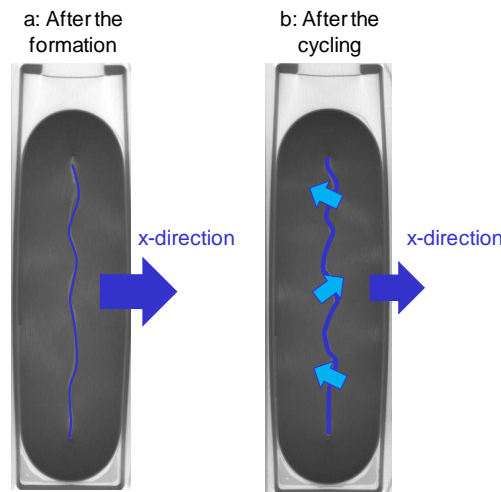


Figure 6.21: Schematic illustration of the mechanical deformation inside of the jelly roll after the formation (a) and after the cycling (b).

As can be seen, the corrugation is less after the formation when the cell shows a high reversible swelling. After around 20 cycles, the amplitude of the reversible swelling is smaller and decreases with a lower gradient than before (see Figure 6.18e). The reason for this is illustrated in Figure 6.21b. Due to the increased inner corrugation during the cycling, the jelly roll is mechanically deformed in different direction. This deformation is reducing the measurable expansion of the cell outside of the housing explaining the reduced reversible swelling in Figure 6.18e. Similar results were observed by Liu et al. who investigated the

stress generation in rolled anodes concluding that a higher swelling can be observed during the initial cycles and is slowing down afterwards.<sup>196</sup>

Summarizing, the application of a mechanical pressure on Si/C|NMC811 PHEV1 cells improves the performance significantly. The reason for this is the highly improved contact of the layers in the jelly roll, which was confirmed by X-ray CT evaluations. Furthermore, the compressed PHEV1 cells show only a slightly decreased capacity compared to the compressed pouch cells. This is caused by a lower active material utilization due to the cell geometry. However, the underlying aging mechanism of the Si/C-anode resulting in an irreversible swelling stays the same as in the pouch cell independently of the geometry. The higher reversible swelling observed for the PHEV1 cells can be explained by the amplification of the expansion at the weakest point of the cell housing. In addition, the nonlinear behavior of the reversible swelling with an increased gradient during the first 20 cycles and a subsequent lowering is provoked by an increasing mechanical deformation inside of the jelly roll during the cycling.



## 7 Comparison of the effects of mechanical pressure on Si-containing Li-ion cells

To summarize this work, this section highlights the performance of the variously compressed pouch cells containing Si anodes and Ni-rich cathodes with regards to today's requirements for next generation LiBs. As mentioned in the introduction, the largest challenges, which need to be overcome to enable the extensive application of LiBs, are the increase of the volumetric energy density, the increase of the C-rate capability, and the enlargement of the lifetime. Additionally, the safety of the LiBs plays a major role. Firstly, the differently compressed C/Si|NMC811- and Si/C|NMC811-cells will be compared by means of their volumetric energy density and lifetime in section 7.1. Secondly, the main difference of the behavior of both, the C/Si- and the Si/C-anodes, will be discussed in section 7.2. Thirdly, the C-rate capability will be investigated in section 7.3 before all contributions are summarized and compared taking into account the volumetric energy density, the lifetime, the C-rate capability, and the safety of the tested cells in section 7.4.

### 7.1 Volumetric energy density and lifetime

Figure 7.1 shows the volumetric energy density of the C/Si|NMC811- and the Si/C|NMC811-cells with calendared and uncalendered Si/C-anodes at different fixed and flexible pressures as well as uncompressed. The volumetric energy density is not only taking into account the capacity of the cells during the cycling, but also the operando measured total thickness increase of the electrode stack in the cells.

Since the soft case pouch cells analyzed herein naturally vary in their overall volume, the volumetric energy density is referred to a more reproducible parameter, i.e. the stack volume. Since the cycling capacity of the cells depends strongly on the applied pressure, all cells were cycled at the same current according to their theoretic capacity of the active material. Hence, the volumetric energy density is plotted versus the cumulated charge throughput enabling a better comparability. As a baseline, the volumetric energy density for graphite|NMC811-cells is marked with a black dashed line starting from an initial value of  $439.7 \text{ Wh L}^{-1}$ . At the same time, the graphite|NMC622-cells exhibited an initial volumetric energy density of only  $389.5 \text{ Wh L}^{-1}$ . As stated in the introduction in section 1, the state-of-the-art achieved volumetric energy densities vary between  $250 - 450 \text{ Wh L}^{-1}$  for pouch cells targeting  $800 \text{ Wh L}^{-1}$  in 2025 and  $> 1000 \text{ Wh L}^{-1}$  in 2030.<sup>2,7</sup>

To provide a better clarity of the data, the volumetric energy density of the first cycle (initial) and of the 100<sup>th</sup> cycle is shown in Figure 7.2 for the differently compressed cells consisting of the C/Si|NMC811- and the Si/C|NMC811-electrodes.

From Figure 7.1 and Figure 7.2, it becomes obvious that the C/Si-anode provides the highest volumetric energy density of  $563.1 \text{ Wh L}^{-1}$  on cell level at the start of the cycling exceeding today's standards by more than  $100 \text{ Wh L}^{-1}$ .<sup>2</sup> In addition, it has to be noted that the electrodes utilized herein are not optimized with regards on their volume i.e. the thickness of the current collector foils and the separator. The materials are in the range, which is

typically used for test pouch cells but still have potential to be minimized for application purposes enabling a further increase of the volumetric energy density. The lifetime of the C/Si|NMC811-cells suffers from a large volume expansion. Depending on the type and the strength of the mechanical compression, the volumetric energy density of the C/Si|NMC811-cells decreases drastically after 100 cycles exhibiting a maximum remaining volumetric energy density of  $242.1 \text{ Wh L}^{-1}$  for the 0.08 MPa fixed compression. The lifetime decreases with the increase of the pressure in both, the flexible and the fixed configuration. Hence, the best performance in terms of the volumetric energy density in the 1<sup>st</sup> and the 100<sup>th</sup> cycle is achieved with a slightly fixed compression (0.08 MPa) for the C/Si|NMC811-cells.

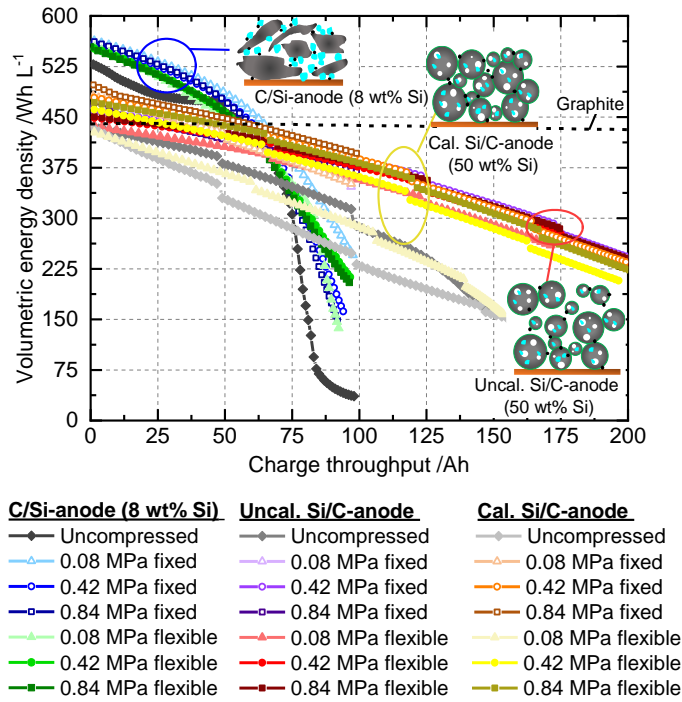


Figure 7.1: Volumetric energy density over cumulative charge throughput of the C/Si-anode, the uncalendered Si/C-anode, and the calendered Si/C-anode during the cycling in stacked pouch cells paired with a NMC811-cathode under different compression configurations. The volumetric energy density of graphite|NMC811-cells is shown as a baseline (black dashed).

The Si/C|NMC811-cells show a different behavior. Their volumetric energy densities start at lower initial values of around  $489.1 \text{ Wh L}^{-1}$  but exhibit a much lower reduction and a prolonged lifetime (see Figure 7.1 and Figure 7.2). This is due to the lower volume expansion and a lower capacity fading. The best results regarding the volumetric energy density and the lifetime are achieved with an increased pressure in the fixed configuration. Of course, when keeping the stack thickness constant in the fixed configuration, the volumetric energy density is increased compared to the flexible configuration. The same accounts for the calendered and uncalendered anodes. With an increased density on electrode level for the calendered anode, the volumetric energy rises. However, as was discussed in section 6.1, the lifetime of the cells with calendered anodes suffered from fractures and cracking of the complex C-matrix of the Si/C-composite. Nevertheless, with increasing the mechanical pressure on the cell, this negative influence could be reduced and the lifetime of the

cells is enhanced. Therefore, the best result regarding the volumetric energy density and the lifetime of the Si/C|NMC811-cells is achieved with calendered anodes and a heavily fixed compression of 0.84 MPa exhibiting a remaining volumetric energy density of  $396.2 \text{ Wh L}^{-1}$  after 100 cycles. However, it has to be noted that such a high pressure might be technically unfeasible to apply on system level in a battery pack. The uncompressed cells with both, the Si/C|NMC811 and the C/Si|NMC811 material, show a drastically accelerated capacity fading. Regarding the uncompressed C/Si|NMC811-cells, the non-linear aging effect discussed in section 5.3 can be observed in the curve in Figure 7.1.

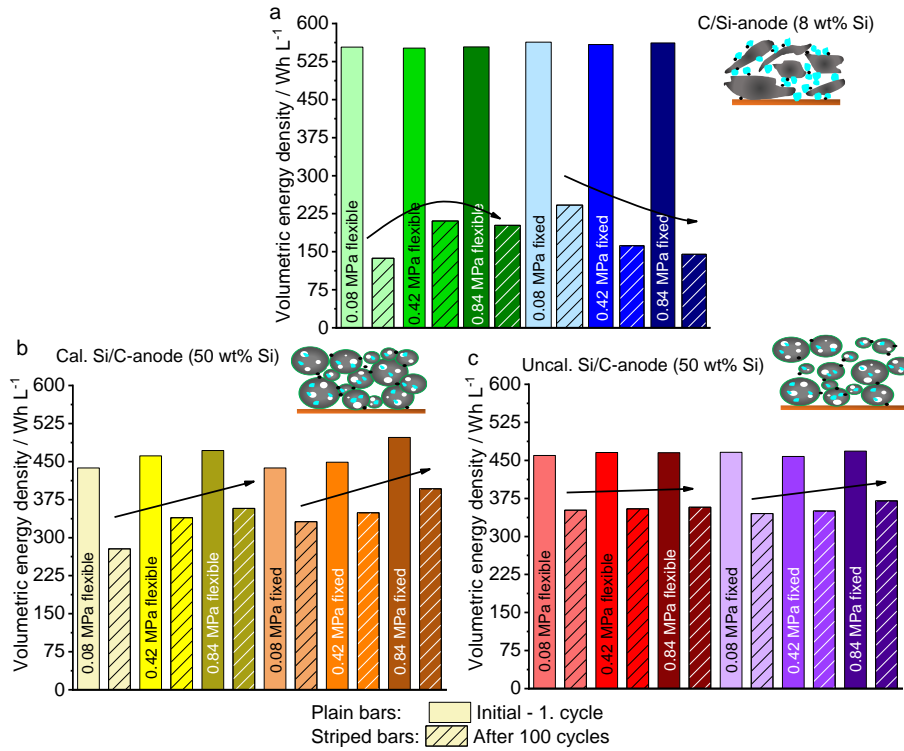


Figure 7.2: Initial volumetric capacity (plain bars) compared to the volumetric capacity after 100 cycles (striped bars) for the stacked pouch cells with C/Si-anodes (a), with calendered Si/C-anodes (b), and with uncalendered Si/C-anodes for different compression configurations.

Both, the Si/C|NMC811- and the C/Si|NMC811-cells, exceed the volumetric energy density of the investigated graphite baseline and the reported values from Fraunhofer ISI of  $250 - 450 \text{ Wh L}^{-1}$  for today's pouch cells during their initial cycles. However, the high capacity fading combined with the volume expansion of the Si-containing anodes leads to a reversed trend after a capacity throughput of around 75 Ah or around 50 cycles and drops below the pure graphite-baseline in terms of volumetric energy density and lifetime (see Figure 7.1). From the evaluation of the volumetric energy density in Figure 7.1 and Figure 7.2, it can be concluded that the C/Si|NMC811-cells at a 0.08 MPa fixed pressure and the Si/C|NMC811-cells with calendered anodes at a 0.84 MPa fixed pressure performs best in terms of the cycle life. The most important performance parameters of these both cell groups is shown in Table 7.1. Here, for comparison purposes of both cell types, the initial volumetric energy density at the begin of life (BOL) and the energy density at a capacity retention of 80%, defined as the end of life (EOL) and after 100 cycles are listed. Furthermore, the initial capacity as well as the volume of the two cells is shown at the BOL. Since

the cells are cycled in a fixed compression, the volume is not changed during the cycling. In addition, the cycle number and the charge throughput at a capacity retention of 80% (EOL) is included in the table. A capacity retention of 80% is a standard EOL criteria for the characterization of LiBs in automotive applications. The capacity retention is calculated from the ratio of the capacity of each cycle divided by the capacity of the cells in the first discharge at 1C. The accelerated aging of the C/Si|NMC811-cells becomes more pronounced compared to the Si/C|NMC811-cells regarding the number of cycles and the charge throughput until reaching the EOL criteria of 80% capacity. Due to their lower volume caused by the higher density of the C/Si-anode on electrode level, the C/Si|NMC811-cells provide a superior initial capacity of  $563.1 \text{ Wh L}^{-1}$  compared to  $497.6 \text{ Wh L}^{-1}$  of the Si/C|NMC811-cells with a lower density and therefore a higher stack volume. Even though the C/Si|NMC811-cells provide a higher initial volumetric energy density than the Si/C|NMC811-cells, the EOL of 80% capacity is already reached after 49 cycles and 60.4 Ah in case of the former but after 96 cycles and 116.5 Ah for the latter. As discussed in section 5, the C/Si|NMC811-cells suffer from the high volume expansion of the C/Si-anode caused by the full utilization of the containing Si. Although the cells are cycled in a fixed pressure configuration, preventing the cell to expand, the C/Si-anodes exhibit a volume expansion compressing the cathode and the separator (see section 5.2). This causes a higher aging rate than the Si/C|NMC811-cells, whose anode capacity is only utilized partially decreasing the volume expansion drastically (see section 6.1.1). With the data from the cycling results in Figure 5.1 and Figure 6.1, the capacity loss per cycle can be calculated. The C/Si|NMC811-cells exhibit a capacity loss of 6.01% per cycle, while the Si/C|NMC811-cells lose only 2.74% of their capacity in each cycle. This explains why the C/Si|NMC811-cells reach the EOL criteria much earlier compared to the Si/C|NMC811-cells.

*Table 7.1: Performance data of the C/Si|NMC811-cells at a 0.08 MPa fixed pressure and the Si/C|NMC811-cells with calendered anodes at a 0.84 MPa fixed pressure. The capacity retention is defined as the capacity per cycle divided by the initial capacity of the cells.*

	Initial $E_{\text{Vol}}$ (BOL) /Wh L <sup>-1</sup>	Initial cell ca- pacity (BOL) /Ah	Initial stack volume* (BOL) /cm <sup>3</sup>	$E_{\text{Vol}}$ at EOL /Wh L <sup>-1</sup>	Cycles until EOL /-	Charge through- put at EOL /Ah	$E_{\text{Vol}}$ after 100 cy- cles /Wh L <sup>-1</sup>
<b>C/Si NMC811- cells at 0.08 MPa fixed pressure</b>	563.1	0.672	26 x 0.170 = 4.420	455.1	49	60.4	242.1
<b>Si/C NMC811- cells (cal.) at 0.84 MPa fixed pressure</b>	497.6	0.706	26 x 0.202 = 5.252	399.5	96	116.5	396.2

\* The initial stack volume is not changing during the cycling due to the fixed compression of the cells.

However, both materials cannot meet the demands of the state-of-the-art requirements requesting a driving range of at least 300 km meaning more than 500 cycles.<sup>7</sup> The data provided in Table 7.1 will be plotted for a final comparison in Figure 7.5 in section 7.4.

## 7.2 Comparison of the pressure distribution and the expansion

The main driving force of the differentiating aging behavior of the C/Si|NMC811- and Si/C|NMC811-cells is caused by the higher volume expansion of the former. For a final comparison, the pressure distribution of both cells is regarded after 50 cycles in the discharged and the charged state at cell voltages of 2.7 V and 4.2 V, respectively. Figure 7.3a and b show the pressure mapping results of a C/Si|NMC811-cell compressed to an initial fixed pressure of 0.42 MPa. The pressure mapping results of a Si/C|NMC811-cell at an initial fixed pressure of 0.84 MPa are shown in Figure 7.3c and d. In addition to the pressure mappings, the pressure is plotted for one line across the cells' surfaces in x- and y-axis for each measurement at the point with the highest detected pressures. In case of the C/Si|NMC811-cell, the average pressure on the surface already increased by 88% to 0.79 MPa in the discharged and by 102.4% to 0.85 MPa in the charged state from its initial value of 0.42 MPa after 50 cycles. Furthermore, large pressure inhomogeneities can be observed on the surface of the charged cell, which were discussed in detail in section 5.2. Even though, the Si/C|NMC811-cell was initially compressed at a higher pressure of 0.84 MPa, the average pressure after 50 cycles increased only by 11.9% to 0.94 MPa in the discharged and by 16.6% to 0.94 MPa in the charged state. In addition, the pressure distribution is much more homogeneous on the surface of the Si/C|NMC811-cell (compare Figure 7.3b and d). The reason for this is obvious. The Si in the C/Si-anode is utilized completely while the Si in the Si/C-anode is only partially lithiated. Furthermore, the Si/C-anode provides an embedded porosity to buffer the volume expansion of the Si. Therefore, the vertical expansion of the Si/C-anode is much less compared to the C/Si-anode. From the operando expansion measurements presented in section 5.1 and 6.1, it could be observed that the C/Si|NMC811-cells expand totally by 19.0% during 100 cycles in the charged state. At the same time, the C/Si|NMC811-cells only show a total expansion of 4.9% after 100 cycles. Consequently, the repetitive breaking and need to re-form the protective SEI layer is reduced in the Si/C-anode. Consequently, in case of the fixed compression, the pressure increase of the Si/C|NMC811-cells is much lower. Therefore, the partial lithiation combined with porosity in the Si/C-composite helps to control the intrinsic volume expansion of the Si on cost of a reduced volumetric energy density. In literature, several groups tried to prevent the volume expansion of Si to enable the application in anode active materials. Dash and Pannala calculated the theoretical limit of the amount of Si in Si/C-composites to prevent a vertical volume expansion. They ended up with a value of around 11% Si by the assumption of providing a large enough void space in the electrode to buffer the expansion.<sup>197</sup> However, the herein presented results demonstrate that even when applying a high pressure on the Si-containing electrode, the volume expansion can never be prevented completely. In fact, the functionality of other components of the cell as

the separator are suffering in case of the herein evaluated anode material with  $\sim 8$  wt% Si. Kumar et al. investigated the change of stress in Si-containing anodes by in-situ dilatometry studies.<sup>198</sup> Their results fit to the herein observed phenomena declaring that the porosity has a large influence on the volumetric expansion of the anodes. As was presented in section 6.1, the uncalendered Si/C-anodes with a higher porosity showed a lower vertical expansion than the calendered ones, leading to the conclusion that the higher porosity helps to reduce the volume change on electrode level. Furthermore, for all material combinations, the flexible compression to a higher pressure reduces the vertical expansion of the cells by a forced expansion into the void pore volume in the electrodes. However, the compression cannot fully prevent the volume expansion of the Si.

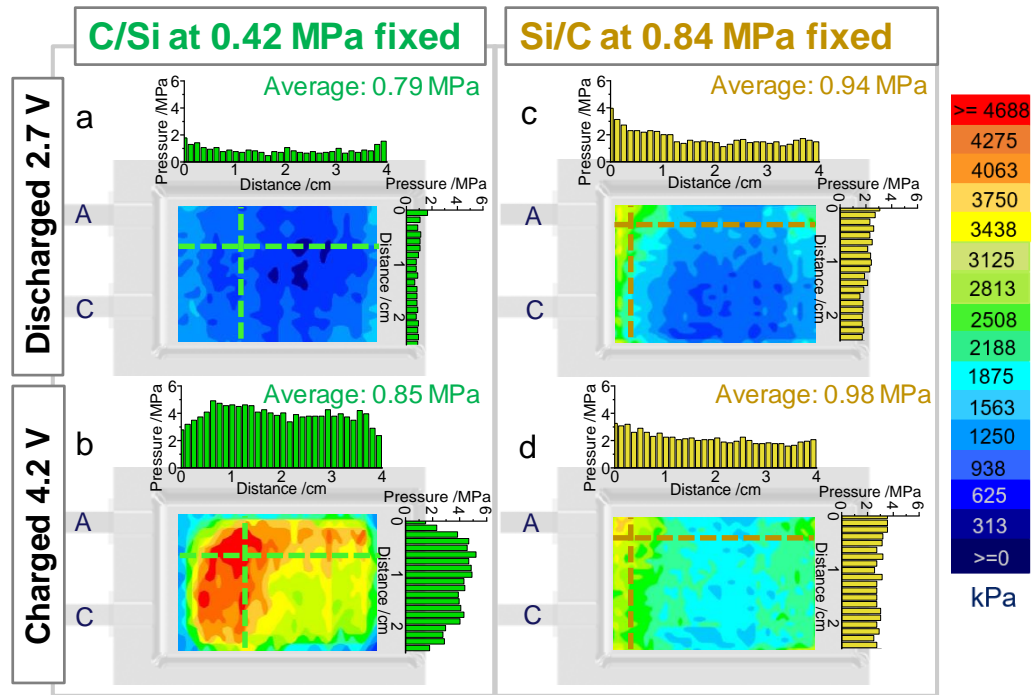


Figure 7.3: Comparison of the pressure distribution of a NMC811/C/Si pouch cell (a and b) and a NMC811/Si/C pouch cell (c and d) under fixed pressure configuration after 50 cycles. The pressure mapping is shown for the discharged (2.7 V) and charged state (4.2 V). The initially applied pressure levels were 0.42 MPa and 0.84 MPa for the NMC811/C/Si and NMC811/Si/C pouch cell, respectively.

### 7.3 C-rate capability

C-rate tests at different discharge C-rates of C/3 to 2C and at different compressions were performed for all cell types (see experimental section 3.3). Figure 7.4a, b, and c show the resulting relative capacity of the graphite|NMC622-, the C/Si|NMC811-, and the Si/C|NMC811-cells at different compression, i.e. uncompressed and flexibly compressed to 0.08 MPa, 0.42 MPa, and 0.84 MPa. In addition, the results for the fixed pressure configurations are shown in the supplementary material in Figure S3. The relative capacity is calculated based on the maximum discharge capacity of the respective cathode. As was discussed in section 4, the graphite|NMC622-cells suffer from the application of an increased pressure, especially at high C-rates. Due to the decrease of the pore volume in the graphite-anode, the ionic pore resistance increases reducing the ion mobility in the pores. Therefore, starting at a C-rate higher than 0.8C, these cells show a diminished capacity



output due to polarization effects. Contrarily, the compression has a positive influence on the C-rate capability of both, the C/Si|NMC811- and the Si/C|NMC811-cells (see Figure 7.4b and c). Especially the Si/C|NMC811-cells show a very good C-rate capability, which means that the capacity at higher C-rates is only decreased slightly to 89.9% in case of the heavily compressed (0.84 MPa) cell with uncalendered anodes. The C/Si|NMC811-cells show a slightly reduced C-rate capability with a relative capacity of 84.6% at 2C. In general, the C-rate capability is increased for the Si-containing anodes in comparison to the graphite-anodes with a relative capacity of only 77.7% at 2C. The reason for this is obvious. Due to the higher specific capacity of the Si-containing anodes of  $\sim 560 \text{ mAh g}^{-1}$  compared to  $\sim 335 \text{ mAh g}^{-1}$  of the graphite utilized in this work, the mass loading and therefore the thickness of the Si-containing anodes can be reduced drastically. Hence, Si-containing anodes do not only provide advantages regarding their theoretic volumetric energy density, but the C-rate capability is increased as well.

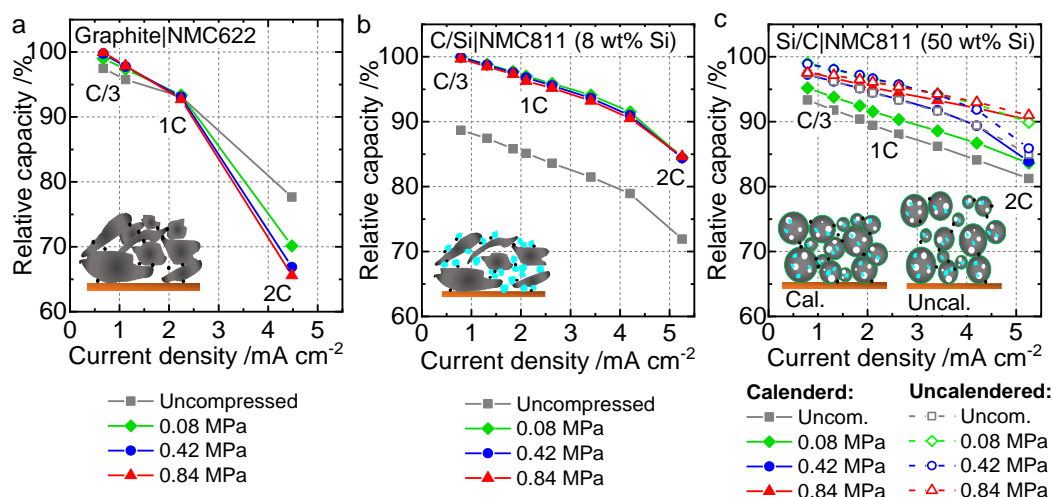


Figure 7.4: Comparison of the C-rate tests of the graphite|NMC622 (a), C/Si|NMC811- (b), and Si/C|NMC811-pouch cells (c) at different compression configuration and in case of the Si/C-anode calendered and uncalendered.

## 7.4 Summary of all contributions

Finally, all results regarding the performance of the Si-containing cells are summarized in a spider chart taking into account today's main requirements on the usability of LiBs.<sup>2-4</sup> In addition to the specifications mentioned beforehand, also a fourth, very important aspect, i.e. the safety, is considered. Figure 7.5 shows the resulting spider chart including the C-rate capability at 2C, the safety, the volumetric energy density, and the relative capacity after 100 cycles. The results obtained with the cells tested herein are compared to the state-of-the-art-requirements defined according to literature, i.e. a cycle life of at least 500 cycles at a capacity retention of 70%, a volumetric energy density of  $450 \text{ Wh L}^{-1}$ , and a remaining relative capacity of 80% at 2C.<sup>2,7-9</sup> Assuming a linear capacity retention of the cells, the state-of-the-art requirement of 70% remaining capacity at 500 cycles means a remaining capacity of 94% after 100 cycles. The state-of-the-art requirements are marked in green in the spider chart. The spider plot contains the results obtained from the graphite|NMC622-



cells in gray. Since the 0.08 MPa fixed and the 0.84 MPa fixed configuration showed the highest improvement of the performance of the C/Si|NMC811- and the Si/C|NMC811-cells, respectively, these results are contrasted with their uncompressed analogues. The results of the C/Si|NMC811-cells are shown in blue and the Si/C|NMC811-cells in red. The values of the relative capacity after 100 cycles and the volumetric energy density are derived from Figure 7.1 and Table 7.1, while the C-rate capability at 2C is a result of the C-rate tests presented in Figure 7.4.

To determine the safety of the test cells, various abuse tests, i.e. nail penetration and over-charge tests, were performed with 1.5 Ah stacked cells in the charged state during the project. According to EUCAR specifications, the safety of LiBs are defined in so-called Hazard Levels (HL), which is the outcome of the safety tests and is a value between 0 to 7. Thereby, a HL of 0 means that no effect was observed and the cell didn't lose any function during the event of the safety tests. A HL of 7 is defined as an explosion with the disintegration of the cell.<sup>199</sup> To fulfill automotive applications, the LiBs have to achieve a HL  $\leq 4$ , which means no flame or explosion during the event. A HL  $\leq 4$  is utilized for the state-of-the-art requirements plotted in green in Figure 7.5. In line with the expectations, the C/Si|NMC811- and the Si/C|NMC811-cells show a higher HL of 4 than the graphite|NMC622-cells with a HL of 3. The reason is the higher reactivity and the thermal instability of the NMC811 in comparison with the NMC622 which is a known problem.<sup>13,87,185,200</sup> However, several groups report of an improved thermal stability of Ni-rich NMCs achieved by coating with SiO<sub>2</sub>, TiO<sub>2</sub>, or Li<sub>2</sub>ZrO<sub>3</sub>.<sup>200–202</sup>

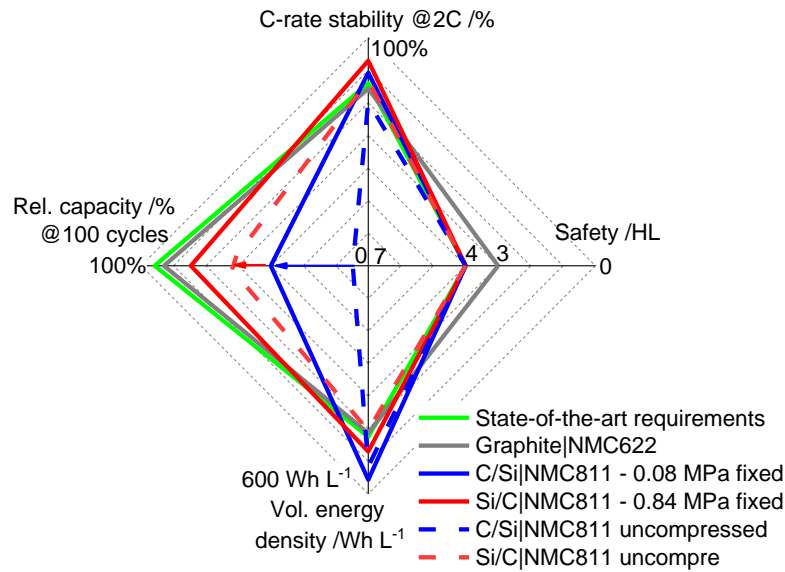


Figure 7.5: Spider chart of the results on graphite|NMC622-, C/Si|NMC811-, and Si/C|NMC811-pouch cells regarding requirements as the C-rate capability, the lifetime, the volumetric energy density, and the safety. The state-of-the-art requirements are derived from different literature sources.<sup>2,7–9</sup>

As discussed in section 7.1, the initial energy density of the C/Si|NMC811-cells at a 0.08 MPa fixed pressure with a value of 563.1 Wh L<sup>-1</sup> is higher than of the Si/C|NMC811-cells at a fixed pressure of 0.84 MPa with a value of 489.0 Wh L<sup>-1</sup>. Both exceed the state-of-the-art-requirements and demonstrate advantages when compared to the graphite|NMC622-cells with an initial volumetric energy density of 440.1 Wh L<sup>-1</sup>. Contrarily,

the Si/C|NMC811-cells exhibit a slight advantage with respect to the C-rate capability. With a remaining relative capacity of 89.9% at 2C, the Si/C|NMC811-cells exceed the state-of-the-art requirements significantly. As discussed in section 7.3, the reason for this is the high porosity at a concurrently thin coating thickness.

Concerning the lifetime, both Si-containing systems suffer from an accelerated capacity fading. The graphite|NMC622-cells show the highest remaining capacity of 90.6% after 100 cycles followed by the Si/C|NMC811-cells with 78.1% after 100 cycles. However, when comparing the uncompressed and compressed state of the cells with Si-containing anodes, a major extension of the lifetime can be achieved by the application of a well-defined pressure. Especially, when regarding the C/Si|NMC811-cells, the cycle life is prolonged drastically by around 40%.

Summarizing, the lifetime of both Si-containing systems is significantly improved by the application of a mechanical pressure. However, the applied pressure has to be adjusted precisely depending on the microstructural characteristics of the individual Si-composite-anode. Moreover, the C-rate capability and the initial volumetric energy density achieved with the Si-containing cells is promising when compared to the state-of-the-art and the graphite-baseline. Nevertheless, there still is a lot of potential for improvements with regards on the lifetime. From the results presented herein, the concept of a partial lithiation combined with an embedded porosity in the particles might be a promising idea to pursue. Since the material utilized in this work suffered from the untightness of the carbon coating on the Si/C-particles (see section 6.1.1 and 6.1.2), further developments should focus on this topic. In addition, improvements regarding the utilized electrolyte and binders of the anodes in combination with an externally applied pressure might be a promising approach.

## 8 Conclusion and outlook

In this work, the influence of mechanical pressure on aging, performance, and swelling behavior of silicon (Si) containing Lithium-ion battery cells (LiBs) was investigated. For this purpose, LiBs assembled from two different types of next-generation Si-based anode active materials, were tested. The electrochemical results and expansion behavior of LiBs with a C/Si-anode with a low Si content of  $\sim 8$  wt% were compared to LiBs with a Si/C-anode containing a high Si mass ratio of  $\sim 50$  wt%. While former exhibits a high vertical expansion due to the utilization of the full capacity of the Si, latter shows significantly less volume expansion, since the Si is implemented into a matrix with embedded porosity and is only partially lithiated. To enable a reasonable comparison, both anodes were tested in LiBs with the same Ni-rich NMC811-cathode. Furthermore, LiBs containing a graphite-anode and an NMC622-cathode meeting today's standards in terms of performance and expansion behavior were examined in an analogue way to create a baseline of reference data.

There are several approaches in literature trying to determine the expansion of various materials during the lithiation.<sup>62,138–142,145,146</sup> However, none of them provides insights into the swelling behavior of LiBs compressed with a defined pressure. In this work, an operando expansion measurement system was developed enabling the application and the adjustment of a homogeneous pressure on the LiB. Furthermore, the pressure distribution on the surface of the LiBs was tracked spatially resolved during the cycling employing a new pressure mapping technique. The cells were tested in a flexible and fixed pressure configuration. The flexible configuration allows the LiBs to expand while the pressure on the surface is kept constant during the operando expansion measurement. In contrast, the fixed configuration inhibits the expansion of the LiBs during the cycling, leading to a gradual increase of the pressure.

In the first step, the influence of the applied mechanical pressure on the electrodes was evaluated. The compressibility of the different anode and cathode materials as well as of the separator and the electrode stacks was determined. The results exhibited a strong dependency of the compressibility of the electrodes on the particle size of the active material as well as on the porosity. A decreased particle size or an increased porosity increase the compressibility. Furthermore, a non-linear correlation between the number of layers of an electrode stack and the resulting compressibility was revealed. With a small number of layers, the compressibility of each layer is larger than it is in an electrode stack consisting of more layers under the same mechanical pressure. This means that the utilized mechanical pressure must be adjusted not only depending on the material and electrode properties but also on the number of layers applied in the LiB. The number of layers in the LiB should be above 10 to enable reproducible conditions when applying mechanical pressure. Besides, symmetric EIS measurements of the electrodes enabled the evaluation of the pressure-dependent ionic pore resistance. The results show a decrease of the  $\text{Li}^+$  mobility in the reduced pore volume of compressed electrodes. This effect is even more pronounced for highly loaded electrodes. The direct influence of the increased ionic pore resistance on a reduced

C-rate capability in compressed cells was observed for graphite|NMC622-cells. Furthermore, the results of the EIS measurements have shown that the electric contact in the cells is improved by the mechanical compression, resulting in a higher reversible capacity at low C-rates compared to the uncompressed state. However, for C-rates above 0.8C the increased ionic pore resistance led to a significant rise of the polarization, which, in turn, reduces the available capacity. These first results demonstrated the importance of understanding the electrochemical processes in compressed electrodes and the necessity for a precise adjustment of the applied pressure for the respective application.

In the second part of this work, the influence of the mechanical pressure on Si-containing cells with a high expansion was examined. Since the capacity of the Si is utilized completely and by optimizing the applied pressure, the C/Si|NMC811-cells achieved a high initial volumetric energy density of  $563 \text{ Wh L}^{-1}$ . However, the material suffers from its repetitive high volume expansion reducing the lifetime significantly. When cycled without compression, a total swelling of 27.5% after 100 cycles was detected. This leads to a severe particle-particle contact loss, fracture of the particles, and layer detachments. The loss of contact in turn results in an accelerated electrolyte decomposition under gas formation detected by high precision dilatometry measurements. The cycle life could be prolonged drastically by applying a slightly fixed (0.08 MPa) or a medially flexible (0.42 MPa) pressure increasing the remaining capacity after 100 cycles by 33%. However, the cell aging was accelerated for higher fixed or flexible pressures. Employing an extensive post-mortem study and operando spatially resolved pressure mappings, two different aging mechanisms were identified. On the one hand, when compressed to a heavily flexible pressure, the cells suffer from their repetitive film formation and trapping of cycleable Li, causing a linear degradation. On the other hand, under a heavily fixed pressure, the attempt of preventing the expansion of the C/Si-anode leads to the generation of pressure hot spots resulting in pore closure of the separator.

The morphological design of the second Si/C-composite investigated in this work provides an approach to overcome the disadvantages of the first one. The material concept is to prevent the high volume expansion by embedding the Si and void pore volume in a C-matrix. To keep the designed particle structure intact during the lithiation of the Si, the capacity of the implemented Si is limited to approx. 30%. In combination with an optimized applied pressure in the cells, the total swelling during the cycling of the Si/C|NMC811-cells was reduced to 4.5% after 100 cycles. Even though, the composite structure provides an intrinsic porosity, the outer mechanical pressure is necessary to force the Si to utilize it instead of expanding vertically. Since the intrinsic density of the material and therewith of the electrode is very low, calendering experiments were performed to increase the volumetric energy density. Thereby, interesting correlations of the calendering process with the applied mechanical pressure were observed. In any case, the calendering process led to particle cracking resulting in an accelerated capacity fading of the cells. Interestingly, the accelerated capacity fading of the damaged active material could be decelerated by the application of a high mechanical pressure. Both, the lifetime and the volumetric energy density were improved significantly. In this manner, it was possible to increase the lifetime of the cells to a remaining capacity of 78.1% compared to 54.9% in the uncompressed state. However,

in comparison to the C/Si|NMC811-cells discussed above, the improvement of the lifetime is on cost of the volumetric energy density.

Furthermore, interesting results on particle cracking of the Ni-rich NMC811-cathode due to a potential shift were gained. The generally higher lithiation cut-off potential of the Si-rich anodes compared to graphite gradually forces the cathode potential to higher values when keeping the same voltage window including a constant voltage step during charging the full cells. The upper cathode potential was found to be shifted to values  $> 4.35$  V vs.  $\text{Li/Li}^+$  during the cycling in the Si/C|NMC811-cells causing cracking of the NMC particles. The findings demonstrate the high importance of the precise adjustment of the cycling conditions of Si-containing anodes in full cell applications. Based on the knowledge gained on pouch cell level, prismatic cells (PHEV1 format) were assembled from Si/C-anodes and NMC811-cathodes. Employing operando expansion and X-ray CT measurements, the mechanical deformation of the jelly roll in the prismatic cells cycled with and without a mechanical compression was analyzed. The PHEV1 cells cycled without compression suffered from layer detachments and contact loss, which was confirmed by the X-ray CT analysis. These processes lead to a strongly accelerated capacity fading. Contrariwise, the compressed PHEV1 cells showed a reproducible behavior compared to the compressed pouch cells in terms of their capacity retention and their irreversible swelling. A deviation of the swelling behavior was observed compared to the pouch cells. This could be explained by a careful evaluation of the results from X-ray CT measurements.

This work provides important insights into the challenges, which have to be taken into account when utilizing Si in next-generation LiB applications. First results on the sensitivity and on the effects of the application of mechanical pressure on Si-containing LiBs in different cell formats were presented. This is the first step to enable the extensive utilization of these materials providing an increased specific capacity in nowadays LiB applications. However, numerous challenges remain, which need to be overcome in the future.

On electrode level, both introduced Si-containing composite concepts showed their advantages and disadvantages in terms of a high volume expansion on cost of the lifetime and vice versa. Therefore, a combination of both concepts could be a promising approach i.e. reducing the void space in the C-matrix of the Si/C-composite to increase the volumetric energy density and at the same time, maintaining a reduced volume expansion of the material. This approach could be realized by following the concept of the partial lithiation. On the cell level, the application of a mechanical pressure has to be adjusted precisely based on the knowledge gained in this work. Regarding the positive electrode, improvements of the stability of Ni-rich cathode materials by coating or doping techniques as well as the precise setting of the potential windows need to be pursued. Corrugations of the jelly roll in prismatic cells with Si-containing anodes are a severe drawback, which can be diminished by optimizing the jelly roll geometry. To reduce the tensile stress and enable a homogenous utilization of the active material, changing the geometry to an electrode stack instead of using a spirally wound roll might be promising.

Generally, the use of such cells exhibiting high volume expansion during the cycling will challenge the module and pack development. Today's module constraints are designed to

---

hold the cells in place applying no or only a light pressure on the cells. Hence, future module designs have to be created, which enable the application of higher mechanical pressures on the cells while withstanding the expansion of the cells.

## References

1. ZSW, (2019) [https://www.zsw-bw.de/fileadmin/user\\_upload/PDFs/Pressemitteilungen/2019/pi02-2019-ZSW-WeltweiteZahlenElektroautos.pdf](https://www.zsw-bw.de/fileadmin/user_upload/PDFs/Pressemitteilungen/2019/pi02-2019-ZSW-WeltweiteZahlenElektroautos.pdf), (2020-02-11).
2. Fraunhofer ISI, (2017) <https://www.isi.fraunhofer.de/content/dam/isi/dokumente/cct/lib/Energiespeicher-Roadmap-Dezember-2017.pdf>, (2020-04-26).
3. B. Scrosati and J. Garche, *Journal of Power Sources*, **195**, 2419–2430 (2010).
4. J.-M. Tarascon and M. Armand, *Nature*, **414**, 359–367 (2001).
5. M. Marinaro, D. Bresser, E. Beyer, P. Faguy, K. Hosoi, H. Li, J. Sakovica, K. Amine, M. Wohlfahrt-Mehrens, and S. Passerini, *Journal of Power Sources*, **459**, 228073 (2020).
6. D. Bresser, K. Hosoi, D. Howell, H. Li, H. Zeisel, K. Amine, and S. Passerini, *Journal of Power Sources*, **382**, 176–178 (2018).
7. D. Andre, H. Hain, P. Lamp, F. Maglia, and B. Stiaszny, *J. Mater. Chem. A*, **5**, 17174–17198 (2017).
8. D. Andre, S.-J. Kim, P. Lamp, S. F. Lux, F. Maglia, O. Paschos, and B. Stiaszny, *J. Mater. Chem. A*, **3**, 6709–6732 (2015).
9. Fraunhofer ISI, (2013) [https://www.isi.fraunhofer.de/content/dam/isi/dokumente/cct/lib/PRM-LIB-2030\\_en.pdf](https://www.isi.fraunhofer.de/content/dam/isi/dokumente/cct/lib/PRM-LIB-2030_en.pdf), (2020-04-26).
10. Battery 2030+, (2020) [https://battery2030.eu/digitalAssets/815/c\\_815818-l\\_1-k\\_battery-2030\\_roadmap-v2.1.pdf](https://battery2030.eu/digitalAssets/815/c_815818-l_1-k_battery-2030_roadmap-v2.1.pdf), (2020-02-11).
11. M. Winter, J. O. Besenhard, M. E. Spahr, and P. Novák, *Adv. Mater.*, **10**, 725–763 (1998).
12. T. Ohzuku and Y. Makimura, *Chem. Lett.*, **30**, 642–643 (2001).
13. F. Schipper, E. M. Erickson, C. Erk, J.-Y. Shin, F. F. Chesneau, and D. Aurbach, *J. Electrochem. Soc.*, **164**, A6220–A6228 (2017).
14. M. T. McDowell, S. W. Lee, W. D. Nix, and Y. Cui, *Adv. Mater.*, **25**, 4966–4985 (2013).
15. C. J. Wen and R. A. Huggins, *Journal of Solid State Chemistry*, **37**, 271–278 (1981).
16. C. van der Marel, G. J. B. Vinke, and W. van der Lugt, *Solid State Communications*, **54**, 917–919 (1985).
17. M. N. Obrovac and V. L. Chevrier, *Chem. Rev.*, **114**, 11444–11502 (2014).
18. V. L. Chevrier and J. R. Dahn, *J. Electrochem. Soc.*, **156**, A454 (2009).



19. M. N. Obrovac and L. Christensen, *Electrochemical and Solid-State Letters*, **7**, A93–A96 (2004).
20. L. Y. Beaulieu, T. D. Hatchard, A. Bonakdarpour, M. D. Fleischauer, and J. R. Dahn, *J. Electrochem. Soc.*, **150**, A1457 (2003).
21. L. Shi, C. Pang, S. Chen, M. Wang, K. Wang, Z. Tan, P. Gao, J. Ren, Y. Huang, H. Peng, and Z. Liu, *Nano Lett.*, **17**, 3681–3687 (2017).
22. L. Shi, W. Wang, A. Wang, K. Yuan, Z. Jin, and Y. Yang, *Journal of Power Sources*, **318**, 184–191 (2016).
23. F. Luo, B. Liu, J. Zheng, G. Chu, K. Zhong, H. Li, X. Huang, and L. Chen, *J. Electrochem. Soc.*, **162**, A2509–A2528 (2015).
24. D. J. Lee, M.-H. Ryou, J.-N. Lee, B. G. Kim, Y. M. Lee, H.-W. Kim, B.-S. Kong, J.-K. Park, and J. W. Choi, *Electrochemistry Communications*, **34**, 98–101 (2013).
25. K. Richter, T. Waldmann, M. Memm, M. Kasper, and M. Wohlfahrt-Mehrens, *J. Electrochem. Soc.*, **165**, A3602–A3604 (2018).
26. W.-J. Zhang, *Journal of Power Sources*, **196**, 13–24 (2011).
27. X. Su, Q. Wu, J. Li, X. Xiao, A. Lott, W. Lu, B. W. Sheldon, and J. Wu, *Adv. Energy Mater.*, **4**, 1300882 (2014).
28. U. Kasavajjula, C. Wang, and A. J. Appleby, *Journal of Power Sources*, **163**, 1003–1039 (2007).
29. J. Yang, N. Solomatin, A. Kraytsberg, and Y. Ein-Eli, *ChemistrySelect*, **1**, 572–576 (2016).
30. T. Schott, R. Robert, P. A. Ulmann, P. Lanz, S. Zürcher, M. E. Spahr, P. Novák, and S. Trabesinger, *J. Phys. Chem. C*, **121**, 18423–18429 (2017).
31. K. Dong, H. Markötter, F. Sun, A. Hilger, N. Kardjilov, J. Banhart, and I. Manke, *ChemSusChem*, **12**, 261–269 (2019).
32. H. Takezawa, S. Ito, H. Yoshizawa, and T. Abe, *Journal of Power Sources*, **324**, 45–51 (2016).
33. G. Jeong, S. M. Lee, N. S. Choi, Y.-U. Kim, and C. K. Lee, *Electrochimica Acta*, **56**, 5095–5101 (2011).
34. X. Xiao, W. Zhou, Y. Kim, I. Ryu, M. Gu, C. Wang, G. Liu, Z. Liu, and H. Gao, *Adv. Funct. Mater.*, **25**, 1426–1433 (2015).
35. W.-R. Liu, M.-H. Yang, H.-C. Wu, S. M. Chiao, and N.-L. Wu, *Electrochem. Solid-State Lett.*, **8**, A100 (2005).
36. C. Xu, F. Lindgren, B. Philippe, M. Gorgoi, F. Björefors, K. Edström, and T. Gustafsson, *Chem. Mater.*, **27**, 2591–2599 (2015).

37. T. Chen, J. Hu, L. Zhang, J. Pan, Y. Liu, and Y.-T. Cheng, *Journal of Power Sources*, **362**, 236–242 (2017).
38. A. Baasner, F. Reuter, M. Seidel, A. Krause, E. Pflug, P. Härtel, S. Dörfler, T. Abendroth, H. Althues, and S. Kaskel, *J. Electrochem. Soc.*, **167**, 020516 (2020).
39. D. Mazouzi, Z. Karkar, C. Reale Hernandez, P. Jimenez Manero, D. Guyomard, L. Roué, and B. Lestriez, *Journal of Power Sources*, **280**, 533–549 (2015).
40. X. Liu, Y. Du, L. Hu, X. Zhou, Y. Li, Z. Dai, and J. Bao, *J. Phys. Chem. C*, **119**, 5848–5854 (2015).
41. S. D. Beattie, M. J. Loveridge, M. J. Lain, S. Ferrari, B. J. Polzin, R. Bhagat, and R. Dashwood, *Journal of Power Sources*, **302**, 426–430 (2016).
42. L.-H. Huang, D. Chen, C.-C. Li, Y.-L. Chang, and J.-T. Lee, *J. Electrochem. Soc.*, **165**, A2239–A2246 (2018).
43. J. L. Gómez-Cámer, C. Bünzli, M. M. Hantel, T. Poux, and P. Novák, *Carbon*, **105**, 42–51 (2016).
44. B. P. N. Nguyen, J. Gaubicher, and B. Lestriez, *Electrochimica Acta*, **120**, 319–326 (2014).
45. V. Etacheri, O. Haik, Y. Goffer, G. A. Roberts, I. C. Stefan, R. Fasching, and D. Aurbach, *Langmuir*, **28**, 965–976 (2012).
46. J. G. Lee, J. Kim, J. B. Lee, H. Park, H.-S. Kim, J. H. Ryu, D. S. Jung, E. K. Kim, and S. M. Oh, *J. Electrochem. Soc.*, **164**, A6103–A6109 (2017).
47. D.-T. Nguyen, J. Kang, K.-M. Nam, Y. Paik, and S.-W. Song, *Journal of Power Sources*, **303**, 150–158 (2016).
48. T. Jaumann, J. Balach, M. Klose, S. Oswald, U. Langklotz, A. Michaelis, J. Eckert, and L. Giebeler, *Phys. Chem. Chem. Phys.*, **17**, 24956–24967 (2015).
49. T. Jaumann, J. Balach, U. Langklotz, V. Sauchuk, M. Fritsch, A. Michaelis, V. Teltevskij, D. Mikhailova, S. Oswald, M. Klose, G. Stephani, R. Hauser, J. Eckert, and L. Giebeler, *Energy Storage Materials*, **6**, 26–35 (2017).
50. S. E. Trask, K. Z. Pupek, J. A. Gilbert, M. Klett, B. J. Polzin, A. N. Jansen, and D. P. Abraham, *J. Electrochem. Soc.*, **163**, A345–A350 (2016).
51. G. Berckmans, L. De Sutter, M. Marinaro, J. Smekens, J. Jaguemont, M. Wohlfahrt-Mehrens, J. van Mierlo, and N. Omar, *Electrochimica Acta*, **306**, 387–395 (2019).
52. L. De Sutter, G. Berckmans, M. Marinaro, J. Smekens, Y. Firouz, M. Wohlfahrt-Mehrens, J. van Mierlo, and N. Omar, *Energies*, **11**, 2948 (2018).
53. G. Berckmans, L. De Sutter, A. Kersys, A. Kriston, M. Marinaro, M. Kasper, P. Axmann, J. Smekens, M. Wohlfahrt-Mehrens, A. Pfrang, J. Jaguemont, J. Van Mierlo, and N. Omar, *WEVJ*, **9**, 43 (2018).

54. R. Korthauer, Ed., *Handbuch Lithium-Ionen-Batterien*, p. 436, Springer Vieweg, Berlin, (2013).
55. V. Etacheri, R. Marom, R. Elazari, G. Salitra, and D. Aurbach, *Energy Environ. Sci.*, **4**, 3243 (2011).
56. R. Schmuch, R. Wagner, G. Hörpel, T. Placke, and M. Winter, *Nat Energy*, **3**, 267–278 (2018).
57. M. M. Thackeray, C. Wolverton, and E. D. Isaacs, *Energy Environ. Sci.*, **5**, 7854 (2012).
58. H. Zhang, M.-Y. Zhou, C.-E. Lin, and B.-K. Zhu, *RSC Adv.*, **5**, 89848–89860 (2015).
59. R. Jung, M. Metzger, D. Haering, S. Solchenbach, C. Marino, N. Tsiouvaras, C. Stinner, and H. A. Gasteiger, *J. Electrochem. Soc.*, **163**, A1705–A1716 (2016).
60. T. Zheng, J. N. Reimers, and J. R. Dahn, *Phys. Rev. B*, **51**, 734–741 (1995).
61. R. Fong, *J. Electrochem. Soc.*, **137**, 5 (1990).
62. T. Ohzuku, N. Matoba, and K. Sawai, *Journal of Power Sources*, **5** (2001).
63. X. Y. Song, K. Kinoshita, and T. D. Tran, *J. Electrochem. Soc.*, **143**, L120–L123 (1996).
64. J. R. Dahn, *Phys. Rev. B*, **44**, 9170–9177 (1991).
65. E. Peled, *J. Electrochem. Soc.*, **144**, L208 (1997).
66. H. Buqa, A. Würsig, J. Vetter, M. E. Spahr, F. Krumeich, and P. Novák, *Journal of Power Sources*, **153**, 385–390 (2006).
67. V. A. Agubra and J. W. Fergus, *Journal of Power Sources*, **268**, 153–162 (2014).
68. V. Müller, R. Kaiser, S. Poller, and D. Sauerteig, *Journal of Energy Storage*, **15**, 256–265 (2018).
69. S. S. Zhang, *Journal of Power Sources*, **161**, 1385–1391 (2006).
70. S. S. Zhang, K. Xu, and T. R. Jow, *Journal of Power Sources*, **160**, 1349–1354 (2006).
71. P. Keil and A. Jossen, *Journal of Energy Storage*, **6**, 125–141 (2016).
72. Weixiang Shen, Thanh Tu Vo, and A. Kapoor, in *2012 7th IEEE Conference on Industrial Electronics and Applications (ICIEA)*, p. 1567–1572, IEEE, Singapore, Singapore (2012) <http://ieeexplore.ieee.org/document/6360973/>.
73. J. Vetter, P. Novák, M. R. Wagner, C. Veit, K.-C. Möller, J. O. Besenhard, M. Winter, M. Wohlfahrt-Mehrens, C. Vogler, and A. Hammouche, *Journal of Power Sources*, **147**, 269–281 (2005).

74. M. Broussely, S. Herreyre, P. Biensan, P. Kasztejna, K. Nechev, and R. J. Staniewicz, *Journal of Power Sources*, **9** (2001).
75. C. R. Birkl, M. R. Roberts, E. McTurk, P. G. Bruce, and D. A. Howey, *Journal of Power Sources*, **341**, 373–386 (2017).
76. T. Waldmann, B.-I. Hogg, and M. Wohlfahrt-Mehrens, *Journal of Power Sources*, **384**, 107–124 (2018).
77. S. H. Kim, Y. S. Kim, W. J. Baek, S. Heo, D.-J. Yun, S. Han, and H. Jung, *ACS Applied Materials & Interfaces*, **10**, 24549–24553 (2018).
78. R. E. Ruther, K. A. Hays, S. J. An, J. Li, D. L. Wood, and J. Nanda, *ACS Appl. Mater. Interfaces*, **10**, 18641–18649 (2018).
79. M. Wetjen, M. Trunk, L. Werner, R. Gernhäuser, B. Märkisch, Z. Révay, R. Gilles, and H. A. Gasteiger, *J. Electrochem. Soc.*, **165**, A2340–A2348 (2018).
80. M. Wetjen, D. Pritzl, R. Jung, S. Solchenbach, R. Ghadimi, and H. A. Gasteiger, *Journal of The Electrochemical Society*, **164**, A2840–A2852 (2017).
81. T. Weigel, F. Schipper, E. M. Erickson, F. A. Susai, B. Markovsky, and D. Aurbach, *ACS Energy Lett.*, **4**, 508–516 (2019).
82. N. Y. Kim, T. Yim, J. H. Song, J.-S. Yu, and Z. Lee, *Journal of Power Sources*, **307**, 641–648 (2016).
83. F. Lin, I. M. Markus, D. Nordlund, T.-C. Weng, M. D. Asta, H. L. Xin, and M. M. Doeff, *Nat Commun*, **5**, 3529 (2014).
84. F. Schipper, E. M. Erickson, C. Erk, J.-Y. Shin, F. F. Chesneau, and D. Aurbach, *J. Electrochem. Soc.*, **164**, A6220–A6228 (2017).
85. H. Kim, M. G. Kim, H. Y. Jeong, H. Nam, and J. Cho, *Nano Lett.*, **15**, 2111–2119 (2015).
86. S.-K. Jung, H. Gwon, J. Hong, K.-Y. Park, D.-H. Seo, H. Kim, J. Hyun, W. Yang, and K. Kang, *Advanced Energy Materials*, **4**, 1300787 (2014).
87. F. Schipper, H. Bouzaglo, M. Dixit, E. M. Erickson, T. Weigel, M. Talianker, J. Grinblat, L. Burstein, M. Schmidt, J. Lampert, C. Erk, B. Markovsky, D. T. Major, and D. Aurbach, *Adv. Energy Mater.*, **8**, 1701682 (2018).
88. F. Schipper, D. Dixit, M. Talianker, O. Haik, J. Grinblat, E. M. Erickson, C. Ghanty, D. T. Major, B. Markovsky, and D. Aurbach, *Journal of Materials Chemistry A*, **4**, 16073 (2016).
89. E. M. Erickson, H. Bouzaglo, H. Sclar, K.-J. Park, B.-B. Lim, F. Schipper, C. Ghanty, J. Grinblat, B. Markovsky, Y.-K. Sun, and D. Aurbach, *J. Electrochem. Soc.*, **163**, A1348–A1358 (2016).

90. C. Rahe, S. T. Kelly, M. N. Rad, D. U. Sauer, J. Mayer, and E. Figgemeier, *Journal of Power Sources*, **433**, 126631 (2019).
91. M. Wohlfahrt-Mehrens, C. Vogler, and J. Garche, *Journal of Power Sources*, **127**, 58–64 (2004).
92. H. Li, A. Liu, N. Zhang, Y. Wang, S. Yin, H. Wu, and J. R. Dahn, *Chem. Mater.*, **31**, 7574–7583 (2019).
93. J. Li, R. Shunmugasundaram, R. Doig, and J. R. Dahn, *Chem. Mater.*, **28**, 162–171 (2016).
94. E. Barsoukov and J. R. Macdonald, Eds., *Impedance spectroscopy: theory, experiment, and applications*, 2nd edition., p. 595, Wiley-Interscience, Hoboken (New Jersey), (2005).
95. T. Osaka, D. Mukoyama, and H. Nara, *Journal of The Electrochemical Society*, **162**, A2529–A2537 (2015).
96. S. Devan, V. R. Subramanian, and R. E. White, *J. Electrochem. Soc.*, **151**, A905 (2004).
97. J. P. Meyers, M. Doyle, R. M. Darling, and J. Newman, *J. Electrochem. Soc.*, **147**, 2930 (2000).
98. M. E. Orazem and B. Tribollet, *Electrochemical impedance spectroscopy*, p. 523, Wiley, Hoboken (New Jersey), (2008).
99. H. Brandstätter, I. Hanzu, and M. Wilkening, *Electrochimica Acta*, **207**, 218–223 (2016).
100. M. D. Levi, V. Dargel, Y. Shilina, D. Aurbach, and I. C. Halalay, *Electrochimica Acta*, **149**, 126–135 (2014).
101. N. Ogihara, Y. Itou, T. Sasaki, and Y. Takeuchi, *J. Phys. Chem. C*, **119**, 4612–4619 (2015).
102. N. Ogihara, S. Kawauchi, C. Okuda, Y. Itou, Y. Takeuchi, and Y. Ukyo, *Journal of The Electrochemical Society*, **159**, A1034–A1039 (2012).
103. J. Landesfeind, D. Pritzl, and H. A. Gasteiger, *J. Electrochem. Soc.*, **164**, A1773–A1783 (2017).
104. H. Nara, D. Mukoyama, R. Shimizu, T. Momma, and T. Osaka, *Journal of Power Sources*, **409**, 139–147 (2019).
105. A. S. Keefe, S. Buteau, I. G. Hill, and J. R. Dahn, *J. Electrochem. Soc.*, **166**, A3272–A3279 (2019).
106. J. Landesfeind, J. Hattendorff, A. Ehrl, W. A. Wall, and H. A. Gasteiger, *Journal of The Electrochemical Society*, **163**, A1373–A1387 (2016).
107. J. Landesfeind, M. Ebner, A. Eldiven, V. Wood, and H. A. Gasteiger, *J. Electrochem. Soc.*, **165**, A469–A476 (2018).

108. M. Ecker, T. K. D. Tran, P. Dechent, S. Käbitz, A. Warnecke, and D. U. Sauer, *J. Electrochem. Soc.*, **162**, A1836–A1848 (2015).
109. J. Li, E. Murphy, J. Winnick, and P. A. Kohl, *Journal of Power Sources*, **102**, 294–301 (2001).
110. S. Rodrigues, N. Munichandraiah, and A. K. Shukla, *Journal of Solid State Electrochemistry*, **3**, 397–405 (1999).
111. A. Jossen, *Journal of Power Sources*, **154**, 530–538 (2006).
112. C. H. Chen, J. Liu, and K. Amine, *Journal of Power Sources*, **96**, 321–328 (2001).
113. D. Andre, M. Meiler, K. Steiner, H. Walz, T. Soczka-Guth, and D. U. Sauer, *Journal of Power Sources*, **196**, 5349–5356 (2011).
114. D. R. Franceschetti, *J. Electrochem. Soc.*, **138**, 1368 (1991).
115. H. Nara, D. Mukoyama, T. Yokoshima, T. Momma, and T. Osaka, *Journal of The Electrochemical Society*, **163**, A434–A441 (2016).
116. D. Sauerteig, N. Hanselmann, A. Arzberger, H. Reinshagen, S. Ivanov, and A. Bund, *Journal of Power Sources*, **378**, 235–247 (2018).
117. J. Newman and K. E. Thomas-Alyea, *Electrochemical Systems*, Wiley-Interscience, (2004).
118. F. Pouraghajan, H. Knight, M. Wray, B. Mazzeo, R. Subbaraman, J. Christensen, and D. Wheeler, *J. Electrochem. Soc.*, **165**, A2644–A2653 (2018).
119. M. Gaberscek, J. Moskon, B. Erjavec, R. Dominko, and J. Jamnik, *Electrochem. Solid-State Lett.*, **11**, A170 (2008).
120. C.-W. Wang, A. M. Sastry, K. A. Striebel, and K. Zaghib, *J. Electrochem. Soc.*, **152**, A1001–A1010 (2005).
121. M. Ender, A. Weber, and E. Ivers-Tiffée, *Electrochemistry Communications*, **34**, 130–133 (2013).
122. M. Itagaki, Y. Hatada, I. Shitanda, and K. Watanabe, *Electrochimica Acta*, **8** (2010).
123. D. Wiedenmann et al., *AIChE J*, **59**, 1446–1457 (2013).
124. V. Müller, R. Bernhard, J. Wegener, J. Pfeiffer, S. Rössler, R.-G. Scurtu, M. Memm, M. A. Danzer, and M. Wohlfahrt-Mehrens, *J. Energy Technology* (2020) 2000217.
125. D. Jantke, R. Bernhard, E. Hanelt, T. Buhrmester, J. Pfeiffer, and S. Haufe, *J. Electrochem. Soc.*, **166**, A3881–A3885 (2019).
126. V. Müller, R.-G. Scurtu, M. Memm, M. A. Danzer, and M. Wohlfahrt-Mehrens, *Journal of Power Sources*, **440**, 227148 (2019).



127. T. Waldmann, A. Iturrondobeitia, M. Kasper, N. Ghanbari, F. Aguesse, E. Bekaert, L. Daniel, S. Genies, I. J. Gordon, M. W. Löble, E. D. Vito, and M. Wohlfahrt-Mehrens, *J. Electrochem. Soc.*, **163**, A2149–A2164 (2016).
128. V. Müller, R.-G. Scurtu, K. Richter, T. Waldmann, M. Memm, M. A. Danzer, and M. Wohlfahrt-Mehrens, *J. Electrochem. Soc.*, **166**, A3796–A3805 (2019).
129. L. De Sutter, G. Berckmans, M. Marinaro, J. Smekens, Y. Firouz, M. Wohlfahrt-Mehrens, J. van Mierlo, and N. Omar, *Energies*, **11**, 2948 (2018).
130. L. De Sutter, G. Berckmans, M. Marinaro, M. Wohlfahrt-Mehrens, M. Berecibar, and J. Van Mierlo, *Journal of Power Sources*, **451**, 227774 (2020).
131. A. J. Louli, L. D. Ellis, and J. R. Dahn, *Joule*, **3**, 745–761 (2019).
132. F. Nobili, F. Croce, B. Scrosati, and R. Marassi, *Chemistry of Materials*, **13**, 1642–1646 (2001).
133. X.-Y. Qiu, Q.-C. Zhuang, Q.-Q. Zhang, R. Cao, Y.-H. Qiang, P.-Z. Ying, and S.-G. Sun, *Journal of Electroanalytical Chemistry*, **687**, 35–44 (2012).
134. F. Nobili, R. Tossici, F. Croce, B. Scrosati, and R. Marassi, *Journal of Power Sources*, **94**, 238–241 (2001).
135. K. Kisu, S. Aoyagi, H. Nagatomo, E. Iwama, M. T. H. Reid, W. Naoi, and K. Naoi, *Journal of Power Sources*, **396**, 207–212 (2018).
136. A. J. Smith, J. C. Burns, D. Xiong, and J. R. Dahn, *J. Electrochem. Soc.*, **158**, A1136–A1142 (2011).
137. M. J. Mühlbauer, O. Dolotko, M. Hofmann, H. Ehrenberg, and A. Senyshyn, *Journal of Power Sources*, **348**, 145–149 (2017).
138. M. Nagayama, K. Ariyoshi, Y. Yamamoto, and T. Ohzuku, *J. Electrochem. Soc.*, **161**, A1388–A1393 (2014).
139. L. W. Sommer, A. Raghavan, P. Kiesel, B. Saha, J. Schwartz, A. Lochbaum, A. Ganguli, C.-J. Bae, and M. Alamgir, *J. Electrochem. Soc.*, **162**, A2664–A2669 (2015).
140. M. Hahn, H. Buqa, P. W. Ruch, D. Goers, M. E. Spahr, J. Ufheil, P. Novák, and R. Kötz, *Electrochem. Solid-State Lett.*, **11**, A151 (2008).
141. M. Winter, G. H. Wrodnigg, J. O. Besenhard, W. Biberacher, and P. Novák, *J. Electrochem. Soc.*, **147**, 2427 (2000).
142. B. Rieger, S. Schlueter, S. V. Erhard, J. Schmalz, G. Reinhart, and A. Jossen, *Journal of Energy Storage*, **6**, 213–221 (2016).
143. J. Barker, *Electrochimica Acta*, **45**, 235–242 (1999).

144. K.-Y. Oh, J. B. Siegel, L. Secondo, S. U. Kim, N. A. Samad, J. Qin, D. Anderson, K. Garikipati, A. Knobloch, B. I. Epureanu, C. W. Monroe, and A. Stefanopoulou, *Journal of Power Sources*, **267**, 197–202 (2014).
145. M. Bauer, M. Wachtler, H. Stöwe, J. V. Persson, and M. A. Danzer, *Journal of Power Sources*, **317**, 93–102 (2016).
146. M. Bauer, B. Rieger, S. Schindler, P. Keil, M. Wachtler, M. A. Danzer, and A. Jossen, *Journal of Energy Storage*, **10**, 1–10 (2017).
147. D. Sauerteig, S. Ivanov, H. Reinshagen, and A. Bund, *Journal of Power Sources*, **342**, 939–946 (2017).
148. A. J. Louli, J. Li, S. Trussler, C. R. Fell, and J. R. Dahn, *J. Electrochem. Soc.*, **164**, A2689–A2696 (2017).
149. T. Yoon, C. C. Nguyen, D. M. Seo, and B. L. Lucht, *J. Electrochem. Soc.*, **162**, A2325–A2330 (2015).
150. D. Y. W. Yu, M. Zhao, and H. E. Hoster, *CHEMELECTROCHEM*, **2**, 1090–1095 (2015).
151. C. Veth, D. Dragicevic, and C. Merten, *Journal of Power Sources*, **267**, 760–769 (2014).
152. T. Grandjean, A. Barai, E. Hosseinzadeh, Y. Guo, A. McGordon, and J. Marco, *Journal of Power Sources*, **359**, 215–225 (2017).
153. S. Kosch, A. Rheinfeld, S. V. Erhard, and A. Jossen, *Journal of Power Sources*, **342**, 666–676 (2017).
154. M. Sohn, D. G. Lee, D. J. Chung, A. Kim, and H. Kim, *Bull. Korean Chem. Soc.*, **40**, 150–156 (2019).
155. S. J. Cooper, A. Bertei, D. P. Finegan, and N. P. Brandon, *Electrochimica Acta*, **251**, 681–689 (2017).
156. S. Watanabe, M. Kinoshita, T. Hosokawa, K. Morigaki, and K. Nakura, *Journal of Power Sources*, **258**, 210–217 (2014).
157. H. Keiser, K. D. Beccu, and M. A. Gutjahr, *Electrochimica Acta*, **21**, 539–543 (1976).
158. M. Kroll, D. Hlushkou, S. Schlabach, A. Hölzel, B. Roling, and U. Tallarek, *J. Electrochem. Soc.*, **165**, A3156–A3163 (2018).
159. H.-K. Song, Y.-H. Jung, K.-H. Lee, and L. H. Dao, *Electrochimica Acta*, **7** (1999).
160. H.-K. Song, H.-Y. Hwang, K.-H. Lee, and L. H. Dao, *Electrochimica Acta*, **45**, 2241–2257 (2000).
161. S. Malifarge, B. Delobel, and C. Delacourt, *J. Electrochem. Soc.*, **164**, E3329–E3334 (2017).

162. C. Peabody and C. B. Arnold, *Journal of Power Sources*, **196**, 8147–8153 (2011).
163. J. Cannarella and C. B. Arnold, *Journal of Power Sources*, **226**, 149–155 (2013).
164. M. F. Lagadec, R. Zahn, S. Müller, and V. Wood, *Energy Environ. Sci.*, **11**, 3194–3200 (2018).
165. M. F. Lagadec, R. Zahn, and V. Wood, *Journal of The Electrochemical Society*, **165**, A1829–A1836 (2018).
166. X. Zhang, E. Sahraei, and K. Wang, *Sci Rep*, **6**, 32578 (2016).
167. M. Haruta, T. Doi, and M. Inaba, *J. Electrochem. Soc.*, **166**, A258–A263 (2019).
168. C.-H. Hsu, H.-Y. Chen, and C.-J. Tsai, *Journal of Power Sources*, **438**, 226943 (2019).
169. K. Yasuda, Y. Kashitani, S. Kizaki, K. Takeshita, T. Fujita, and S. Shimosaki, *Journal of Power Sources*, **329**, 462–472 (2016).
170. N. Delpuech, N. Dupre, P. Moreau, J.-S. Bridel, J. Gaubicher, B. Lestriez, and D. Guyomard, *ChemSusChem*, **9**, 841–848 (2016).
171. A. J. Smith, J. C. Burns, X. Zhao, D. Xiong, and J. R. Dahn, *J. Electrochem. Soc.*, **158**, A447 (2011).
172. J. Guo, A. Sun, X. Chen, C. Wang, and A. Manivannan, *Electrochimica Acta*, **56**, 3981–3987 (2011).
173. F. B. Spingler, W. Wittmann, J. Sturm, B. Rieger, and A. Jossen, *Journal of Power Sources*, **393**, 152–160 (2018).
174. V. Zinth, C. von Lüders, M. Hofmann, J. Hattendorff, I. Buchberger, S. Erhard, J. Rebelo-Kornmeier, A. Jossen, and R. Gilles, *Journal of Power Sources*, **271**, 152–159 (2014).
175. C. von Lüders, V. Zinth, S. V. Erhard, P. J. Osswald, M. Hofmann, R. Gilles, and A. Jossen, *Journal of Power Sources*, **342**, 17–23 (2017).
176. B. B. Berkes, A. Schiele, H. Sommer, T. Brezesinski, and J. Janek, *J Solid State Electrochem*, **20**, 2961–2967 (2016).
177. C. P. Aiken, J. Xia, D. Y. Wang, D. A. Stevens, S. Trussler, and J. R. Dahn, *J. Electrochem. Soc.*, **161**, A1548–A1554 (2014).
178. J. Self, C. P. Aiken, R. Petibon, and J. R. Dahn, *J. Electrochem. Soc.*, **162**, A796–A802 (2015).
179. R. Petibon, V. L. Chevrier, C. P. Aiken, D. S. Hall, S. R. Hyatt, R. Shunmugasundaram, and J. R. Dahn, *J. Electrochem. Soc.*, **163**, A1146–A1156 (2016).
180. N. Liu, Z. Lu, J. Zhao, M. T. McDowell, H.-W. Lee, W. Zhao, and Y. Cui, *Nature Nanotech*, **9**, 187–192 (2014).

181. Q. Xu, J.-Y. Li, J.-K. Sun, Y.-X. Yin, L.-J. Wan, and Y.-G. Guo, *Adv. Energy Mater.*, **7**, 1601481 (2017).
182. M. N. Obrovac and L. J. Krause, *J. Electrochem. Soc.*, **154**, A103–A108 (2007).
183. B. P. N. Nguyen, S. Chazelle, M. Cerbelaud, W. Porcher, and B. Lestriez, *Journal of Power Sources*, **262**, 112–122 (2014).
184. Y. Oumellal, N. Delpuech, D. Mazouzi, N. Dupré, J. Gaubicher, P. Moreau, P. Soudan, B. Lestriez, and D. Guyomard, *J. Mater. Chem.*, **21**, 6201 (2011).
185. S.-M. Bak, E. Hu, Y. Zhou, X. Yu, S. D. Senanayake, S.-J. Cho, K.-B. Kim, K. Y. Chung, X.-Q. Yang, and K.-W. Nam, *ACS Appl. Mater. Interfaces*, **6**, 22594–22601 (2014).
186. S. Zheng, R. Huang, Y. Makimura, Y. Ukyo, C. A. J. Fisher, T. Hirayama, and Y. Ikuhara, *J. Electrochem. Soc.*, **158**, A357 (2011).
187. H. Liu, M. Wolf, K. Karki, Y.-S. Yu, E. A. Stach, J. Cabana, K. W. Chapman, and P. J. Chupas, *Nano Lett.*, **17**, 3452–3457 (2017).
188. P.-C. Tsai, B. Wen, M. Wolfman, M.-J. Choe, M. S. Pan, L. Su, K. Thornton, J. Cabana, and Y.-M. Chiang, *Energy Environ. Sci.*, **11**, 860–871 (2018).
189. G. Sun, T. Sui, B. Song, H. Zheng, L. Lu, and A. M. Korsunsky, *Extreme Mechanics Letters*, **9**, 449–458 (2016).
190. C. Tian, Y. Xu, D. Nordlund, F. Lin, J. Liu, Z. Sun, Y. Liu, and M. Doeff, *Joule*, **2**, 464–477 (2018).
191. F. Reuter, A. Baasner, J. Pampel, M. Piwko, S. Dörfler, H. Althues, and S. Kaskel, *J. Electrochem. Soc.*, **166**, A3265–A3271 (2019).
192. M. J. Mühlbauer, A. Schökel, M. Etter, V. Baran, and A. Senyshyn, *Journal of Power Sources*, **403**, 49–55 (2018).
193. A. S. Mussa, G. Lindbergh, M. Klett, P. Gudmundson, P. Svens, and R. W. Lindström, *Journal of Energy Storage*, **20**, 213–217 (2018).
194. T. Wierzbicki and E. Sahraei, *Journal of Power Sources*, **241**, 467–476 (2013).
195. M. Fleckenstein, O. Bohlen, M. A. Roscher, and B. Bäker, *Journal of Power Sources*, **196**, 4769–4778 (2011).
196. D. Liu, Y. Wang, Y. Xie, L. He, J. Chen, K. Wu, R. Xu, and Y. Gao, *Journal of Power Sources*, **232**, 29–33 (2013).
197. R. Dash and S. Pannala, *Sci Rep*, **6**, 27449 (2016).
198. R. Kumar, J. H. Woo, X. Xiao, and B. W. Sheldon, *J. Electrochem. Soc.*, **164**, A3750–A3765 (2017).

- 
199. Eucar, *Battery requirements for future automotive applications*, EUCAR Document, EG BEV&FCEV (2019) 1-18.
200. K. Meng, Z. Wang, H. Guo, X. Li, and D. Wang, *Electrochimica Acta*, **211**, 822–831 (2016).
201. D. Zuo, C. Wang, G. Tian, K. Shu, and X. Liu, 13 (2019).
202. W. Cho, S.-M. Kim, J. H. Song, T. Yim, S.-G. Woo, K.-W. Lee, J.-S. Kim, and Y.-J. Kim, *Journal of Power Sources*, **282**, 45–50 (2015).
203. Mathworks, <https://de.mathworks.com/help/optim/ug/lsqnonlin.html#d120e101056>, (2020-05-05).

## Nomenclature

$A$	Electrode area	$\text{cm}^2$
$d$	Electrode thickness	$\mu\text{m}$
$i_0$	Surface exchange current density	$\text{A m}^{-2}$
$L$	Inductance	$\text{F}$
$R_{\text{Co}}$	Interfacial contact resistance	$\Omega$
$R_{\text{Ct}}$	Charge-transfer resistance	$\Omega$
$R_{\text{Ct\_sum}}$	Sum of charge-transfer resistances	$\Omega$
$R_{\text{El}}$	Electric resistance	$\Omega$
$R_{\text{HF}}$	High frequency resistance	$\Omega$
$R_{\text{L}}$	Resistance of an inductor	$\Omega$
$R_{\text{P}}$	Ionic pore resistance	$\Omega$
$R_{\text{P,S}}$	Ionic pore resistance in the separator	$\Omega$
$c_l$	Li concentration in the electrolyte	$/$
$c_S$	Li concentration of active material	$/$
$c_{\text{S,max}}$	Maximum Li concentration	$/$
$k_a$ and $k_c$	Reaction rate	$\text{m s}^{-1}$
$\alpha$	Transfer factor	$/$
$\varepsilon$	Porosity	$\%$
$\tau$	Tortuosity	$/$
$\kappa$	conductivity	$\text{S m}^{-1}$



## Abbreviations

Al	Aluminum
BEV	Battery electric vehicles
BOL	Begin of life
C	Carbon
CC/CV	Constant current/constant voltage
CMC	Carboxymethyl cellulose
CPE	Constant phase element
CT	Computer tomography
Cu	Copper
DMC	Dymethylcarbonate
EC	Equivalent circuit
EIS	Electrochemical impedance spectroscopy
Electrolyte A	1 M LiPF <sub>6</sub> in EC:DEC 3:7 with 2 wt% VC
Electrolyte B	1 M LiPF <sub>6</sub> in EC:DEC 3:7 with 10 wt% FEC
Electrolyte C	0.5 M TBA in EC:EMC 3:7
Electrolyte D	1 M LiPF <sub>6</sub> in FEC:DEC 3:7 with 2 wt% VC
EOL	End of life
FEC	Fluoroethylene carbonate
ICL	Irreversible capacity loss
Li	Lithium
LiB	Lithium-ion battery cell
Mn	Manganese
Ni	Nickel
NMC622	LiNi <sub>0.6</sub> Mn <sub>0.2</sub> Co <sub>0.2</sub> O <sub>2</sub>
NMC811	LiNi <sub>0.8</sub> Mn <sub>0.1</sub> Co <sub>0.1</sub> O <sub>2</sub>
NMP	1-methyl-2-pyrrolidone
PE	Polyethylene
PHEV1	Prismatic cell format
PP	Polypropylene
PVDF	Polyvinylidene fluoride
SBR	Styrene-butadiene rubber
SEI	Solid-electrolyte interphase
Si	Silicon
SOC	State of charge
TBA	Tetrabutylammonium hexafluorophosphate
TLM	Transmission line model

## Supplementary Material

The EIS measurement data was fitted utilizing the function gained from the EC Figure 2.3 in section 2.3.1 in a nonlinear least-square curve fitting function (lsqnonlin)

$$\min_x ||f(x)||_2^2 = \min_x (f_1(x)^2 + f_2(x)^2 + \dots + f_n(x)^2) \quad (S0.1)$$

provided by MATLAB.<sup>203</sup>

The fitting function  $f(x)$

$$f(x) = \begin{pmatrix} Re\{Z\} - Re\left\{ \frac{R_L \cdot j\omega L}{R_L + j\omega L} + R_{HF} + \frac{R_1}{1 + (j\omega R_1 C_1)^{n_1}} + \frac{R_2}{1 + (j\omega R_2 C_2)^{n_2}} + \frac{R_3}{1 + (j\omega R_3 C_3)^{n_3}} + R_{D0} \cdot \tanh(B\sqrt{j\omega}) \right\} \\ Im\{Z\} - Im\left\{ \frac{R_L \cdot j\omega L}{R_L + j\omega L} + R_{HF} + \frac{R_1}{1 + (j\omega R_1 C_1)^{n_1}} + \frac{R_2}{1 + (j\omega R_2 C_2)^{n_2}} + \frac{R_3}{1 + (j\omega R_3 C_3)^{n_3}} + R_{D0} \cdot \tanh(B\sqrt{j\omega}) \right\} \end{pmatrix} \quad (S0.2)$$

was defined according to the EC provided in Figure 2.3 in section 2.3.1. The fitting was conducted utilizing upper and lower bounds, whereas the lower bound for all parameters was 0 while the upper bounds were adjusted depending on the measurement data.

According to the exponential function given in (4.1) in section 4.1, the variables  $a$  and  $b$  were determined utilizing the lsqnonlin-function in Matlab. For that, the fitting function was subtracted from the measured single layer compressibility and optimized. The resulting values for  $a$  and  $b$  are shown in Figure S0.1 for the various materials analyzed in Figure 4.1.

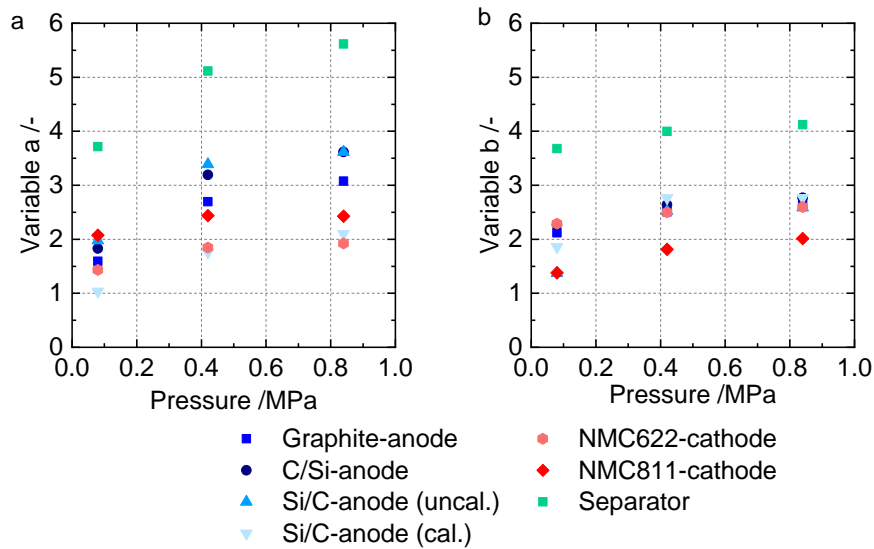


Figure S0.1: Determined fitting parameters of the single layer compressibility measurements shown in Figure 4.1. The fitting was conducted utilizing Matlab according to the function given in (4.1).

Figure S0.2 shows an example of the fitted data compared to the measurement data of the single layer compressibility versus the number of layers at the example of the NMC622-

cathode at a pressure of 0.08 MPa. The fitting function is given in (4.1) and the measurement data is provided in Figure 4.1. The best result was achieved for  $a = 1.4347$  and  $b = 2.2901$ .

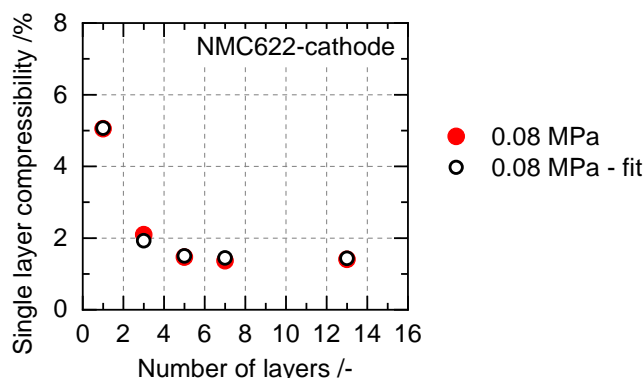


Figure S0.2: Example of the fitted data with the measurement data of the single layer compressibility versus the number of layers for the NMC622-cathode at a pressure of 0.08 MPa.

In addition to the cycling results of the flexibly compressed Si/C|NMC811-cells shown in Figure 6.1, cells were cycled under fixed compression at pressures of 0.08 MPa, 0.42 MPa, and 0.84 MPa. Figure S0.3 shows the specific discharge capacities and the Coulombic efficiency over 100 cycles for the differently compressed cells with calendered and uncalendered anodes. The available capacities are increased with an increased pressure. In addition, the cells with uncal. anodes show a slightly improved performance. The specific capacity after 100 cycles of these cells is added to the overview in Figure 6.1e.

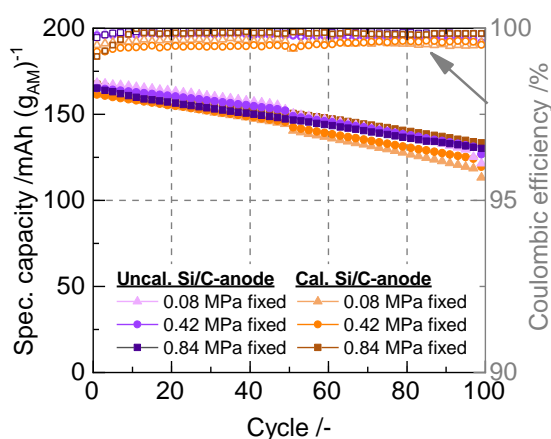


Figure S0.3: Cycling performance of the Si/C|NMC811-cells with calendered (cal.) and uncalendered (un-cal.) anodes at different fixed compression.

Figure S0.4 shows an EDX spectrum measured on a separator harvested from a Si/C|NMC811-cells cycled without compression. As can be seen in the spectrum in Figure S0.4b, the amount of F is increased drastically confirming the deposition of electrolyte decomposition products on the surface of the separator.

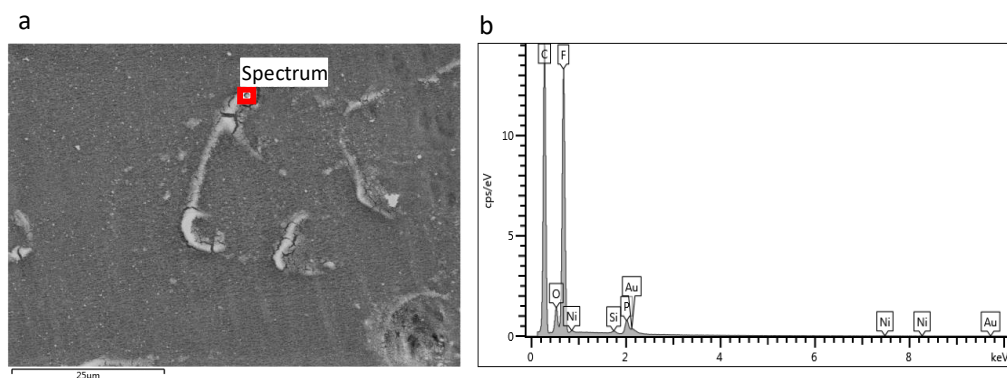


Figure S0.4: EDX spectrum of a harvested separator from Si/C|NMC811-cells cycled without compression. Analysis of the decomposition product on the separator. The separator was sputtered with Au for the investigation.

Figure S0.5 shows the results of the C-rate testing of the C/Si|NMC811- and Si/C|NMC811-cells cycled under fixed compression which were conducted to complement the C-rate results presented in Figure 7.4.

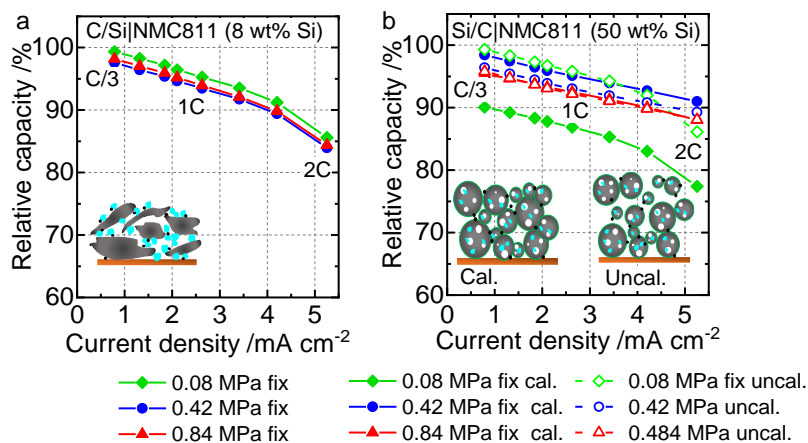


Figure S0.5: Overview of the C-rate tests of the C/Si|NMC811 (a) and Si/C|NMC811 (b) pouch cells at different fixed compression.

## Danksagungen

Zunächst möchte ich mich bei meinem Doktorvater, Prof. Dr. Michael Danzer, sowie bei meiner Fachgebietsleiterin, Frau Dr. Margret Wohlfahrt-Mehrens, für die Möglichkeit meiner Promotion bedanken. Ohne die zustande gekommene Kooperation zwischen dem Lehrstuhl für Elektrische Energiesystem (EES) der Universität Bayreuth und der Fachabteilung Akkumulatoren Materialforschung (ECM) am Zentrum für Sonnenenergie- und Wasserstoff-Forschung (ZSW) in Ulm, wäre meine Promotion nie ermöglicht worden.

Mein herzlicher Dank gilt auch Frau Prof. Dr. Christina Roth für die Übernahme des Zweitgutachtens meiner Arbeit.

Des Weiteren möchte ich mich beim Bundesministerium für Wirtschaft und Energie (BMWi) für die finanzielle Unterstützung während meiner Doktorarbeit im Rahmen des Projektes Lib.de bedanken.

Ein besonderer Dank geht auch an meine Kollegen am ZSW. Dabei möchte ich vor Allem meine Projektleiterin, Dr. Michaela Memm, nennen, die während der letzten Jahre immer ein offenes Ohr für anfallende Problemstellungen hatte. In addition, I would like to thank Dr. Rares-George Scurtu and Dr. Gilberto Carbonari for the fruitful collaboration and the heated discussions about impedance spectroscopy. Außerdem möchte ich mich speziell bei einigen Kollegen bedanken, deren Hilfsbereitschaft mich über die Zeit meiner Promotion immer wieder überrascht hat: Jürgen Hager & Georg Zettisch für ihre Hilfe bei jeglichen Konstruktionen; Benjamin Wiedemann, Christian Glöckner & Frank Häussler dafür, dass ich ihre Messgeräte nutzen durfte; Michael Kasper für sein offenes Ohr und die Hilfe bei den Zellöffnungen; Harald Brazel, Michael Wörz, Dr. Harry Döring und ihre ECA-ler dafür, dass ich über die Jahre den ein oder anderen Rat und Mess-Kanal bekommen habe. Meinen Mitstreitern im ECS Student-Chapter danke ich für den fachübergreifenden Austausch und die netten Abende. Dafür, dass sie mich und meine Büro-Dekoration die letzten Jahre ertragen haben, möchte ich meinen Bürokollegen Toni & Thomas danken.

Zu guter Letzt möchte ich mich bei meiner Familie bedanken. Besonders meinen Eltern danke ich, dass sie mich stets bei der Erreichung meiner Ziele unterstützt und an mich geglaubt haben.

Meinem Freund, Paul, danke ich für die notwendige Ablenkung an den Abenden, dafür, dass ich ihm meine teilweise konfuse Ideen quasi jederzeit mitteilen durfte und für seine Unterstützung bei deren Umsetzung im Labor.

## List of publications

1. Verena Müller, Rudi Kaiser, Silvan Poller, Daniel Sauerteig, Radu Schwarz, Martin Wenger, Vincent Lorentz, Martin März, „Introduction and application of formation methods based on serial-connected lithium-ion battery cells”, J. Energy Storage 14, pp. 56-61 (2017). <https://doi.org/10.1016/j.est.2017.09.013>
2. Verena Müller, Rudi Kaiser, Silvan Poller, Daniel Sauerteig, “Importance of the constant voltage charging step during lithium-ion cell formation”, J. Energy Storage 15, pp. 256-265 (2018). <https://doi.org/10.1016/j.est.2017.11.020>
3. Verena Müller, Rares-George Scurtu, Michaela Memm, Michael A. Danzer, Margret Wohlfahrt-Mehrens, „ Study of the influence of mechanical pressure on the performance and aging of Lithium-ion battery cells”, J. Power Sources 440 (2019) 227148. <https://doi.org/10.1016/j.jpowsour.2019.227148>
4. Verena Müller, Rares-George Scurtu, Karsten Richter, Thomas Waldmann, Michaela Memm, Michael A. Danzer, Margret Wohlfahrt-Mehrens, „ Effects of Mechanical Compression on the Aging and the Expansion Behavior of Si/C-Composite|NMC811 in Different Lithium-Ion Battery Cell Formats”, J. Electrochem. Soc., 166 (15) A1-A10 (2019). <https://doi.org/10.1149/2.1121915jes>
5. Verena Müller, Rebecca Bernhard, Jennifer Wegener, Jürgen Pfeiffer, Stefan Rössler, Rares-George Scurtu, Michaela Memm, Michael A. Danzer, Margret Wohlfahrt-Mehrens, „Evaluation of scalable porous Si-rich Si/C-composites with low volume expansion in coin to prismatic cell formats“, J. Energy Technology (2020) 2000217 <https://doi.org/10.1002/ente.202000217>
6. Gilberto Carbonari, Verena Müller, Rares-George Scurtu, Michaela Memm, Alice Hoffmann, Margret Wohlfahrt Mehrens, “Edge Quality Contribution on the Electrical Impedance of Lithium-ion Batteries Electrodes", J. Electrochem. Soc., 2020 167 080504. <https://iopscience.iop.org/article/10.1149/1945-7111/ab8875>



## Conference contributions

1. Verena Müller, Rares-George Scurtu, Michaela Memm, Michael A. Danzer, Margret Wohlfahrt-Mehrens, „Improvement of the electrochemical performance and life cycle of lithium-ion battery cells applying a homogeneous external pressure“, Ulm ElectroChemical Talks 16, 13. – 14. November 2018, Ulm, Germany
2. Verena Müller, Rares-George Scurtu, Michaela Memm, Michael A. Danzer, Margret Wohlfahrt-Mehrens, „Study of the electrochemical performance and life cycle of Lithium-ion battery cells applying a homogeneous external pressure“, Kraftwerk Batterie, 3. – 4. April 2019, Aachen, Germany
3. Verena Müller, Rares-George Scurtu, Michaela Memm, Michael A. Danzer, Margret Wohlfahrt-Mehrens, „Optimization of the electrochemical performance, the aging, and the volume expansion of next generation Si-composite lithium-ion battery cells by applying a mechanical pressure“, Advanced Lithium Batteries for Automobile Applications ABAA 12, 6. – 9. October 2019, Ulm, Germany
4. Gilberto Carbonari, Verena Müller, Rares-George Scurtu, Michaela Memm, Margret Wohlfahrt-Mehrens, „Electrochemical Impedance Spectroscopy: a Multi-diagnostic Tool for LiB Electrodes Characterization“, Advanced Lithium Batteries for Automobile Applications ABAA 12, 6. – 9. October 2019, Ulm, Germany
5. Philip Kargl, Verena Müller, Mario Marinaro, Patrick Kolm, Christoph Breitfuss, Alexander Thaler, Margret Wohlfahrt-Mehrens, Roland Würschum „Simulation and measurements of the expansion of Li-ion cells with Si-based anodes with a meso-mechanical – electrical finite-element model“, International Battery Production Conference IBPC, 4. – 6. November 2019, Braunschweig, Germany
6. Philip Kargl, Verena Müller, Patrick Kolm, Christoph Breitfuss, Martin Liebenberger, Mario Marinaro, Alexander Thaler, Margret Wohlfahrt-Mehrens, Roland Würschum „Study of the expansion of Li-ion cells with Si-based anodes with a combined approach of measurements and finite-element simulations“, Kraftwerk Batterie, 23. – 25. March 2020, Münster, Germany

## Curriculum vitae

### Personal data

**Name:** Verena Müller  
**Date and place of birth:** 21. September 1992 in Neustadt a. d. Aisch

### Education

**Master of Science** with distinction in electrical engineering at the Friedrich-Alexander University in Erlangen/Nürnberg

2014 – 2017 Master thesis entitled “*Untersuchung verschiedener Betriebsstrategien zur seriellen Formation von Li-Ionen Zellen*” supervised by Prof. M. März in a cooperation of Robert Bosch GmbH and Fraunhofer IISB

Short summary: *The thesis focused on the development of cost efficient serial formation strategies for the Li-ion battery cell manufacturing. Initially, several serial formation concepts as cell balancing as well as dropout systems were compared. Furthermore, the influences of changed formations parameters on the aging of the Li-ion cells was assessed.*

**Bachelor of Science** in electrical engineering at the Friedrich-Alexander University in Erlangen/Nürnberg

2011 – 2014 Bachelor thesis entitled “*Optische Qualitätskontrolle für Laserstrukturierungsprozesse von CIGS-Dünnschichtsolarmodulen*” supervised by Prof. B. Schmauß in a cooperation with Robert Bosch GmbH

Short summary: *The thesis focused on the development of an in-line system for the quality control of laser scribes on CIGS solar cells. A line scanning system was capacitated to online control the scribing quality of the CIGS layer. A method for an automated image processing was developed. Further techniques to characterize the scribing of the Mo and ZnO<sub>x</sub> were introduced.*

2003 – 2011 Abitur at Friedrich-Alexander Gymnasium Neustadt a. d. Aisch

### Scholarships, awards, and functions

2019 – today Vice president of the **ECS student section Ulm**

2013 – today Students @ Bosch

2012 – 2017 **Studienstiftung des deutschen Volkes**

2017 **Drive-E Studienpreis** in the category Master thesis awarded by the BMBF and the Fraunhofer Gesellschaften

## Working experience

- 2017 – today      **Research associate:** Center for Solar Energy and Hydrogen Research (ZSW) in Ulm in the division for Accumulators Materials Research directed by Dr. M. Wohlfahrt-Mehrens
- 2017      **Research assistant:** Fraunhofer IISB Erlangen in the group battery systems
- 2015 – 2017      **Working student:** Robert Bosch GmbH in Bamberg in the development and process engineering of Li-ion battery cells
- 2015      **International internship:** Robert Bosch Battery Systems LLC in Orion, MI, USA in the systems engineering of the Fiat 500e Li-ion battery pack
- 2014 – 2015      **Working student:** Siemens AG in Erlangen in the development of IGBT-modules for electric drives
- 2012 – 2014      **Working student:** Bosch Rexroth AG in Nürnberg in the manufacturing of gearboxes for wind power stations
- 2013      **Internship:** Robert Bosch GmbH in the cooperate research of laser ablation techniques for CIGS solar cells